# An Exploration of the Cellular Origins and Metabolic Vulnerabilities of Glioblastoma

by

Yu-Jung Chen

A Dissertation

Presented to the Faculty of the Louis V. Gerstner, Jr.

Graduate School of Biomedical Sciences,

Memorial Sloan Kettering Cancer Center

in Partial Fulfillment of the Requirements for the Degree of

Doctor of Philosophy

New York, NY

September 2023

_____ _____

Luis F Parada, PhD Date
Dissertation Mentor

**Dedication**

To my parents and sister.
To my fiancée, I-Li.
And to those patients whose lives crossed path with mine.

## Abstract

Glioblastoma is a malignant disease with dire prognosis and in urgent need of improved therapeutics. We studied a previously uncharacterized stem progenitor population in the basilar pons of adult mice and investigated its tumorigenic potential. This quiescent population was able to give rise to a tumor when the three most common tumor suppressor genes (*Nf1*, *Trp53* and *Pten*) are deleted. The tumors generated resembles those derived from the oligodendrocytic progenitor cells (OPC).

In another independent study, we identified a small compound, Gliocidin, that kills glioblastoma cells while sparing replicative mouse embryonic fibroblasts. Gliocidin activity reveals a *de novo* purine synthesis pathway metabolic vulnerability in glioblastoma caused by indirect inhibition of inosine monophosphate dehydrogenase 2 (IMPDH2). Gliocidin mediated IMPDH2 blockade reduces intracellular guanine nucleotide levels causing nucleotide imbalance, replication stress, and tumor cell death. Gliocidin is a prodrug anabolized into its tumoricidal metabolite by the enzyme nicotinamide nucleotide adenylyltransferase (NMNAT1) of the $NAD^+$ salvage pathway. *In vivo,* Gliocidin penetrates the blood brain barrier and extends orthotopic murine GBM mouse survival. The DNA alkylating agent, Temozolomide (TMZ), induces Nmnat1 expression causing a synergistic tumor killing effect and additional survival benefit in patient-derived xenograft (PDX) orthotopic mouse models. Additionally, we uncovered GID E3 ligase complex degradation of NMNAT1, and its negative regulator, YPEL5, thus identifying a novel actionable target to enhance Gliocidin

activity. This study brings Gliocidin to light as a prodrug that can improve the survival of GBM patients.

## Biographical Sketch

Yu-Jung was born in Taipei, Taiwan to Tso-Ming Chen and Li-Hsueh Yeh in 1986. He moved to Bangkok Thailand at the age of 6 as his family relocated for his father's career. From age 6 to 18, he studied at Ruamrudee International School from primary school all the way until high school.

In 2005, Yu-Jung returned to Taiwan and entered the medical school of National Yang-Ming University (now called National Yang-Ming Chiao-Tung University). During summers of 2006-2009, he worked as an undergraduate research student in the lab of Dr. Mei-Yu Chen, working on mTORC2 signaling projects using the budding yeast as model. He completed his clinical clerkship and subintership in 2009-2011 at multiple teaching hospitals across Taiwan and at the UCSD medical center. He did his internship from 2011-2012 at Taipei Veterans General Hospital.

After medical school, Yu-Jung decided to continue to train himself in the field of molecular biology and onco-cellular signaling research, he entered the masters program at the Institute of Biochemistry and Molecular Biology at National Yang-Ming University. He worked on his thesis project in Dr. Mei-Yu Chen's lab for two years, focusing on the topic: The Regulation of mTORC2 activity and Rictor Expresion in Head and Neck cancer cells. He graduated and earned his master of science (MS) degree in 2014. It was also at that time when he helped diagnosed a close friend of his with a malignant tumor. It was that event that led him to understand the necessity to advance medicine is to fulfill unmet clinical needs and decided to pursue a cancer research career

After earning his MS, Yu-Jung then went on to fulfill his one-year of compulsory military service obligation. After a month of basic training at Cheng Kung Hill, he went to serve for 11 months in the alternative military service program at the Taiwan Water Resource Agency. Upon fulfilling a year service obligation, he went on to practice as a post-graduate year resident doctor at the Ditmanson Medical Foundation Chia-Yi Christian Hospital for 5 months.

In 2016, Yu-Jung was matriculated into the Louis V. Gerstner Jr. Graduate School of Biomedical Science and moved to New York to begin his PhD studies. In 2017, he joined the Parada lab for his doctoral research. Since then, he has been studying glioblastoma to try to understand its vulnerabilities for future therapeutic purposes.

## Acknowledgement

My graduate school years were a mix of ecstatic and down moments, which I believe are integral and inevitable aspects of a PhD journey. The presence of my lab colleagues throughout those years made this journey all the more enjoyable.

I would like to express my gratitude to my colleague Swathi Iyer, with whom I have collaborated over the past seven years. We have grown together and achieved numerous milestones. I want to thank Yufeng Shi for providing me with the opportunity to work on the finishing touches of his project, which opened the door to glioblastoma research for me. Special thanks go to Zilai Wang and Daochun Sun, both of whom have imparted essential skills, mentality, and concepts during my early years of graduate school. I extend my appreciation to Peter Xie, who has set an exemplary scientific standard for our lab. I am also grateful to Jing Li, who has consistently assisted me with intracranial experiments, dedicating countless hours to my research. I would like to acknowledge Alicia Pedraza, whose silent contributions are indispensable for the smooth functioning of the lab. Furthermore, I want to thank Sarnai Ganbold for dedicating numerous hours to my projects, significantly advancing our science. My gratitude goes to Michelle Lien, who has always been open to help, even during her busiest moments. I am grateful to Tao Wang for giving me the opportunity to learn and grow as a mentor. I would also like to express my gratitude to Sheila Alcantara, Charlene Iltis, Stefan Sweha, Kacper Walentynowicz, Chenura Jayewickreme, Mollie Chipman, and Dan Laks for being amazing colleagues.

Lastly, I want to acknowledge our exceptional administrative staff: Keisha Diaz, Ashley Chandradat, Aimee Cowan, and Tünde Frankl. I cannot thank them enough for their extraordinary support, which has significantly improved my lab life in so many aspects.

I would like to express my gratitude to my committee members, Drs. Alex Joyner and Robert Benezra, for their unwavering support and guidance throughout my years of PhD training. I am also thankful to Dr. Lydia Finley for chairing and to Dr. Robert Wechsler-Reya for serving as the external advisor of my thesis committee. I am grateful for their suggestions and advice during my thesis defense.

Most importantly, I want to convey my utmost gratitude to my PhD advisor, Luis Parada. His mentorship has not only provided me with invaluable guidance but has also created a vibrant and nurturing research environment. The unwavering support I have received from Luis has been instrumental in propelling my research career forward. I am extremely grateful to him.

I would like to thank my friends and community, both here in New York and back in Taiwan. Their incessant words of support and companionship have provided me with constant energy to stay on the path of research.

I would like to thank I-Li Tan for her unwavering support throughout these years. I would not have been able to pull through the toughest moments without you by my side.

Finally, I would like to express my gratitude to my family, who have supported me unconditionally throughout my life. None of what I have achieved

today would have been possible without the sacrifices and unspoken love from my parents.

## Table of Contents

## List of figures

## List of Abbreviations

**COP**: Committed Oligodendrocyte Precursor cell

**CGD**: Cre-GFP-Diphtheria Toxin Receptor

**CRISPR**: Clustered Regularly Interspaced Short Palindromic Repeats

**GBM**: Glioblastoma

**GID**: Glucose-Induced Degradation

**GMPS**: Guanine Monophosphate Synthase

**GSEA**: Gene Set Enrichment Analysis

**IDH**: Isocitrate dehydrogenase

**IMPDH**: Inosine Monophosphate Dehydrogenase

**MAEA**: Macrophage Erythroblast Attacher

**MFA**: Mycophenolate Mofetil

**MPA**: Mycophenolic Acid

**mTOR**: Mammalian Target of Rapamycin

**mTORC1**: Mammalian Target of Rapamycin Complex 1

**NAD**: Nicotinamide Adenine Dinucleotide

**NG2**: Neural/glial antigen 2

**NMN**: Nicotinamide Mononucleotide

**NMNAT1**: Nicotinamide Nucleotide Adenylyltransferase 1

**NRK1**: Nicotinamide Riboside Kinase 1

**NSC**: Neural Stem Cell

**NST**: Nestin

**OPC:** Oligodendrocyte Progenitor Cell

**PDX**: Patient-Derived Xenograft

**RMND5A**: Required For Meiotic Nuclear Division 5 Homolog A

**SVZ**: Subventricular Zone

**UBE2H**: Ubiquitin Conjugating Enzyme E2 H

**WDR26:** WD Repeat Domain 26

**YPEL5**: Yippee Like 5

## Chapter 1 Introduction

Glioblastoma (GBM) is the most common adult primary brain malignancy and is amongst the most lethal human cancers. The incidence of GBM increases after age 40 and peaks in adults age 75-84 years of age. It is highly aggressive with a median overall survival of about 15 months after radiation and chemotherapy. Despite more than a decade of effort in GBM research with new scientific insights gained, the prognosis of GBM patients has mostly remain unchanged. This discrepancy between the wealth of biological knowledge amassed and the stagnated drug development process and unsuccessful clinical trials warrant a more meaningful/insightful way of doing GBM research. This introduction aims to give an comprehensive overview of the necessary information we currently need to know about GBM. More in-depths knowledge of each subtopic could be found elsewhere.

### WHO Classification of GBM

According to the fifth edition of the WHO classification (2021), glioblastomas are classified as adult-type isocitrate dehydrogenase (IDH) wildtype diffuse gliomas. Under this most recent version, adult-type diffuse glioma now consists of three distinct diseases: 1) astrocytoma, IDH mutant, 2) oligodendroglioma, IDH mutant, and 1p/19q co-deleted and 3) Glioblastoma, IDH wildtype or IDH mutation status not otherwise specified (NOS) (Louis et al., 2021). This new classification first separates glioma based on the status of IDH mutation, as IDH mutant gliomas has an overall better prognosis than IDH wildtype gliomas. Then among IDH

mutant gliomas, the presence of 1p/19q codeletion distinguishes between astrocytoma and oligodendrogliomas. All grades of IDH mutant astrocytoma (grade 2, 3 and 4) are grouped together under the same disease entity, while glioblastoma only consists of grade IV IDH wildtype tumors. Oligodendroglioma are typically grade 2 and 3 tumors.

For historical comparison purpose, in the previous versions of WHO classification, glioblastoma was classified based on its clinical course and mutational status as either primary and secondary GBM (Louis et al., 2016). Primary GBM (about 90%, IDH wildtype) corresponds to clinically defined *de novo* GBM that occurs more commonly in adults over 55 years of age, while secondary GBM (about 10%, IDH mutant), corresponds to a prior history of low grade glioma that commonly occurs in younger adults. It was already then known that GBM with an IDH mutation had a better prognosis, but was only in 2021 that GBM was defined as a singular entity defined as IDH wildtype to indicate its worse prognosis and distinct underlying pathobiology.

**Molecular Classification of GBM**

In the era of next generation sequencing, tumors have been massively sequenced and tumor repositories were established that contains a wealth of sequencing information for a diverse number of tumor types. The Cancer Genome Atlas (TCGA) is one such network with GBM being one of the earliest tumor type to be profiled (Cancer Genome Atlas Research, 2008). It began by characterizing DNA copy number changes and gene expressions of 206 glioblastoma tumors.

Thus, it is one of the most molecularly profiled of all human cancers. The abundant genomic profiling of GBM has led to the identification of its most frequent recurrent somatic mutations such as *PTEN* (31.%), *TP53* (29.0%), *EGFR* (26.6%), *NF1* (11.0%), *RB1* (8.6%), *PIK3CR1* (11.4%) (updated based on the most recent TCGA GBM Firehose Legacy on cBioportal) and copy number changes *CDKN2A* (57.4%), *EGFR* (43.8%), *CDK4* (14.8%), *PDGFRA* (12.8%) and *PTEN* (9.7%).

GBM was initially classified in 2010 as four molecularly distinct groups (namely proneural, neural, classical, and mesenchmymal) based on the gene expressions, recurrent somatic mutations and methylation profiles (Brennan et al., 2013; Verhaak et al., 2010). In 2017, it was reclassified into only proneural (PN), classical (CL) and mesenchymal (MES), omitting the neural subtype as it was discovered to be contamination of normal neural lineage cells (Q. Wang et al., 2017)

Based on this new classification, retrospective analysis of overall survival between the three groups are 11.5, 14.7 and 17.0 months in MES, CL and PN cases, respectively. MES has the poorest outcome of all and is correlated with higher immune cell infiltration. Among MES tumors, *NF1* is a frequently mutated or deleted tumor suppressor gene and is highly correlated with tumor associated macrophages/microglia infiltration. However, the exact mechanism to *NF1* inactivation leading to macrophage infiltration is still currently unknown. (Q. Wang et al., 2017). It is important to mention here that the TCGA data-based molecular stratification of GBM was not considered to be stratification factors in the WHO classification of diffuse gliomas.

Recently a longitudinal study of GBM patients was conducted by the Glioma Longitudinal Analysis Consortium (GLASS), to study the molecular evolution of glioma and identification of recurrent drivers (Varn et al., 2022). This study showed that approximately fifty percent of recurrent tumors underwent a change in tumor subtype, which are categorized as neuronal, mesenchymal, and proliferative. The neuronal subtype is characterized by a discernible increase in the population of proliferating stem-like cells, concomitant with an elevation in the expression of genes pertinent to neuronal signaling, which may potentially stem from interactions between tumor cells and neurons. In contrast, the mesenchymal subtype encompasses tumors that either initially harbored or acquired an NF1 mutation during the recurrence phase. This transition towards a mesenchymal phenotype is associated with an escalation in granulocytes and myeloid cells within the tumor microenvironment. Using receptor-ligand analysis of these datasets suggest that the expression of oncostain M (OSM) and oncostatin M receptor (OSMR) by myeloid cells and tumor cells, respectively, are strongly enriched in the mesenchymal subtype. This is in line with studies showing that OSM-induced the *in vitro* transition of glioma cells into mesenchymal state through STAT3 signaling (Hara et al., 2021). The proliferative subtype predominantly comprises an augmented population of proliferating stem-like tumor cells. This subtype is characterized by temozolomide-driven hypermutation and acquired deletions of *CDKN2A* and *CCND2* genes. Both the mesenchymal and proliferative subtypes upon recurrence are correlated with a worse survival prognosis.

However, the clinical/biological relevance and functional basis of the algorithm-generated groups are not well established.

**Cell of Origin of GBM**

Currently, the consensus is that glioblastoma arises from the neural stem cells in the subventricualar zone of the lateral ventricles. The study of the cell of origin of glioblastoma has largely benefited from studies of the wildtype neural stem cell field. In the adult mammalian brain, neurogenic regions harboring neural stem cells (NSCs) are located in the subventricular zone (SVZ) of the lateral ventricle (Doetsch et al., 1999; Johansson et al., 1999) and the subgranular zone (SGZ) of the hippocampal dentate gyrus (Ahn & Joyner, 2005; Casper et al., 2007; Palmer et al., 1997; Song et al., 2002). In the SVZ, neural stem cells are a self-renewing population that gives rise to new neurons that migrate through the rostral migratory stream into the olfactory bulb and oligodendroctyes in the white matter. *Gli*, *Gfap*, *Glast*, *Sox2* and *Nestin* are markers that have been used to identify neural stem cells and have been shown by lineage tracing experiments to give rise to neurons and glia.

Active NSCs give rise to transit amplifying cells (TACs), which can be marked by the transcription factors ASLC1 and DLX2 (Doetsch et al., 2002; Kim et al., 2007). On the neuronal path, TACs divide symmetrically approximately three times before differentiating into neuroblasts, which are marked by doublecortin (DCX) (Ponti et al., 2013). Chains of neuroblasts then migrate to the olfactory bulb (OB) forming a path called the rostral migratory stream (RMS). Along the RMS,

neuroblasts divide one to two more times before reaching the OB to differentiate into interneurons, which are marked by NeuN (Ponti et al., 2013). NSCs and TACs give rise to relatively fewer glial lineages than neurons. In the normal uninjured state, NSC and TACs that express OLIG2 can migrate into the corpus callosum to differentiate into oligodendrocytic precursor cells (OPC; NG2 and PDGFRα positive) (Menn et al., 2006). OPCs then divide to proliferate into mature oligodendrocytes (OLIG2 and APC/CC1 positive) in the corpus callosum. After demyelinating injury, oligodendrogliogenesis rapidly increases, suggesting that NSCs are subjected to cues that change their developmental course during injury (Nait-Oumesmar et al., 1999; Picard-Riera et al., 2002). Similarly, brain injury has also been shown to trigger NSCs from the SVZ to form astrocytes that migrate to the injury site (Benner et al., 2013).

Experimental evidence supporting the notion that glioblastoma arises from a neural stem progenitor population in the adult brain came largely from past three decades of studies using tumor mouse models. These models have been created by introducing mutations through specific promoter transgenes that target stem progenitor populations. A variety of tumor suppressor genes (TSG) and oncogenes have been exploited in mice to generate brain tumors that phenocopy human glioma. *Tp53* mutations were amongst the most commonly used mutation as it is often mutated in human GBM. The first spontaneous glioma mouse model generated was based on cis-germline heterozygous loss of *Tp53* and *Nf1* that showed a wide range of astrocytoma grades (Reilly et al., 2000). As evidence showed that GBM contain a population of cells with stem cell characteristics (Singh

et al., 2003), later models with *hGFAP-cre* or *hGFAP- creER* driven conditional knockout of *Tp53* along with other different tumor suppressor genes (*Pten*, *Nf1*, or *Rb*) were also shown to develop high grade glioma with high penetrance (Chow et al., 2011; Zheng et al., 2008; Zhu et al., 2005), while introducing *Pten* heterozygosity into the *Tp53*/*Nf1* model resulted in accelerated morbidity (Kwon et al., 2008). As human GFAP transgene is not exclusively expressed in NSC but also in mature astrocytes, the *Nestin-creER* line was used to target more specifically in neural stem/progenitor cells (Chen et al., 2009; Lagace et al., 2007), and was shown to induce GBM formation with complete penetrance upon conditional inactivation of *Tp53*, *Nf1*, and *Pten* at four weeks of age (Alcantara Llaguno et al., 2009).

The concept of the SVZ neural stem/progenitor cells, and not the differentiated astrocytes, being the cell of origin of GBM was further demonstrated when tumors only arise in the SVZ and not in the cortex and the striatum when viral cre adenovirus to induce TSG recombination was injected into these corresponding regions (Alcantara Llaguno et al., 2009). Another independent study also showed that only transplanted NSCs, and not transplanted astrocytes, with *P53/Pten/Rb* mutations gave rise to tumors (Jacques et al., 2010). Furthermore, our laboratory has previously substantiated the premise that cells of the neuronal lineage, either progenitor and differentiated, cannot give rise to glioma (Alcantara Llaguno et al., 2019). Through the utilization of different mature neuron (Camk2a-creER$^{T2}$), immature neurons (NeuroD1-creER$^{T2}$) and neuronal progenitor (Dlx1-creER$^{T2}$) mouse models to knockout *Nf1*, *Trp53*, and *Pten*

knockout in the corresponding neuronal cell types and showed that neurons or its progenitors are incapable of initiating glioma formation.

Aside from NSC as the candidate cell of origin for GBM, we have also previously demonstrated that inducing *Nf1*, *Trp53* and *Pten* deletions in the *Ascl1-creER* line targeting neural progenitors gave rise to two different types of high grade gliomas that differed by location, histology, lineage markers, and gene expression profile, in which we named them as type I and II tumors. The type I tumors are more infiltrative with high GFAP and NESTIN expression and are primarily localized to the dorsal brain, while type II tumors have better- defined borders that expresses oligodendrocytic markers and are localized to the ventral brain. It was further demonstrated that type I tumor arises from neural progenitor and type II tumor from OPCs, as *Nestin-creER* generates tumor resembling type I tumor and *NG2-creER* generated tumors resembling type II tumor, both exhibiting lineage-specific signatures. Results from other studies also showed that OPCs are another cell of origin of GBM by using similar methods (Galvao et al., 2014; Liu et al., 2011). Though OPCs have been shown to give rise to oligodendroglioma, however, the driver mutations do not associate with *Trp53* or *Nf1 (Persson et al., 2010)*.

Overall, current evidence is consistent with the following: 1) GBM arises from the more immature stem/progenitor population and 2) identical mutations introduced in different cell types can give rise to different molecular subtypes of tumors. Therefore, it is possible that different cellS of origin-mutation combination can lead to different subtypes of GBM.

**Cancer Stem Cell Theory vs Plasticity Model**

GBM is a highly intratumoral heterogeneous tumor. Traditionally, the tumor heterogeneity of GBM is explained through the developmental biology lens, or the cancer stem cell theory, where a cellular hierarchy exist with a stem cell situated at the apex and differentiated cells at the base (Clevers, 2011; Reya et al., 2001). At the apex, cancer stem cells are a quiescent population and like stem cells, either self-renew or asymmetrically divide to give rise to downstream progenitor-like tumor cells. A diverse array of progenitor-like cells then undergo further cell divisions that give rise to differentiated-like tumor cells. Through successive rounds of this uni-directional top to bottom division and expansion, diversity arises within the tumor population. Treatment such as chemotherapy or radiation targets rapidly proliferating cells, but not the quiescent cancer stem cells. Recurrence of GBM is proposed to arise from the therapy-resistant cancer stem cells, where over time, re-activation of stem-like cells can give rise to an entire tumor entity (Chen et al., 2012). This has long been the explanation to heterogeneity in tumors where a developmental-stem cell like-hierarchy existed. Thus, the search for cancer stem cell markers to specifically target CSCs has long been an area of focused research. However, though many CSC markers have been proposed and experimentally demonstrated, current understanding is that the there is no one optimal fixed CSC marker that can be applied to all GBMs. Some possibilities include that multiple markers maybe needed to define CSCs or that there is even heterogeneity within

CSCs. More in-depth studies on GBM CSCs are required to address these essential questions.

An alternative perspective suggests that the rigid unidirectional CSC model falls short in explaining intratumoral heterogeneity, while the plasticity model emerges as a more plausible theory. Recent investigations utilizing single-cell sequencing techniques on GBM cells, in conjunction with bulk-RNA-seq derived subtype identifiers, have revealed that tumor cells from the same tissue exhibit gene signatures of various subtypes (Patel et al., 2014). Additionally, theoretical frameworks have been postulated, proposing that GBM cells exist in four distinct states, primarily influenced by their genomic copy number alterations and mutational profiles (Neftel et al., 2019). These states include OPC-like (associated with *PDGFRA* amplification), NPC-like (linked to *CDK4* amplification), AC-like (related to *EGFR* amplification), and MES-like (correlated with *NF1* mutation). The model proposed by the Neftel *et al*. contends that tumor cells possess plasticity, permitting them to transition between these cell states. This implies that CSCs may not be a fixed entity, but rather a flexible and adaptive cellular state that changes in response to external cues. It is important to note, however, that this model relies solely on the analysis of expression datasets. Experimental validations have not yet yielded conclusive results and necessitate further comprehensive verification.

Our lab has previously demonstrated that GBM arises from different types of stem and progenitor lineages with identical tumor suppressor mutations have similar histology (Alcantara Llaguno et al., 2015). However, histologic and gene expression analysis reveal differential features between GBM from different cells

of origin. These observations in the mouse model suggest that the cell of origin can be an important determinant of GBM subtypes. Hence, identification of other cells of origin of GBM may uncover previously undetermined molecular subtypes. Integrating this information may provide a better classification of GBM that reflects biological relevance.

**Extrachromosomal DNA**

Another intriguing mechanism that has recently re-gained attention, shedding light on intratumoral heterogeneity, involves the studies of extrachromosomal DNA (ecDNA) in tumors. EcDNA, distinguished by its circular structure, assumes a pivotal role in 40-60% of GBM, effectively harboring the amplified proto-oncogenes *EGFR*, *PDGFRA*, *CDK4*, *MDM2*, and *MYC* and their enhancers (deCarvalho et al., 2018). The distinctive extrachromosomal positioning and circular structure provide easy accessibility to transcription factors, thereby facilitating transcription. Moreover, free from chromosomal and positional constraints, ecDNA is inherited unevenly by daughter cells, leading to a rapid increase of intratumoral heterogeneity.

**Current treatment modality of glioblastoma and obstacles encountered**

Treatment of glioblastoma consists of gross surgical resection of all contrast-enhancing tumor, followed by 6 cycles of concurrent radiation and administration of oral akylating agent temozolomide. This led to an improved survival outcome as compared to receiving only radiation alone (14.6 months vs

12.1 months; hazard ratio [HR], 0.63 [95% CI, 0.52-0.75]; P < .001) (Stupp et al., 2005). Patients with *MGMT* methylation in tumor tissue responds better to temozolomide and has a better overall survival (21.7 months 95% CI, 17.4-30.4) compared with radiation alone (15.3months (95% CI, 13.0-20.9) with radiation alone (P = .01) (Esteller et al., 2000).

GBM recurrence is invetiable (approximately 7 months after treatment), and are thereafter treated with additional surgery, chemotherapy (including temzolomide and nitroureas) and radiation. Although Bevacizumab (anti-VEGF Ab) is also approved for recurrent GBM, it is only used as a symptomatic treatment for cerebral edema, with no benefits on patient overall survival (Chinot et al., 2014).

A recent noninvasive treatment modality of GBM is Tumor Treating Fields (TTFields) or commercially named as Optune® developed by Novocure. TTField applies low intensity, intermediate-frequency alternating electric fields over the brain tumor region. It is designed as a wearable product over the head of the patient. The FDA of the United States has approved Optune® for the treatment of recurrent (in 2011) and newly diagnosed GBM (in 2015). Patients with TTFields plus temozolomide (20.5 months, 95% CI, 16.7-25.0 months, n=196) have a better overall survival than patients on temozolomide (15.6 months, 95% CI, 13.3-19.1 months, n=84) (HR, 0.64 [99.4% CI, 0.42-0.98]; P = .004) (Stupp et al., 2015).

The mechanism of action of TTFields on tumors is thought to involve low intensity (1-2V/cm) and medium frequency (100-400 kHz) waves to affect the cell cycle to decrease proliferation. Detail proposed mechanisms include affecting the polarization of microtubules required for mitosis, electromagnetically affecting the

distribution of macromolecules during mitosis causing aneuploidy, which then induces a cascade of autophagy and cell death (Guo et al., 2022).

**Targeted therapies and Immunotherapy in GBM**

Due to previously assumed upregulated pathways in GBM, as analyzed by TCGA and various studies, attempts have been made to treat GBM through targeted therapies aimed at oncogenic signaling pathways. Unfortunately, these endeavors were ineffective (Touat et al., 2017). Unsurprisingly, in the era of immunotherapy, checkpoint inhibitors such as anti-PD1 have also been tested in combination with the standard treatment of care for GBM patients. However, in newly diagnosed GBM patients irrespective of MGMT status (Lim et al., 2022; Omuro et al., 2023), phase 3 clinical trials revealed that the combination of nivolumab and temozolomide, along with radiation, did not lead to improved overall survival. The same lack of survival benefits was also observed in recurrent GBM, as evidenced by trials comparing nivolumab and bevacizumab (Reardon et al., 2020). While an analysis of post-treatment tumors does suggest alterations in the immune microenvironment due to checkpoint inhibitors, there is a lack of convincing evidence regarding their efficacy against tumors. This discrepancy might be attributed to the immunosuppressive environment commonly found in GBM, where the presence of adaptive immune cells is limited, and their function appears to be compromised due to exhaustion.

## Chapter 2 The study of CGD transgene labeled cells as potential stem progenitor cells and cells of origin of GBM

This chapter breaks into three different sections. The first investigates the stem cell potential of the Nestin transgene labeled cells in the basilar pons of early postnatal to juvenile (P28-30) mice. The second part investigates the type of tumor generated from these CGD transgene labeled cells. The last part is a recent investigation on an enriched oligodendrocytic prognenitor population called committed oligodendrocytic progenitors (COP), specifically focusing on its identification and isolation.

### Introduction

### Nestin transgene labeled cells are present in the basilar pons of 4-week old mice

Various *Nestin* promoter transgenic mouse lines have long been used extensively to study neural stem cells. *Nestin* is type VI neurofilament and a cytoskeletal protein. It is known to be expressed widely in tissues and stem progenitor cells such as pancreatic islets, skeletal muscle satellite cells, developing myotomes, testis, hair follicles and even in hematopoietic stem cells. In the context of GBM, it is a biomarker for invasiveness (Ishiwata et al., 2011).

In the CNS, Nestin is expressed as early as E7.5 in neuroepithelium (Lendahl et al., 1990) and gradually subsides during differentiation (Mignone et al., 2004). In studies where Nestin knockout mice were generated, although there was a substantial decrease in neural stem cells and mild reduction in peripheral motor

function, overall the mutants showed a normal gross development of the central nervous system (Mohseni et al., 2011).

Although Nestin is expressed in a wide variety of tissue, it is really the intron elements of Nestin that regulates its tissue specific expression. In earlier studies, it has been demonstrated that the first and second intron directed reporter gene expression to mainly muscle and neural precursors (Zimmerman et al., 1994). Though different independent Nestin transgeneic mouse lines exist in the neural stem cell research field, they all utilized the rat *Nestin* promoter in conjunction with its second intron that limits transgene expression to the central nervous system.

Our lab has previously generated a *Nestin* promoter transgenic line and have been using it to study GBM that arises from the subventricular zone (Chen et al., 2009). We have previously demonstrated that 4-weeks old *Nestin-CreER; Rosa26-LacZ*$^{lox\text{-}stop\text{-}lox}$ mice has transgene expression in the basilar pons, shown by β-galactosidase staining in mice induced with tamoxifen at 4 weeks of age (Figure 2.1A). Using another independently generated Nestin transgenic mouse model (Xie et al., 2020), we also observed expression of the Nestin transgene in basilar pons at the adult age (Figure 2.1B). This newer version of Nestin transgene cassette, which we named as CGD, harbors: (1) an inducible ***C****re* recombinase; (2) a *H2B-eGFP* fusion gene to label NSCs with GFP expression; (3) human **D**iphtheria Toxin receptor, for temporally regulated ablation of the neural progenitors by administering diphtheria toxin (Figure 2.1C). These genetic elements are under the control of a rat *Nestin* promoter and second intron (as are other Nesting transgenes) that drives expression specifically in NSC and not other

cell types[44]. It is important to note that the CGD transgene expression (Rat *Nestin* promoter) does not necessarily reflect endogenous murine *Nestin* expression, and thus additional validation is needed. The CGD line expresses GFP in the adult basilar pons even until 3 months of age (Figure 2.1C), though there is a tendency to have a decrease in GFP intensity over time.

Having observed GFP expression in the basilar pons of adult CGD mice, and given the historical correlation of $Nestin^+$ neural cells with stemness, we proceeded with asking two major questions:

1. Are the $GFP^+$ cells in the pons stem progenitor cells?
2. Can these $GFP^+$ cells give rise to glioblastoma?

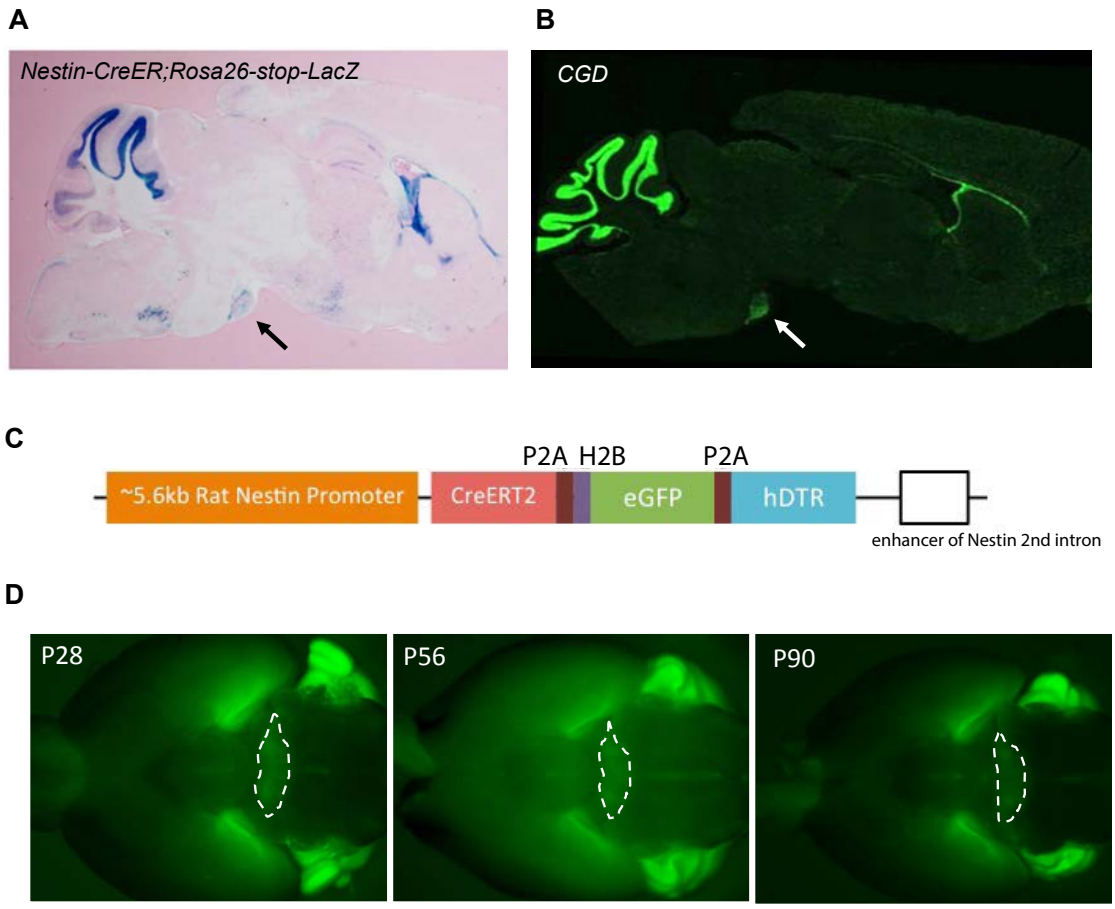


**Figure 2.1. CGD transgene.** (A) A sagittal section of X-gal staining of 8- weeks old *Nestin*-creER; R26lacZ mouse brain induced with tamoxifen at 4-weeks of age. Arrowhead pointing at basilar pons (arrow). (B) A sagittal section of 6-wk old CGD mouse brain with GFP expression at basilar pons (arrow). (C) Diagram of the CGD transgene construct, consisting of a rat *Nestin* promoter sequence, cDNA encoding CreER fusion protein, H2B-eGFP, human diphtheria toxin receptor and an enhancer of the *Nestin* second intron interconnected with P2A peptide sequence for multiple gene expression. (D) Immunofluorescent images showing eGFP expression from the ventral side of the whole brain at different ages of CGD mice.

## Results

### Pontine GFP$^+$ cells are not differentiated astrocytes or oligodendrocytes

First, we observed through tissue immunofluorescence staining (Figure 2.2A) that there exists GFP expressing cells with two different expression intensity, which hereafter we denote them as GFP$^{high}$ and GFP$^{low}$ cells (Figure 2.2B). We investigated whether CGD transgene labeled cells are stem progenitor cells in the basilar pons by performing immunohistochemistry using defined known stem cell, differentiated neuronal and glial markers. We ask whether these CGD labeled cells belongs to the oligodendrocytic or astrocytic lineage. In the P28 (young adult) *in vivo* basilar pons setting, all GFP$^+$ cells do not express OLIG2 (pan-oligodendrocytic lineage marker) or S100β (differentiated astrocytic lineage marker), suggesting these cells are not oligodendrocytic cells or differentiated astrocytes (Figure 2.2C-E).

### GFP$^{high}$ cells are mature neurons

Interestingly, we observed that GFP$^{high}$ cells co-stained strongly with the neuronal marker NeuN (Figure 2.2F). This is unexpected but we think can be explained by several reasons. Nestin+ cells are neural stem cells that give rise to neurons in the developing brain. Some NSCs may undergo rapid cell divisions (divide 1-2 times) to become terminally differentiated neurons. Also, it is highly plausible that the GFP expressed from the CGD transgene has a prolonged half-life, which is most likely attributed to the design of enhanced GFP expression by fusing with nuclear histone H2B. In non-dividing cells, it is known that H2B has a

long half life (median of 159 days). Thus, in non-dividing differentiated neurons, where endogenous Nestin expression have already subsided, due to the artifact of the prolong GFP-H2B fusion protein, GFP expression may exist for a prolonged period.

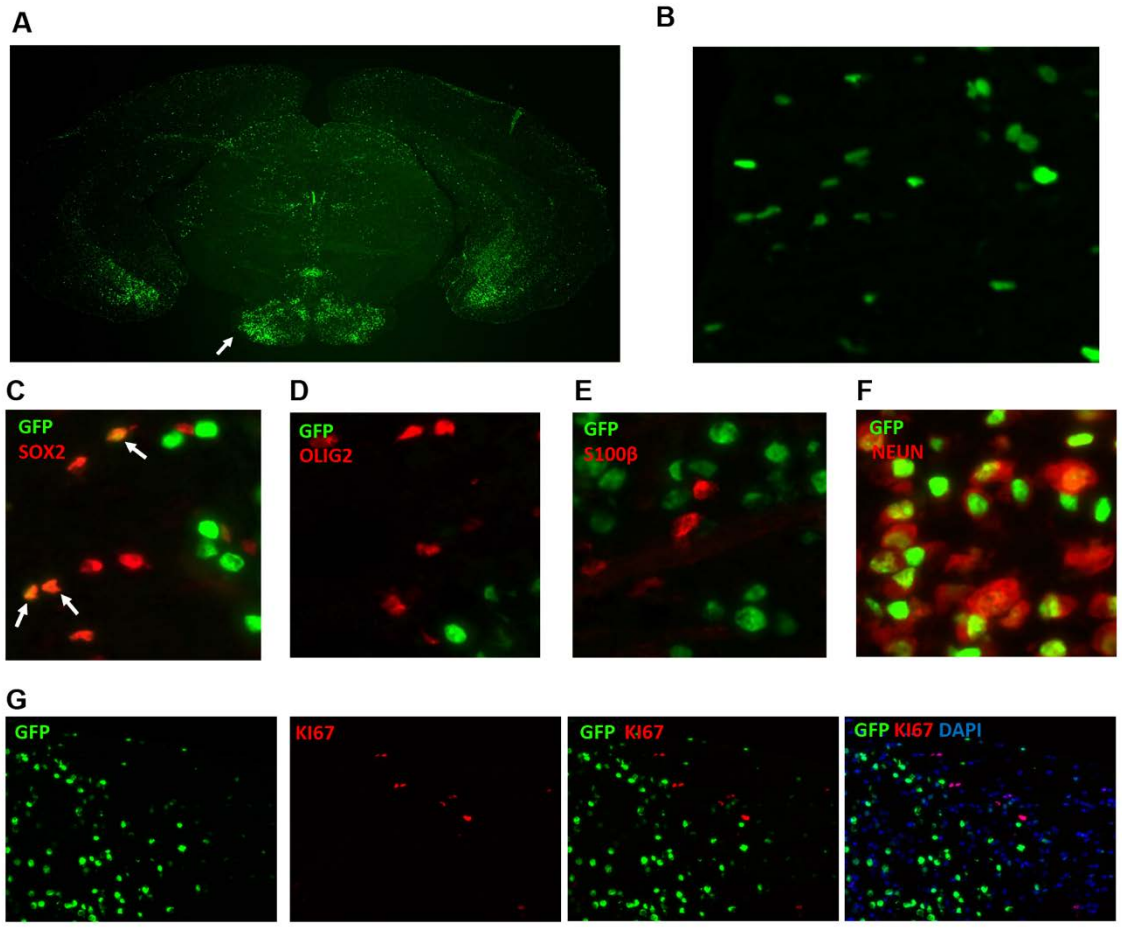


**Figure 2.2. GFP positive cells in P28 CGD basilar pons are non-proliferative, non-astrocytic and non-oligodendrocytic.** (A) GFP imaging of a coronal section of a P28 CGD mouse brain. Arrow points to basilar pons. (B) Immunofluorescence imaging of P28 basilar pontine regions showing GFP+ cells with various expression intensity. (C-F) Co-immunostaining of GFP with stem/astrocytic marker SOX and glial markers OLIG2, S100β and NEUN. (G) Co-immunostaining of GFP with KI67 in P28 CGD basilar pons.

**GFP$^{low}$SOX2$^{+}$ cells are a quiescent population**

Interestingly, all P28 GFP$^{low}$ cells expressed SOX2, a stem/progenitor marker, and were absent for KI67 (Figure 2.2G). As stem cells often reside in the quiescent stage, the absence of KI67 expression prompted us to ask whether GFP$^{low}$SOX2$^{+}$ are slow-cycling stem cells.

To study whether GFP$^{low}$SOX2$^{+}$ cells are indeed slow cycling, we performed a pulse chase experiment with 5-ethynyl-2'-deoxyuridine (EdU), in which mice were fed with water containing EdU for three weeks (pulse) (Figure 2.3A). If GFP$^{+}$ cells uptake EdU during the chase period, we will then perform a further chase experiment in which mice will be provided with regular water without EdU for another three weeks (chase). Slow-cycling cells are also known as label-retaining cells, as they take up EdU during the pulse period, but due to their infrequent divisions, retain the EdU label even after the chase period (as opposed to EdU being diluted and dissipate in rapidly dividing cells). However, after three weeks of EdU pulsing, we did not observe any EdU uptake in GFP$^{+}$ cells (Figure 2.3B). Cells that incorporated EdU were all negative for GFP, and upon further characterization, discovered to either express OLIG2 or SOX2 (Figure 2.3C). These observations strongly imply that GFP$^{low}$SOX2$^{+}$ cells at P28 exhibited a propensity to maintain their quiescent state. One possibility is that these cells are stem cells that require external perturbations (e.g., external cues, genetic mutations, injury, etc.) for activation. The other less possible explanation is that they are differentiated glial cells, which are less possible due to the absence of OLIG2 or S100β expression.

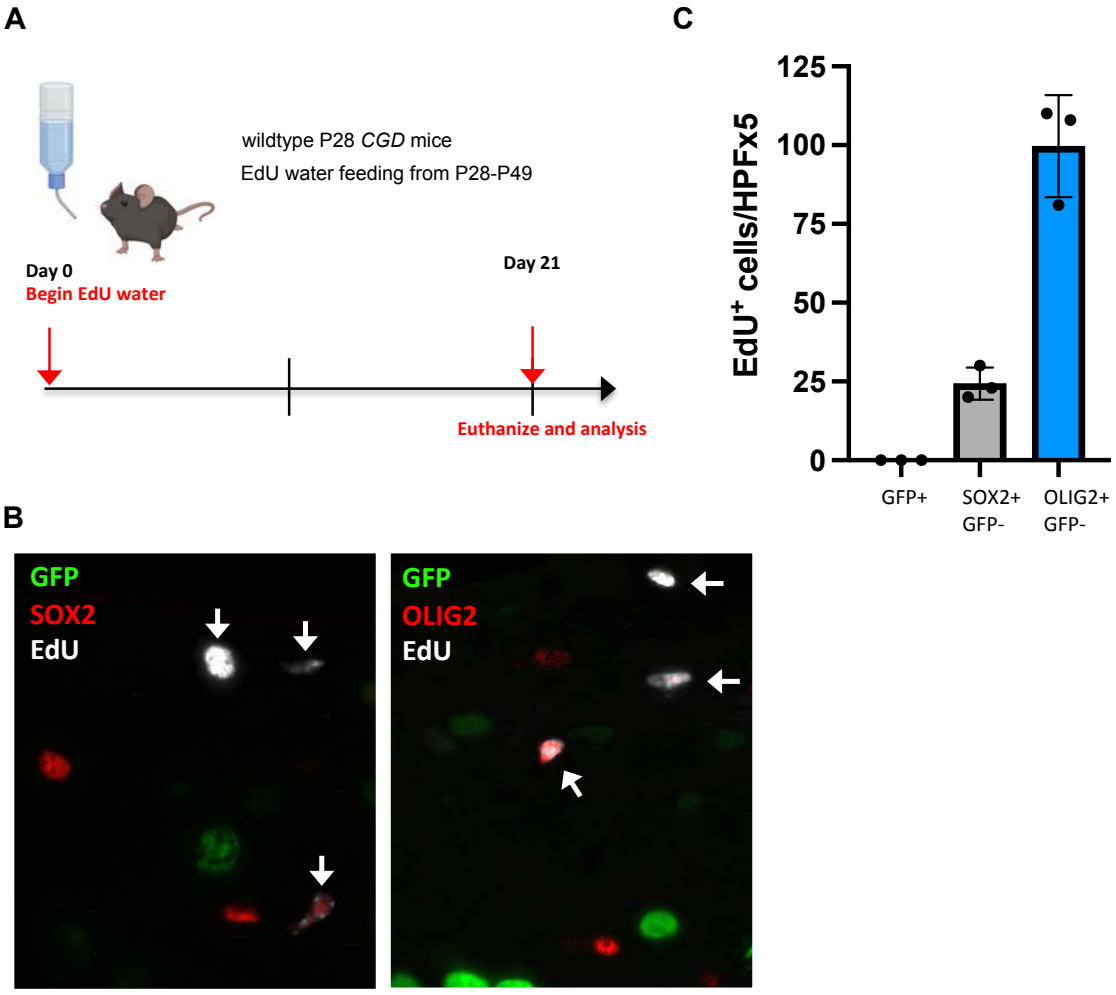


**Figure 2.3. GFP$^{low}$SOX2$^{+}$ cells are quiescent and do not uptake EdU.** (A) Schematic of experimental flow for EdU feeding (pulse) experiment. (B) Immunofluorescent staining showing uptake of EdU in GFP$^{-}$SOX2$^{+}$ and GFP$^{-}$OLIG2$^{+}$ cells and not in GFP$^{+}$ cells.(C) Quantification of cells with in EdU uptake in 5 high power field (HPF x5) view brain sections of EdU-pulse P49 CGD basilar pons (n=3). Data indicate mean ± SD (n=3 replicates).

## Pontine CGD positive cells require PDGF-AA for growth *in vitro*

Neural stem cells that are quiescent *in vivo* can be activated to proliferate and form neurospheres *in vitro (Codega et al., 2014; Xie et al., 2020)*. Thus, we also attempted to isolate and culture these quiescent GFP$^{+}$ cells dissociated from

P28 basilar pons to investigate whether they can be activated in the presence of exogenous growth factor. The $GFP^{high}NeuN^{+}$ cells do not cause concern, as mature neurons do not undergo proliferation in serum-free media. Moreover, during the process of tissue dissociation, neurons are prone to severing and results in cell death. Our initial approach involved employing a serum-free media (SFM) formulation typically used for culturing neural stem cells derived from the SVZ, comprising EGF and FGF (hereafter referred to as EF) (Morshead et al., 1994; Reynolds & Weiss, 1992). However, no cells dissociated from the basilar pons proliferates under the EF condition. This observation prompted us to speculate that specific growth factors may be required for activation.

Consequently, we systematically evaluated a selection of common growth factors frequently utilized in stem cell culture, testing various combinations. Neural stem cells (NSCs) from the SVZ, cultured using EF media, served as a positive control in these experiments. Among all the combinations, only FGF and PDGF-AA together promoted cell growth and sphere formation (Figure 2.4A and B). However, the number and size of spheres formed from $GFP^{+}$ cells were significantly lesser and smaller compared those originating from SVZ NSCs, respectively. These data led us to two possible conclusions: First, $CGD^{low}SOX2$ cells may exhibit lower stemness than SVZ NSCs. Second, there might be a lower absolute count of stem progenitor cells among the $GFP^{+}$ cell population in P28 basilar pons.

It is conceivable that the quantity of stem progenitor cells in a given niche decreases as the mouse ages. We speculate that this scenario may also apply to GFP$^{low}$SOX2 cells. To test this hypothesis, we conducted neurosphere assays on

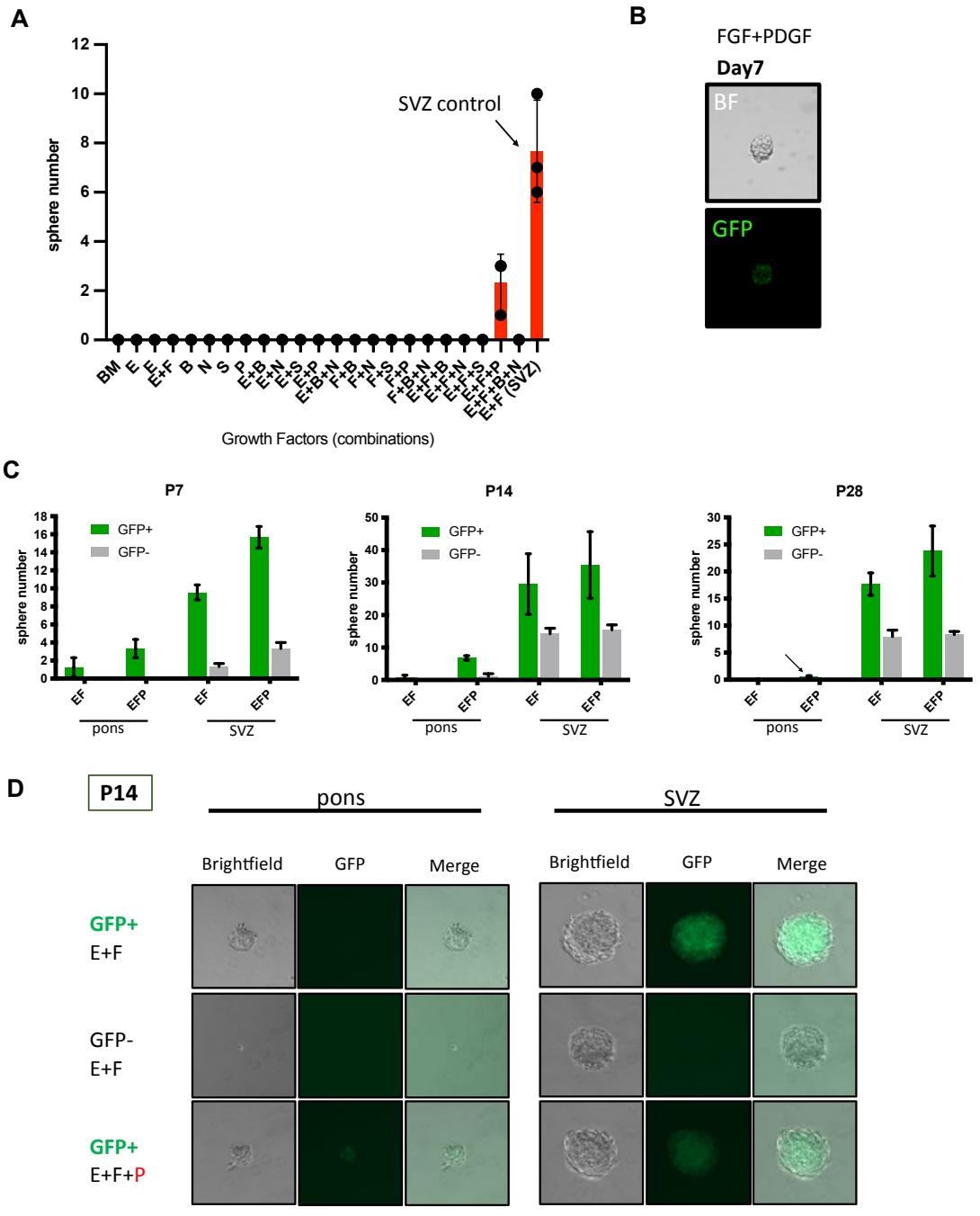

**Figure 2.4. FGF and PDGF-AA are required for P28 GFP$^+$ pontine cells to grow *in vitro*.** (A) Sphere number counts of P28 GFP$^+$ cells cultured in media condition with different growth factors (n=3). (B) Sphere formation of P28 GFP pontine cells, cultured in FGF+PDGF media for seven days. (C) Sphere counts of GFP$^-$ and GFP$^+$ pontine cells derived from P7, P14 and P28 CGD mice, cultured in EF or EFP media. SVZ cells served as a positive control (n=3 replicates). Arrow pointing sphere count in P28 pontine GFP$^+$ cells in EFP condition. (D) Sphere imaging of P14 GFP$^-$ and GFP$^+$ cells cultured in EF or EFP media. BM: basal medium, no growth factors; B: BDNF, E: EGF, F: FGF, P: PDGF-AA, N: Noggin and S: SAG.

GFP$^+$ and GFP$^-$ cells extracted from both the pons and SVZ (utilizing the latter as a positive control) from mice at P7, P14, and P28. These cells were cultured in either EF or EFP (comprising EGF, FGF, and PDGF-AA) serum free media. For P28 derived pontine GFP+ cells, only a very limited number of cells underwent division, giving rise to neurospheres exclusively under EFP, and not EF, serum free media culture (Figure 2.4C and D). This strongly implies that PDGF-AA is necessary for the activation of these cells. Similar outcomes were also observed in neurosphere assays involving P7 and P14 cells. Importantly, P7 and P14 pontine GFP$^+$ cells formed more spheres than that of P28, suggesting that these stem/progenitors very likely decreased in number from P14 to P28. Moreover, for both pontine and SVZ cells, GFP$^+$ cells had a significantly stronger tendency to form neurospheres than GFP$^-$ cells, with the differences being stronger in the pontine cells. This is in line with our previous study (Xie et al., 2020) and further showed that the CGD transgene has the power to identify stem progenitor cells.

### GFP$^{low}$SOX2$^+$ cells express PDGFRα *in vivo*

Given that PDGF-AA is crucial for GFP+ cells, more so in P28 than P14 and P7, to grow in culture, we next asked whether these cells express PDGFRα *in vivo*.

Immunohistochemistry staining of P28 basilar pons revealed co-localization of GFP and SOX2 along with PDGFRα expression (Figure 2.5A). The expression of PDGFRα suggested the possibility that these cells may be oligodendrocytic precursor cells (OPCs), the stem cell of the oligodendrocytic lineage. Despite these

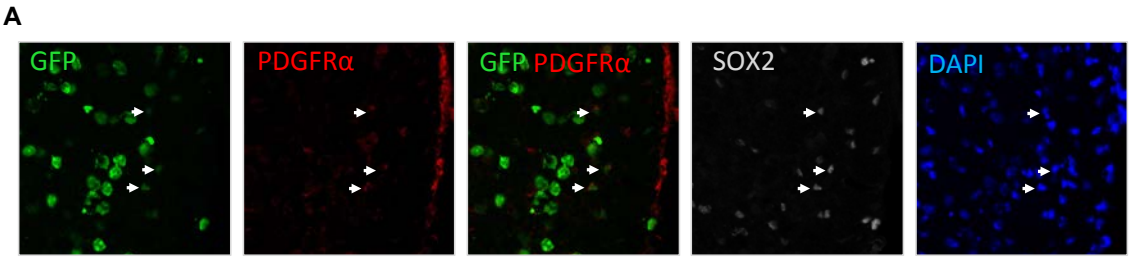


**Figure 2.5. GFP$^{low}$SOX2$^{+}$ cells express PDGFRα *in vivo***
(A) Co-immunostaining of GFP$^{+}$ cells from P28 CGD basilar pons with PDGFRα. Arrows pointed towards co-stained GFP$^{+}$PDGFRα$^{+}$ cells.

GFP$^{+}$SOX2$^{+}$ not expressing OLIG2, past studies have shown that a minor population of the quiescent OPCs do not express OLIG2 (Fang et al., 2023) (Buffo et al., 2005; Ligon et al., 2006). Consequently, the PDGFRα expression observed prompted us to consider that our population of interest may be an OLIG2 negative quiescent OPC.

**Studying the gliomagenesis potential of CGD positive cells in the basilar pons**

As mentioned earlier, the GBM field has generated a variety of different mouse models. Our lab uses Type I and type II tumors.

As mentioned previously, CGD labeled cells are either $GFP^{high}NeuN^{+}$ or $GFP^{low}SOX2^{+}PDGFR\alpha^{+}$. At first glance, this may seem to pose as a problem if we were to induce spontaneous tumor formation since CGD expression also includes neurons. However, this did not dissuade us to investigate the gliomagenesis potential of $GFP^{+}Sox2^{+}PDGFR\alpha^{+}$ since neurons are shown to be incapable of giving rise to tumors (Alcantara Llaguno et al., 2019). The widely accepted paradigm underscores that the cellular origins of glioma emanate from stem progenitor cells, manifesting as neural stem cells (NSCs) or oligodendrocyte precursor cells (OPCs). Furthermore, our laboratory has previously substantiated this finding through the utilization of different mature neuron (*Camk2a*-$creER^{T2}$), immature neurons (*NeuroD1-creER*$^{T2}$) and neuronal progenitor (*Dlx1-creER*$^{T2}$) mouse models to knockout the three most common tumor suppressor genes of GBM: *Nf1*, *Trp53,* and *Pten* (hereafter as *NPP*) in the corresponding mouse neuronal cell types and showed that neuronal lineage cells are incapable of initiating glioma formation (Alcantara Llaguno et al., 2019). Therefore, although the CGD system has the promiscuity of GFP expression in the basilar pons, we focus mainly on the tumorigenic potential of non-neuron $GFP^{+}$ cells ($GFP^{low}SOX2^{+}PDGFR^{+}$) as transgene labeled neurons does not give rise to tumors.

**Knocking out *Nf1*, *Trp53* and *Pten* did not induce proliferation in P28 CGD basilar pons**

To address whether spontaneous tumor formation occurs in adult basilar pons, we administered tamoxifen to P28 CGD mice carrying the *NPP* flox alleles (*Nf1*$^{f/f}$;*Trp53*$^{f/f}$;*Pten*$^{f/+}$) and observe for tumorigenesis over time. However, at P120, these cells remain quiescent as there still remains an absence of Ki67 expression (Figure 2.6A). We did not trace for longer period of time since these mice began to die from tumor arising from the SVZ (type I tumor).

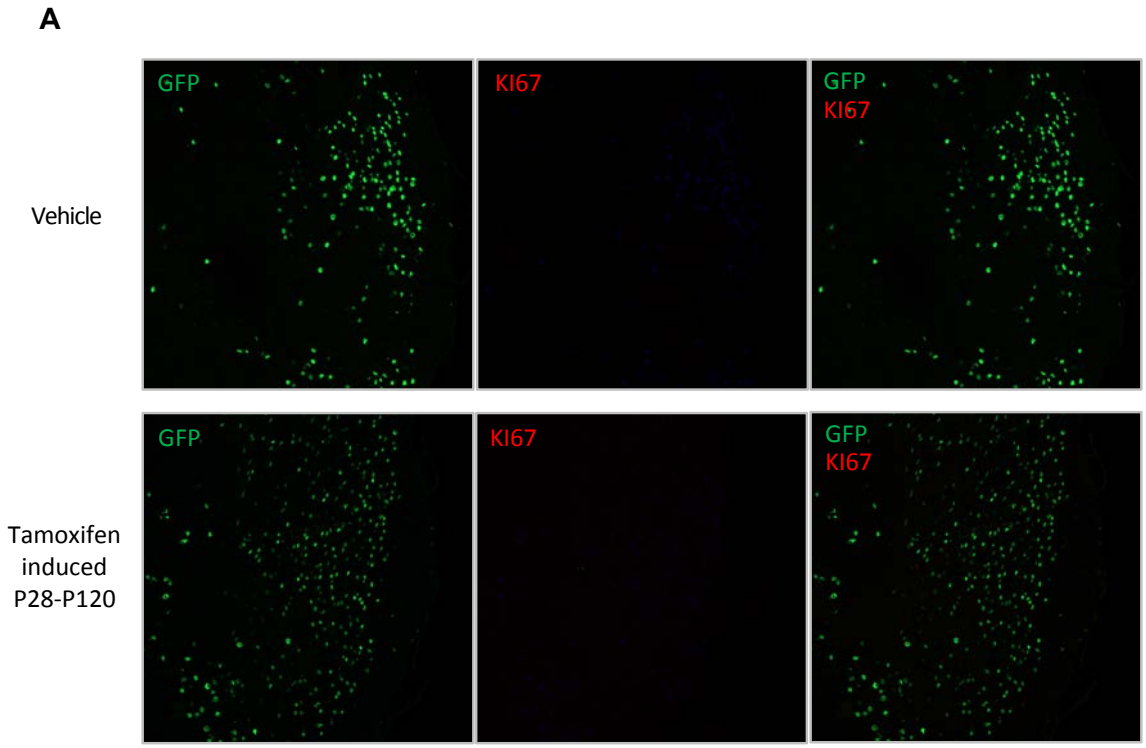


**Figure 2.6. *Nf1*, *Trp53* and *Pten* allele recombination did not induce proliferation in P28 CGD basilar pons.** (A) Immunostaining of KI67 and GFP in the basilar pontine region of P28 CGD mice. Top row: vehicle mice. Bottom row: CGD-NPP mice induced with two consecutive doses of Tamoxifen at P28 and P29 and harvested at P120 for immunostaining analysis.

### *NPP* deleted pontine GFP$^+$ cells can give rise to glioblastoma

The preferred method for exploring the potential of CGD transgene-labeled cells in the basilar pontine region to generate tumors involves the administration of Tamoxifen to P28 *CGD-NPP* mice, followed by observation for tumor development from the basilar pontine region over time. We administered tamoxifen to P28 CGD mice carrying the *NPP* flox alleles (*Nf1$^{f/f}$;Trp53$^{f/f}$;Pten$^{f/+}$*) and observe for tumorigenesis over time. However, at P120, we still did not observe the presence of KI67 in GFP+ cells, suggesting that these cells remain in quiescence. Moreover, due to the predominant expression of the CGD transgene within the NSCs in the SVZ region, mice began to die from SVZ-derived glioma at approximately 3-6 months after Tamoxifen induction. This prevented us from observing the tamoxifen induced mice for tumor arising from the pons. Due to the low number of quiescent GFP$^+$SOX2$^+$ cells in P28 basilar pons, we assume that if tumorigenesis from pontine GFP$^+$ cells would require a longer timeframe as compared to tumors arising from the SVZ (ie. high number of activated neural stem cells). As a result, the conventional approach awaiting tumor formation using the spontaneous mouse model approach is not feasible. Therefore, to avoid being confounding effects from the SVZ-NSC and its derived tumors, our strategy involves transplanting tamoxifen-induced pontine GFP$^+$ cells into recipient mice and monitoring potential for tumor formation. Specifically, we used two slightly different transplantation protocol, namely as the "*in vitro* expansion" and "direct transplantation" method (Figure 2.7A).

The "*in vitro* expansion method" involves the isolation and culture of CGD-expressing pontine cells *in vitro* (Figure 2.7A). The process begins with the isolation of pontine tissue into culture dish with serum free media containing EF, followed by *in vitro* administration of 4-hydroxytamoxifen (4-OH) to induce *NPP* allele recombination. Within three days following the initiation of 4-OH induction, we observed that a minor subset of cells began to undergo rapid cellular proliferation. Notably, the absence of tamoxifen induction resulted in negligible cellular proliferation. Proliferating cells were all GFP positive, showing that it is only CGD transgene expressing cells that underwent *NPP* allele recombination. GFP expression is retained for about a week and began to gradually decline. We cultured the *NPP* KO cells for a total of 14 days (tissue dissociation as day 1) to further expand to cell counts sufficient for intracranial injections. Eventually, 50,000 cells was injected into the striatum of one-month old mice.

The preceding methodology resulted in tumor formation, yet it prompts considerations regarding potential *in vitro* plasticity changes, where cells may assume a more activated or stem-like state (cells bathed in serum free media with EGF and FGF) that may deviate from their original *in vivo* characteristics once there are grown in plastic. In order to address this concern and circumvent such uncertainty, an alternative approach was employed (Figure 2.7A), herein referred to as the "direct transplantation method." Given the limited yield of CGD/GFP cells from pontine dissociation of P28 mice (FACS: GFP+ cells comprise of only 1% of all sorting events), we utilized P7 mice instead to attain a higher yield of GFP+ cells.

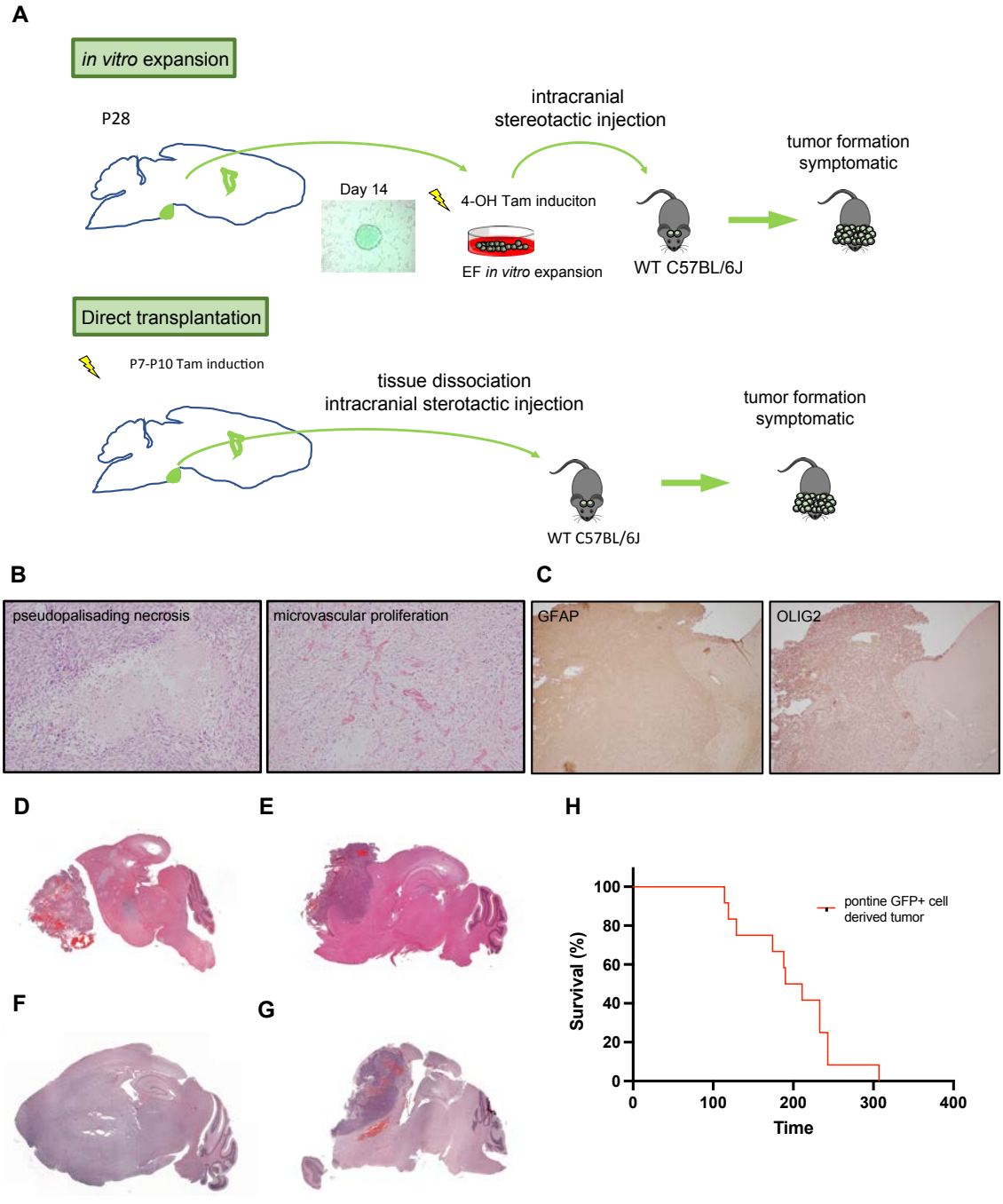


**Figure 2.7. P28 CGD pontine cells are capable of forming GBM.** (A) Diagram of the experimental flow of "*in vitro* expansion" and "direct transplantation method." (B) H&E stainings of CGD pontine derived GBM. (C) GFAP and OLIG2 staining of CGD pontine-derived GBM. (D-G) Whole brain H&E sagittal sections representative of four independent CGD pontine-derived GBMs. (H) Survival analysis of all pooled pontine-derived GBM mice (n=12).

Tamoxifen was administered to P7 *CGD-NPP* mice and pontine tissue was harvested into single cell suspension (15% GFP) at P10, and 10,000 $GFP^+$ cells were immediately transplanted into the striatum of P28 mice. Applying this direct transplantation method to three mice yielded tumors in two instances (Tumor latency: 210 days for PT11 and 129 days for PT25).

We performed hematoxylin and eosin (H&E) staining and immunohistochemistry against GBM clinical pathological markers for all tumors. All tumors presents histology characteristics of human GBM, which includes cellular pleomorphism, high mitotic figures, pseudopalisading necrosis and microvascular proliferation (Figure 2.7B). GFAP and OLIG2 were also highly expressed in these tumors (Figure 2.7C). These pathological findings suggest that the tumors derived from CGD labeled pontine cells (with NPP allele knockout) highly resembled human glioblastoma. Overall tumor histology resembles that of type II tumors with well circumscribed border (Figure 2.7D, E and G) with occasional observation of diffuse tumor (Figure 2.7F). Pooled survival analysis of all CGD pontine cells derived tumors yielded a median latency of 201 days (range: 114-307 days).

**CGD Pontine derived tumors resembles OPC-derived type II tumors**

To determine whether pontine $GFP^+$ cells derived tumors constitute a novel subtype of glioblastoma in addition to type I (*NestinCreER-NPP*) and II (*NG2CreER-NPP*) tumors, we harvested a total of 12 CGD pontine derived tumors (7 from *in vitro* expansion method, 2 from in vivo direct transplantation method)

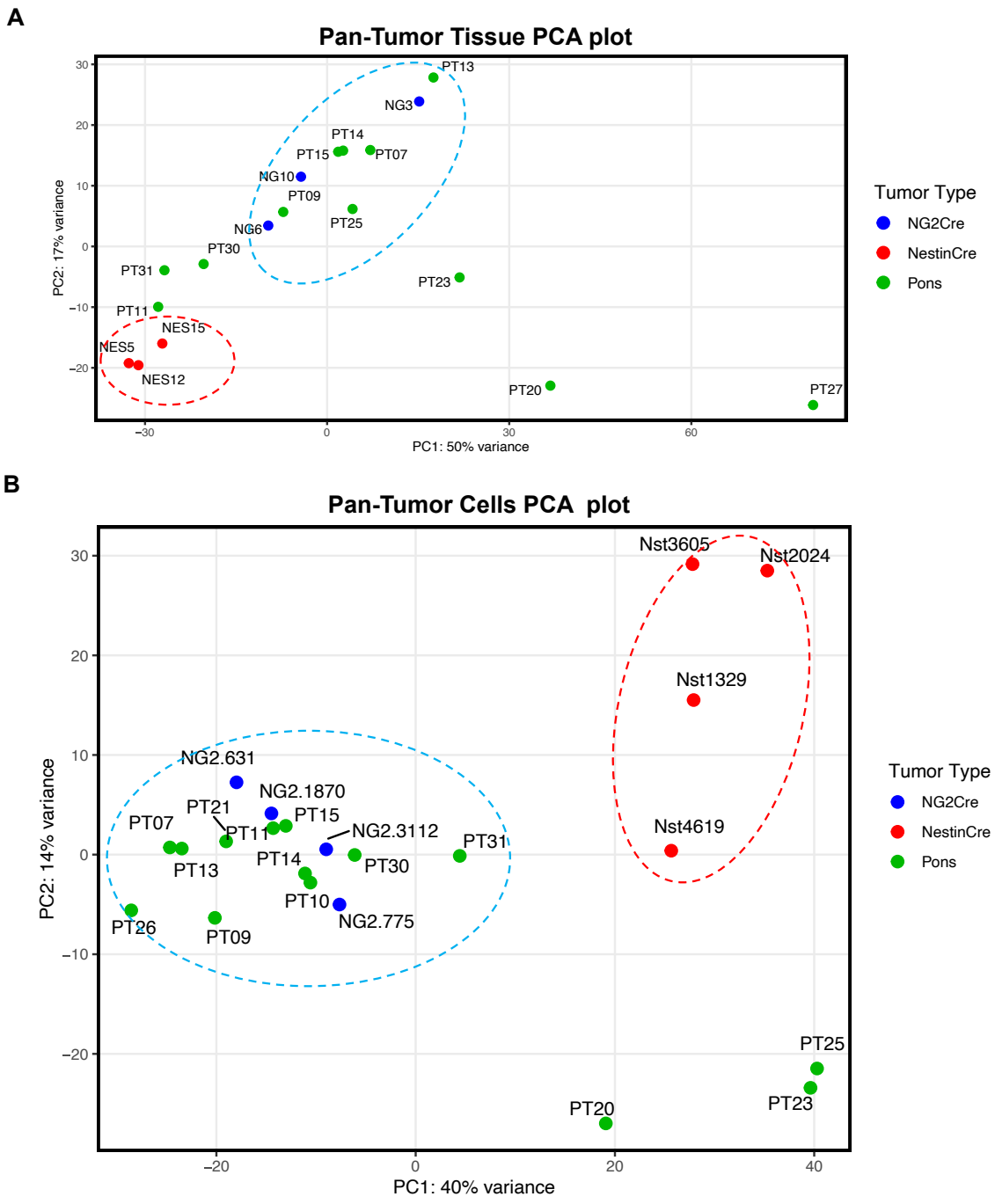


**Figure 2.8. CGD pontine-derived tumors (PT) resembles type II tumors.** (A) PCA plot of transcriptome derived from tumor tissue of NestinCre (type I), NG2Cre (type II) and CGD pontine-derived tumors. (B) PCA plot of transcriptome derived from *in vitro* (Passage number <3) early passage tumor cells of NestinCre (type I), NG2Cre (type II) and CGD pontine-derived tumors.

and 3 of type I and II tumors as subtype controls for bulk-RNA sequencing. To perform unsupervised clustering of the tumors sequenced, we used principal component analysis (PCA) to analyze the transcriptomic data. PCA analysis revealed that type I (NES) and II (NG) tumors clustered separately as expected. A majority of pontine tumors (PT) clustered closely to type II tumors, but three pontine tumors (PT11, PT30 and PT31) clustered in between type I and II tumors (Figure 2.8A).

It has brought to our attention that some of the tumors (PT20, PT23 and PT27) were clustered far away from type I or II tumors. Although this may imply that these tumors may be novel subtypes, we also noticed that there is an increased expression of immune related genes. This raised a technical concern regarding whether the observed expression is due to the contamination by immune cells in the blood due to the lack of tissue perfusion (all tumors were dissected and immediately snapped frozen. No perfusion of mice was performed). Therefore, to ensure that the transcriptome of each tumor samples has high tumor purity, we harvested *in vitro* early passage (less than 3 culture passages) of tumor cells derived from tumor tissue and submitted them for another round of RNA-sequencing. We ensured that primary culture tumor cells consisted only of proliferating tumor cells and were clear of tissue debris.

PCA analysis of tumor cells derived RNA sequencing data showed an even better resolution distinguishing type I and II tumors (Figure 2.8B). We see that the majority of pontine tumors (even that of PT11, PT30 and PT31) clustered closely

to type II tumor cells. Interestingly, we still observed a distant clustering of PT20, PT23 and PT25 away from type I and II clusters.

Therefore, our conclusion is that the majority of pontine tumors (6 out of 12) share expressions resembling that of type II tumors. This similarity implies that the cell of origin of these pontine tumors may be the OPC, which is in line with our characterization of the wildtype $GFP^+SOX2^+PDGFR\alpha^+$ cells.

**A group of non-type I and type II tumors highly expressed mesenchymal genes**

Although not within the scope of this thesis, but in a parallel project in collaboration with Dr. Swathi Iyer of the lab, tumorigenic potential of *CGD-NPP* $GFP^+$ cells isolated from the hypothalamus and dentate gyrus were also investigated using the *in vitro* expansion method. In short, unlike wildtype $GFP^+$ pontine cells, wildtype $GFP^+$ cells from both the hypothalamus and dentate gyrus proliferates spontaneously *in vitro* under SFM-EF condition. Injecting recombined *NPP* $GFP^+$ hypothalamic and dentate gyrus derived cells give rise to high grade glioma also resembling human GBM. Thus, tumors generated from hypothalamus and DG were also submitted together with pontine tumors for bulk-RNA sequencing for subsequent joint analysis.

Additionally, we also included four spontaneous IDH-mutant tumors generated from our *Ng2Cre* transgene harboring *Idh1 R132H* and *Tp53* mutation. The *IDH* mutant tumors were generated by Dr. Chenura Jayewickreme and details of this project is included in his thesis (Jayewickreme *et al*., 2022). The IDH mutant

tumor has been shown to derive from OPC origin. We included the *IDH* mutant tumors to serve as a cell-of-origin control (ie. irrespective of induced mutations: *NPP* vs *IDH1 R132H/Trp53*) and to increase tumor sample numbers to better improve the PCA plot resolution.

The pantumor tissue PCA plot (dentate gryus and mtIDH tumor tissue not available) showed similar findings to what we observed earlier, with the addition that HT2 and HT3 (HT=hypothalamic tumor) tumors are clustered away from type I and II tumors (Figure 2.9A).

The pan-tumor cell PCA plot showed a better clustering resolution (Figure 2.9B). The tumor cell PCA plot showed that the mtIDH tumors clustered very closely with type II tumors as expected. Many hypothalamic and dentate gyrus derived tumors clustered to either type I or II tumors. However, we also noticed an increase in number of tumors that clustered away from type I and II tumors, namely PT20, PT23, PT25, HT02, HT03, DT03, DT05, HT06 and HT01.

Although not within the scope of this thesis, Dr. Swathi Iyer is currently in progress of studying these distantly clustered tumors. We preliminarily named them as “group III” tumors, to distinguish from the known type I and II tumors.

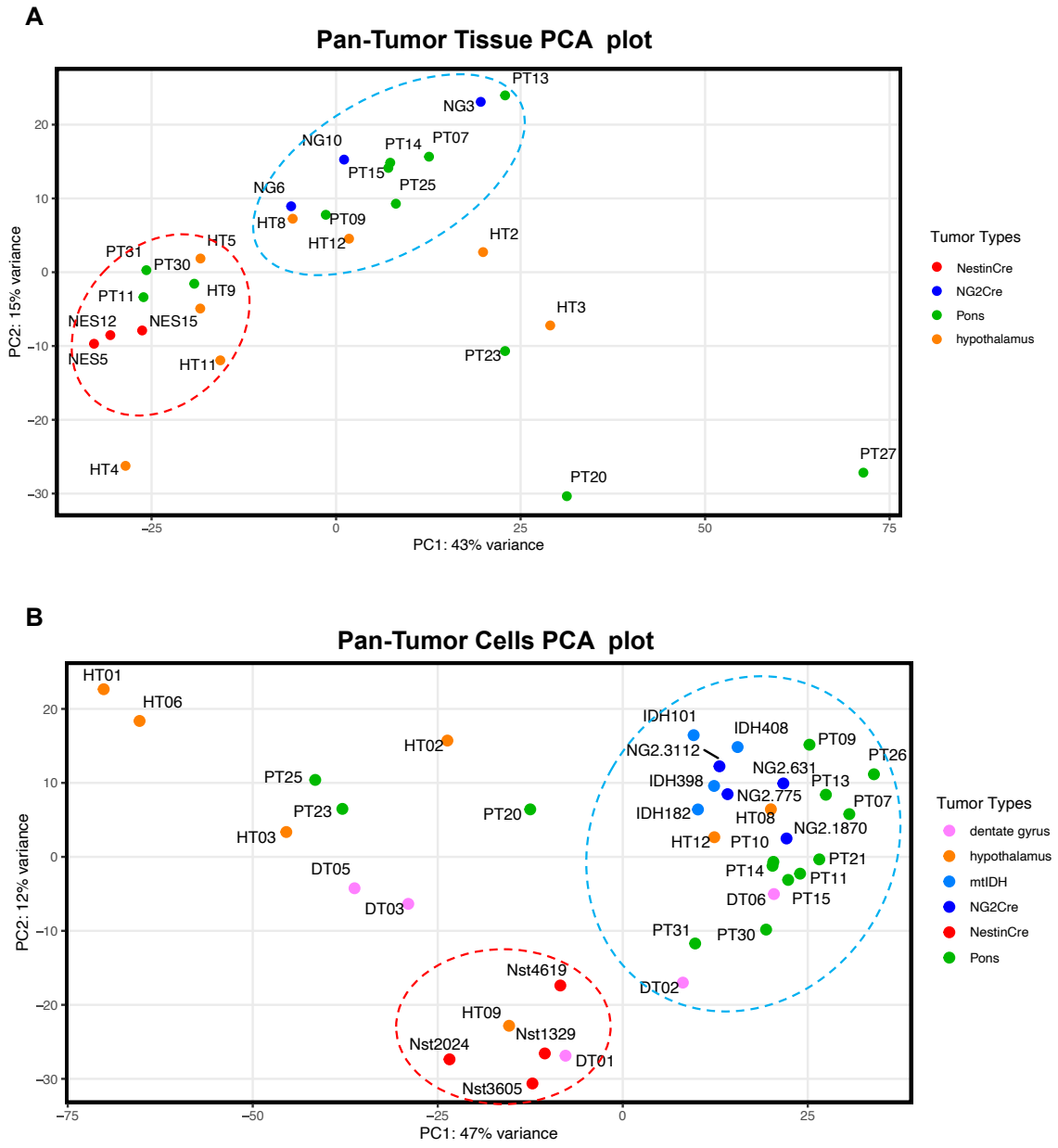


**Figure 2.9. Enrichment of non-type I and II tumors.** (A) PCA plot of transcriptome derived from tumor tissue of *NestinCre* (type I), *NG2Cre* (type II), *CGD* pontine-derived tumors (PT) and *CGD* hypothalamus-derived tumors (HT). (B) PCA plot of transcriptome derived from *in vitro* (Passage number <3) early passage tumor cells of *NestinCre* (type I), *NG2Cre* (type II) and IDH R132H (mtIDH), PT, HT and CGD dentate gyrus-derived tumors (DT).

**Enrichment of an COP genes in PT11, PT30 and PT31 tumors**

Although the overall conclusion drawn from the tumor cell PCA analysis above indicates the close clustering of the majority of pontine tumors with type II tumors, it is noteworthy to mention that PT11, PT30 and PT31 (hereafter as intPT for intermediate pontine tumors) clustered closer proximity to type I tumors in the tumor tissue PCA analysis, as previously mentioned. This observation prompted us to speculate about potential biological pathways specific to *in vivo* intPTs.

Interestingly, upon conducting pairwise differential gene expression analysis between the intPTs and type I or II tumors, enrichment of a subset of oligodendrocytic genes was noted (Figure 2.10A and B). Specifically, these genes were highly specific to the committed oligodendrocytic progenitors (COPs). COP is a nomenclature introduced by the Linnarsson group in 2016, where they performed single cell sequencing on 5072 cells of the oligodendrocytic lineage from 10 different regions of mouse juvenile and adult brain (Marques et al., 2016) (Figure 2.10C). They termed the subsequent developmental stage immediately after OPC as differentiation committed oligodendrocytic precursor, or COP. This population distinctly lacks OPC markers such as *Cspg4/Ng2* or *PDGFRα*. It constitutes a post-mitotic OPC population that has not yet initiated terminal differentiation program. Within the oligodendrocytic research field, previous studies have revealed similar oligodendrocytic entities to COP but are referred differently, such as premyelinating oligodendrocytes, differentiation-committed OPCs (oligodendrocyte precursor cells) and etc (Figure 2.10D). The conspicuous enrichment of COP-specific genes within intPTs in comparison to type I and II

tumors led us to ask whether COP (Figure 2.10A and B), an entity termed by some as differentiation-committeed OPCs, is a potential cell of origin to GBM.

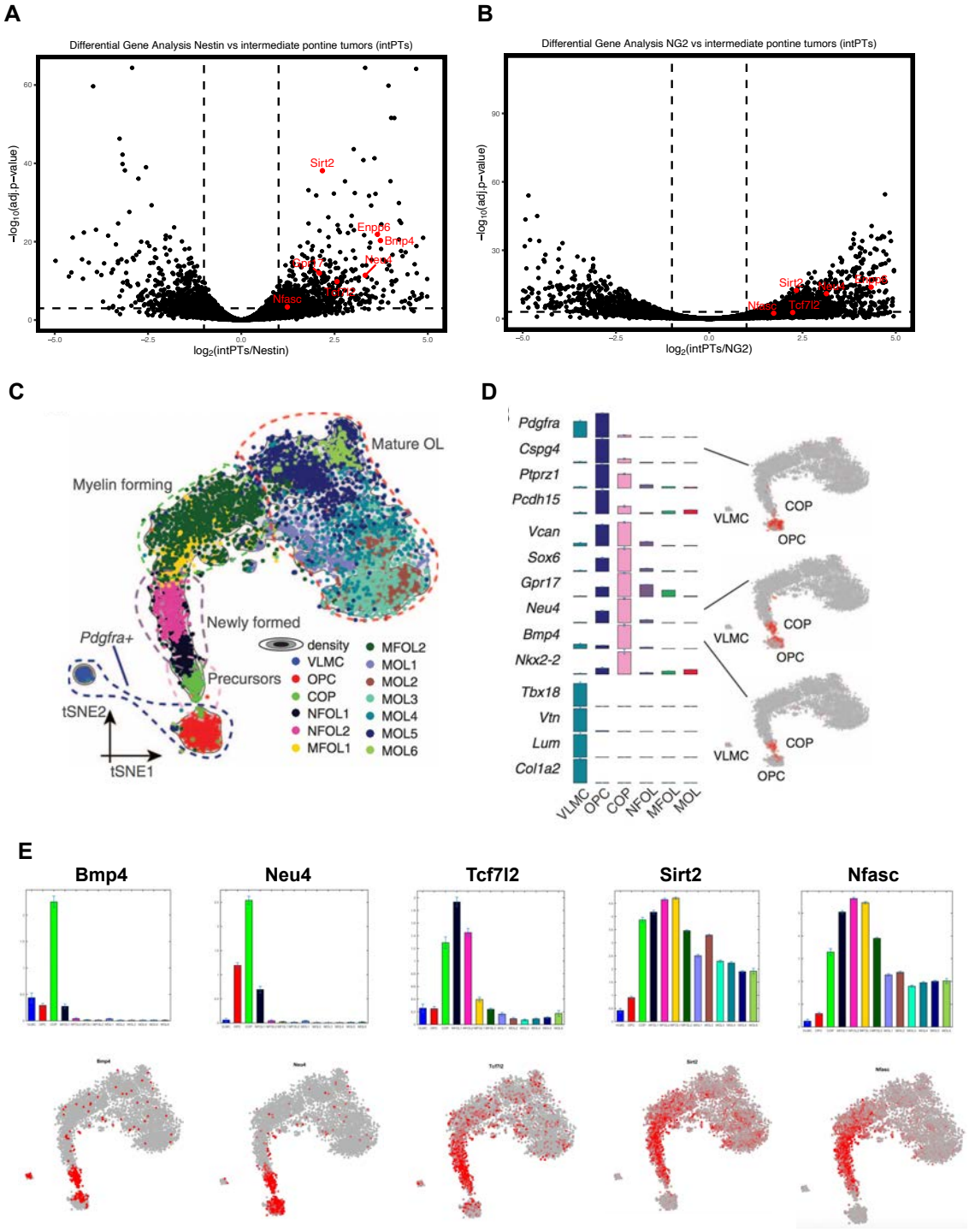

**Figure 2.10. The intermediate pontine tumors are enriched for COP specific genes.** (A and B) Volcano plot of the transciptome between the intPTs (PT11,PT30 and PT31) and (A) type I or (B) type II tumors. Genes highlighted in red are COP-specific genes. (C) tSNE plot showing the trajectory of OPCs to mature oligodendrocytes from the Marques et al. study, featuring a total of 5072 cells. Figure adapted from Marque *et al.* 2016 study. (D) Marker genes specific to each oligodendrocytic stage. Figure adapted from Marque *et al.* 2016 study. (E) COP-specific genes plotted onto the pan-oligodendrocytic tSNE trajectory plot. Data generated from online analytic tool provided on http://linnarssonlab.org/oligodendrocytes.

## CGD/GFP$^{+}$CD9$^{+}$ is a FACS sorting strategy to isolate COPs

To address the potential of COP as the cell of origin of GBM, the ideal approach would be to utilize mice carrying inducible transgene or knock-in construct that labels COPs. Since COP is a new entity, there yet to be defined COP specific markers. Thus, inducing *NPP* allele KO in COP population using spontaneous mouse models remains unfeasible. Thus, our devised experimental approach was to first establish a method to FACS isolate COPs, based on COP-specific cell surface markers. Then by using either the "*in vitro* expansion" or "*in vivo* direct transplantation" methods as mentioned previously, we induce *NPP* allele recombination and intracranially inject *COP-NPP* KO cells to investigate its tumorigenic potential.

To identify a COP-specific cell surface marker, we went back to interrogate the Marques *et al*. oligodendrocyte scSeq dataset. We probed for surface markers and chose CD9 for testing. Based on the Marques *et al*. dataset, CD9 is highly concentrated in the COP population and subsets of the more differentiated myelinating forming oligodendrocytes (MFOL). However, early postnatal mice brain myelination is only in its nascent stage and few oligodendrocytes have

myelination comparable to adult mouse brain. We exploited this property and used early postnatal P7 mice brain as material for isolation and enrichment of COPs.

We dissociated P7 pontine tissue into single cell suspension and used FACS to sort out $GFP^+$ (CGD transgene) cells. Based on PDGFRα (an established OPC marker) and CD9, we further sorted $GFP^+$ cells into four populations: double positive ($PDGFR\alpha^+CD9^+$), single positive ($PDGFR\alpha^+CD9^-$ and $PDGFR\alpha^-CD9^+$) and double negative ($PDGFR\alpha^-CD9^-$). We expect that $PDGFR\alpha^+CD9^-$ to be OPCs and $PDGFR\alpha^-CD9^+$ to be COPs. To validate this, we submitted the sorted cells for bulk RNA-seq to conduct transcriptomics comparison with known OPCs and COP gene signature.

In the pairwise comparison between $PDGFR\alpha^+CD9^-$ and $PDGFR\alpha^-CD9^+$ cell populations, distinct differences were observed, with a principal component analysis (PCA) indicating a PC1 value of 90%, highlighting the robust separation between the two groups. Furthermore, the application of the COP signature generated from Linnarsson dataset revealed a strong enrichment of COP signature genes in the $CD9^+$ group.

Differential expression analysis between the two groups unveiled specific genes displaying significantly elevated expression levels in each population. Within the $PDGFR\alpha^+$ $CD9^-$ group, 2083 genes were upregulated, characterized by pronounced overexpression of PDGFRα (73.5-fold increase), Cspg4/Ng2 (13.0-fold increase), Pcdh15 (4.92-fold increase), and Sox11 (2.46-fold increase). Conversely, the PDGFRα- CD9+ population exhibited 1533 upregulated genes, which includes genes that are highly expressed in the COP population

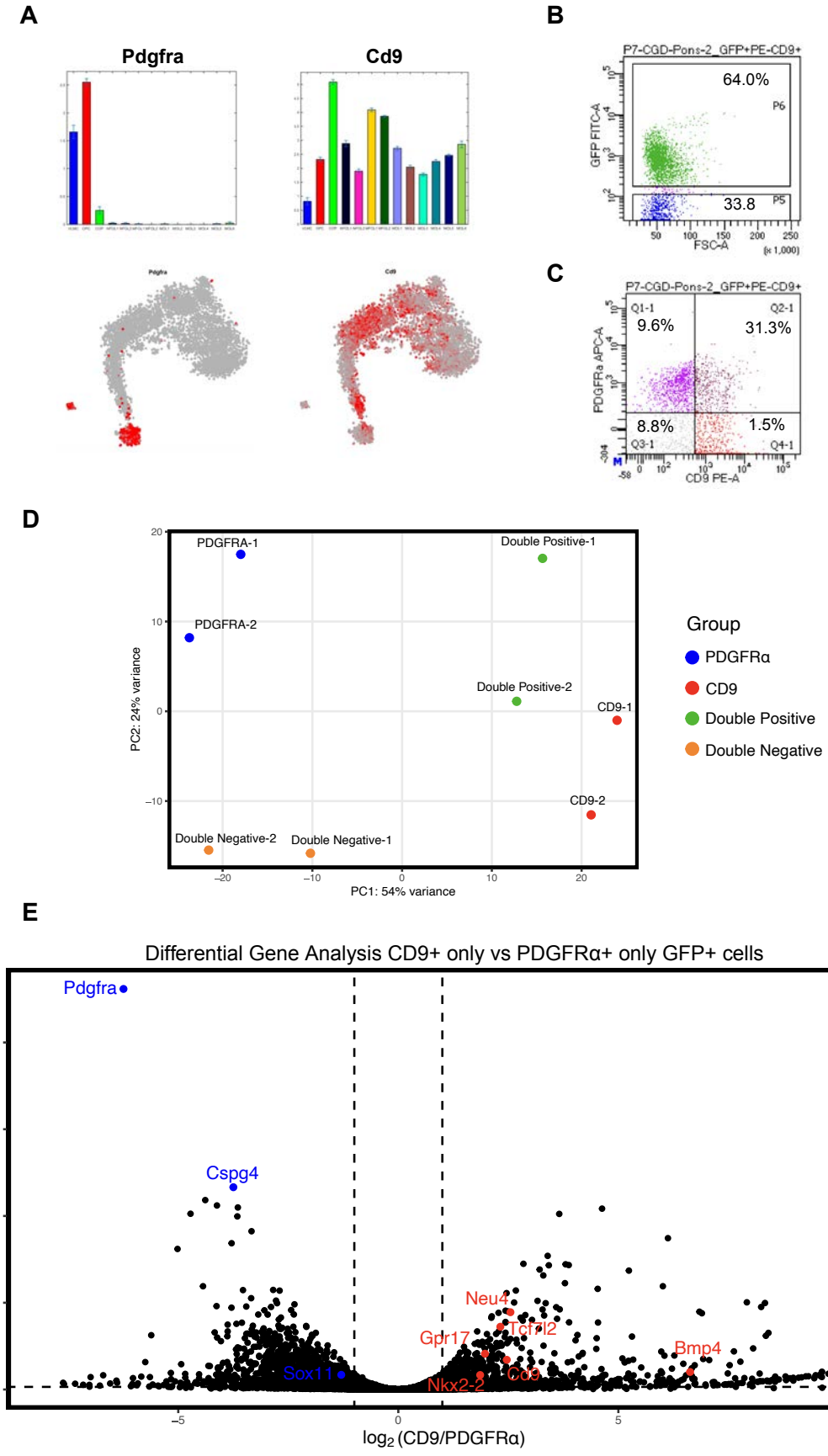
A
Pdgfra
Cd9
B
P7-CGD-Pons-2_GFP+PE-CD9+
64.0%
P6
33.8
P5
GFP FITC-A
FSC-A
(x 1,000)
C
P7-CGD-Pons-2_GFP+PE-CD9+
Q1-1
9.6%
Q2-1
31.3%
8.8%
Q3-1
1.5%
Q4-1
PDGFRa APC-A
CD9 PE-A
D
PDGFRA-1
Double Positive-1
PDGFRA-2
Double Positive-2
CD9-1
CD9-2
Double Negative-2
Double Negative-1
PC2: 24% variance
PC1: 54% variance
Group
PDGFRα
CD9
Double Positive
Double Negative
E
Differential Gene Analysis CD9+ only vs PDGFRα+ only GFP+ cells
Pdgfra
Cspg4
Sox11
Neu4
Tcf7l2
Gpr17
Bmp4
Nkx2-2
Cd9
−log10(adj.p−value)
log2 (CD9/PDGFRα)

**Figure 2.11. CGD coupled with CD9 is a sorting strategy for COP.** (A) Expression fo Pdgfra and Cd9 plotted on the tSNE trajectory plot. (B) FACS analysis of P7 wildtype CGD basiar pontine cells for GFP+ expression. (C) GFP+ cells FACS sorted into four groups based on the cell surface expression of PDGFRα and CD9. (D) PCA plot of the transcriptome of the four sorted populations. (E) Volcano plot of differential gene analysis between PDGFRα$^{-}$CD9$^{+}$ and PDGFRα$^{+}$CD9$^{-}$ transcriptome. Genes highlighted in blue and red are OPC-specific and COP-specific genes, respectively.

(Marques et al., 2016), specifically Bmp4 (24.25-fold increase), Fyn (7.46-fold increase), Neu4 (5.66-fold increase), Cd9 (5.27-fold increase), Tns3 (5.28-fold increase), Tcf7l2 (4.92-fold increase), Nkx2-2 (3.48-fold increase), and Gpr17 (3.73-fold increase). This showed that using CGD/GFP, PDGFRα and CD9 as sorting strategy can isolate and distinguish OPC from COPs.

The dataset presented here, although limited to pairwise comparisons and still requires further experimental validations, marks the first instance of obtaining bulk RNA-seq data from COPs derived from *in vivo* tissue. Our RNA-seq data provided substantial increase in sequencing depth compared to current publicly available scSeq data. Moreover, this sorting strategy provides a potential resource for the oligodendrocytic research community for future research in COPs.

### *Nf1* and Trp53 knockout enhances OPC differentiation towards COP

After establishing a method employing the CGD transgene, we next addressed the effect of *NPP* allele knockout on the dynamic alterations in the proportion of COP cells. We approached this by administering Tamoxifen to early postnatal P7 *CGD-NPP* mice, followed by harvest and dissociation of the pons at P10 to obtain single cell suspensions. Subsequent analysis using flow cytometry

aimed to elucidate changes in the populations of OPCs, OPC/COP transitional cells, and COPs. Our findings reveal that, three days following Tamoxifen induction, a notable increase was observed in the proportion of cells expressing CD9 (both PDGFRα- CD9+ and PDGFRα+ CD9+), concurrently with a decrease in OPCs (PDGFRα+ CD9-) (Figure 2.12B). These results suggest that the abrogation of *Nf1* and *Trp53* (*Pten* is only heterozygous deleted) may contribute to the promotion of OPC differentiation into COPs, or it may suggest that the COP program is needed for tumorigenesis. These findings align with our tumor tissue RNA-seq data.

In summary, we have successfully developed a technique for the isolation of COP and have demonstrated a proportional rise in COP population with the disruption of NPP alleles. Our future endeavors will involve the utilization of this sorting approach to delve into the potential tumorigenic properties of COPs.

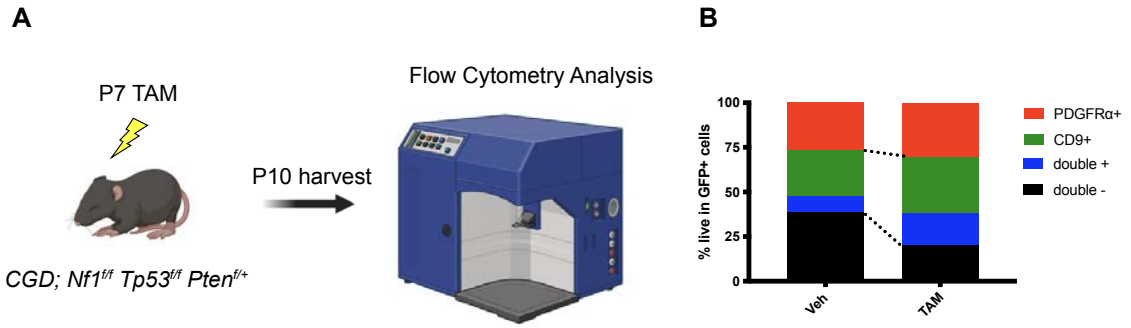


**Figure 2.12. *Nf1* and *Trp53* knockout increases CD9+ population.** (A) Schematic of experimental flow: P7 *CGD-NPP* mice induced with Tamoxifen and harvested at P10 for downstream analysis. (B) Bar plot showing the changes in pontine cell population after tamoxifen induction compared to pontine cells derived from vehicle control-treated mice.

## Discussion

### The precision of CGD as a transgene to label stem progenitor cells

The original intention of developing the CGD transgene, despite a plethora of available *Nestin* transgenic lines, was to generate *Nestin* transgene labeled stem cells that can reflect in real-time the transgene activity with sufficient GFP intensity for FACS sorting purposes. In contrast to the precision exhibited by CGD expression within the SVZ (Xie et al., 2020), wherein it reliably identifies neural stem cells, our data led us to infer that CGD expression within the basilar pons encompasses neurons as well. This likely is attributed to a technical artifact arising from the prolonged half-life of the H2B fusion protein in non-dividing cells, which includes the neurons. However, this artifact did not greatly affect our objective in investigating the tumorigenic potential of $GFP^+SOX2^+$ cells, as demonstrated by the inability of neurons to give rise to tumor in past studies.

### CGD labeled pontine cells are OPCs and give rise to type II tumors

Finding a novel subtype of glioblastoma has been the major goal of this chapter. The entire project is dependent on the ability of *Nestin* transgene to label stem progenitor cells, in the hope that tumors generated therefrom. In summary of the GBM cell of origin investigation studies, by harvesting $GFP^+$ cells from the pons, hypothalamus and dentate gyrus of young adult (P28-P30) CGD mice, we induced *NPP* allele recombination and intracranially implanted these cells to assess their tumorigenic potential. It turns out that *NPP* recombined $GFP^+$ cells from all three regions gave rise to glioblastoma with 100% penetrance. Upon comparing the

transcriptomics of these tumors with that of type I and II tumors, both by tissue and tumor cells, the majority of the pontine tumors clustered closely together with type II tumors. Retrospective analysis of this is in line with the fact that the $GFP^{low}SOX2^{+}$ cells were $PDGFR\alpha^{+}$, which already implied its identity as an OPC. The wildtype study and the tumor study of this project, though no consistent novel subtypes were revealed, were congruent with each other.

**Unexpected modeling of mesenchymal GBM**

Currently, based on human GBM expression datasets, human glioblastoma (GBM) has been stratified into three distinct molecular subtypes: proneural, classical, and mesenchymal. While classical GBM aligned with type I tumors and proneural GBM to type II tumors based on expression and mutation profiles, there exists a notable gap in our understanding of mesenchymal (MES) GBM. MES GBM is often associated with increased immune cell infiltration and *Nf1* mutation. However, MES tumors do not have resemblance to any developmental neural lineage cells and the tumorigenesis mechanism is still unclear. Given the ongoing uncertainty on the cell of origin for MES tumors, generating murine MES GBM mouse model remains a challenge.

Although MES tumors are closely linked to *Nf1* mutation, our generated GEMMs for type I and II spontaneous tumors, despite carrying *Nf1* mutations, did not yield MES tumors. This highlighted that having the *Nf1* mutation alone is insufficient for initiating MES tumor development.

According to our PCA of transcriptomes from all murine GBM tumors we generated in this study, along with type I and II tumors, revealed a subset of tumors distinct from type I and II tumors. We currently termed these outlier samples as “group III” tumors. Remarkably, these group III tumors were enriched in genes associated with the human GBM mesenchymal molecular subtype, particularly those related to inflammation, wound response, angiogenesis and cell migration. Notably, certain group III tumors arised from the pons, which we have shown in Chapter 2 that its cell of origin to be OPCs. This suggests that mesenchymal GBM may not necessarily arise from a different cell of origin but might instead evolve during tumorigenesis through stochastic acquisition of specific mutations or genomic rearrangements.

Taken together, although the study of the pontine tumors has led us to conclude that they give rise to mostly type II tumors, we incidentally generated tumors of a novel subtype akin to the human MES subtype, utilizing the same cell of origin and methodology. For future directions, it would be important to perform whole exome sequencing and even genome-wide CRISPR-Cas9 screens to unveil subtype-specific vulnerabilities within these group III tumors, performed in conjunction with type I and II tumors. This pursuit holds significant potential for unraveling the biology underlying a potential mesenchymal GBM subtype and for identifying subtype specific vulnerabilities.

**Circumventing the need of PDGF-AA in *NPP* recombined pontine GFP$^+$ cells**

A noteworthy observation pertains to the behavior of wildtype cells versus *NPP* recombined GFP$^+$ cells in terms of proliferation stimulation. In the case of wildtype GFP$^+$ cells, the introduction of PDGF-AA (ie., needs EFP) is necessary to trigger proliferation. Conversely, for *NPP* recombined GFP$^+$ cells, the addition of EF suffices. This indicates that the elimination of *Nf1* and *Trp53* (and heterozygous deletion of *Pten*) genes circumvented the need for PDGFRα-dependent signaling for cellular proliferation.

Past studies have shown that loss of *Nf1,* but not *Trp53,* is sufficient for increasing proliferation of OPCs *in vivo (Gonzalez et al., 2018)*. However, a recent study showed that co-deletion of *Pten* and *Trp53* led to OPC proliferation in *Olig1/2-Cre* driven mouse models (Verma et al., 2023). These findings provide insights into how the loss of specific tumor suppressor genes, either individually or in combination, can contribute to OPC proliferation, suggesting their involvement in bypassing the requirement for PDGF-AA to facilitate proliferation *in vitro*. However, it is essential to conduct further experimental investigations to determine the extent to which these *in vivo* findings can be interpreted for *in vitro* studies.

**Widening the applicability of CD9 as a generalized COP marker**

An essential follow up investigation pertains to determining the feasibility of utilizing CGD and CD9 as a FACS sorting strategy for COPs in other brain regions, especially the corpus callosum where the majority of oligodendrogenesis occurs. Past studies have reported CD9 expressions in a minor subset of NG2$^+$ cells (Terada et al., 2002) or myelinated oligodendrocytes (Kagawa et al., 1997). This

is in line with the expression profile of CD9 in the Marques *et al*. data set. Moreover, multiple oligodedrocytic single cell sequencing studies have concluded that unlike astrocytes and neurons where heterogeneity stems from functional specification associated with brain region residence, oligodendrocytic lineage cells are highly homogenous throughout the brain (eg. OPC, COP or NFOLs from different brain regions have minimal differences and clustered together in UMAPs in single cell sequencing analysis) (Marques et al., 2018; Marques et al., 2016; Zeisel et al., 2018). Thus, using only CD9 as a surface marker to FACS sort adult oligodendrocytic cells will result in a mixture of COPs and myelinated oligodendrocytes. In our case, we used early postnatal mice (P7), where myelination is scarce, and the addition of CGD/GFP$^{+}$ to successfully FACS sort COPs. The study of COP-like cells in the past were all done *in vitro* and *in vivo* isolation of COP has not yet been reported. The combination of GFP$^{+}$ and CD9$^{+}$ will be an important tool for the oligodendrocyte research community to study COPs.

Another question to consider is the necessity of CGD for sorting COPs. In the P7 pons, while all PDGFRα$^{+}$ cells are GFP$^{+}$ (data not shown), not all CD9$^{+}$ cells display GFP positivity. This raises the question of whether there exists a difference between CGD$^{+}$CD9$^{+}$ and CGD$^{-}$CD9$^{+}$ cells concerning their stage in the developmental trajectory. Further investigations are warranted to discern potential differences.

While the ability to track individual cell expression was not possible back in the early 2000s, re-analysis of recent single-cell sequencing studies showed that

as OPCs undergo differentiation along its developmental trajectory into COPs entails the immediate increase in CD9. Although CD9 is also expressed in the myelinating oligodendrocytes (MFOLs); however, their number are limited in early postnatal pons. Importantly, CD9 has been deemed non-essential for both oligodendrogenesis and myelination (Terada et al., 2002), thereby establishing its potential as a valuable marker.

**The role of COP population in gliomagenesis**

The observation of an augmented presence of PDGFRα$^{-}$CD9$^{+}$ cells upon the recombination of NPP alleles in *CGD-NPP* mice presents two potential hypotheses. Firstly, it implies that traversing the differentiation path from OPC (the tumor cell of origin) to COP significantly contributes to tumorigenesis. Alternatively, it suggests that COPs themselves might act as a cell of origin for GBM.

Addressing the first scenario presents challenges due to the anticipated enrichment of multiple genes related to COP, rendering a comprehensive gene knockdown unfeasible. Another approach involves silencing a potential master regulator that defines the COP phenotype, albeit necessitating dedicated research efforts.

The second scenario, involving COP as a potential source of GBM initiation, could be experimentally tackled through the GFP$^{+}$PDGFRα$^{-}$CD9$^{+}$ sorting technique coupled with "*in vitro* expansion" or "direct *in vivo* transplantation" methods. Despite pending results due to ongoing experiment optimization within the constraints of time, it remains intriguing to explore whether COPs possess

inherent tumorigenic potential after transitioning away from the OPC state. Moreover, if a tumor arises, the question of whether it manifests as a low or high-grade glioma warrants investigation. Moving forward, it is imperative to invest future exploratory endeavors in addressing these important biological questions.

## Methods

### Animal Studies

All mouse experiments were approved and performed in accordance with the guidelines of the Instiutional Animal Care and Use Committee (IACUC) of Memorial Sloan Kettering Cancer Center. The *CGD* transgene (Xie et al., 2020) was crossed with the *Trp53*$^{f/f}$ (Lin et al., 2004), *Nf1* $^{f/f}$ (Zhu et al., 2001) and *Pten*$^{f/f}$ (Groszer et al., 2001) to generate the *CGD-NPP* (*Nf1* $^{f/f}$, *Trp53*$^{f/f}$, *Pten*$^{f/+}$) mice. Mice were harvested at P120 of age for analysis.

### Lineage tracing

Tamoxifen (Sigma #T5648-5G) was dissolved in sunflower seed oil (Sigma #S5007) and administered by oral gavage (10mg/25g body weight) at a working concentration of 50 mg/ml at P28 of age for two consecutive days.

### Immunofluorescent staining and imaging

Dissected brains were transferred to 30% sucrose PBS for four days, then embedded into frozen blocks with OCT compound (Tissue-Tek). Each brain was sectioned using a cryostat into 10μm sections.

For immunofluorescent staining, slide sections were first preheated on a heat block at 60°C for 30 minutes. Antigen retrieval was performed using a pressure cooker at 95°C for 20 minutes in 10mM sodium citrate buffer, pH 6.0. Slides were then blocked with 10% donkey serum (in PBS-0.1% Triton-X 100) for one hour before overnight primary antibody incubation. Three five-minute washes were performed, followed by a one-hour incubation with the secondary antibody. Three additional five-minute washes were performed, and slides were then bathed in

1:1000 DAPI (in PBST) for 5 minutes before being mounted with Vectashield Mounting Media (Vector Labs). Images were captured using an LSM 800 Confocal Microscope (Zeiss).

**FACS sort**

For sorting P7 and P10 CGD basilar pontine cells, APC Anti-CD140a/PDGFRα (Biolegend #135907) antibody and PE anti-mouse CD9 Antibody (Biolegend #124805) were used. Cells were prepared from dissociating basilar pontine tissues, which then were incubated at 37ºC for 15 minutes with Papain. Antibodies were incubated at 4ºC for 20 minutes according to manufacturer manual prior to FACS sorting.

**EdU pulsing**

5-Ethynyl-2'-deoxyuridine (sc-284628) was added into 30% sucrose water and continuously fed to mice for 3 weeks prior to harvest. Click-iT™ EdU Kit, Alexa Fluor™ 647 dye (ThermoFisher # C10340) was used to detect EdU. EdU detection was done according to manufacture protocol.

**Orthotopic tumor implantation models**

For transplantation experiments, 4 weeks old C57BL/6J mice were used as recipients. All mice were injected with 100,000 *CGD-NPP* recombined cells at the following coordinates: 0.5mm AP, -1.5mm ML, 4.0mm DV with respect to the bregma. Mice developed tumors in the range of 6-10 months.

**Cell culture experiments**

All *in vitro* murine wildtype and tumor cells were maintained in a 5% oxygen cell culture incubator and cultured with serum-free media (SFM). SFM consisted of DMEM/F-12, N2 (GeminiBio #400-163), B27 without vitamin A (Gibco #17-504-044), EGF (10ng/mL; Gibco #PHG0311), bFGF (10ng/mL; Gemini #300-113P), glutamine (Gibco #25030081), sodium pyruvate (Gibco #11360070), penicillin/streptomycin (Gibco #15140122), glucose (Sigma #G8270), bicarbonate (Gibco # 25080-094), and HEPES (Sigma #3375). For *in vitro* recombination induction, 4-hydroxytamoxifen (Sigma #7904-5G) at 4uM concentration was used. After cells were induced with 4-OH for 24 hours, fresh media was replaced. Smoothened agonist SAG (Selleckchem #S7779; working concentration: 100nM) and Noggin (Sigma #250-38-1MG; working concentration: 25ng/mL) were used for testing media formulations optimal for $GFP^+$ pontine cell growth.

**RNA-sequencing**

Upon development of symptoms, tumor tissue were harvested, snap frozen and placed in -80C. Upon preparation for tumor tissue RNA-sequencing, all tumor tissues were thawed out at the same time. For tumor cells RNA-sequencing, fresh tumor-tissue derived cells were cultured for less than 3 passages and then harvested in the same batch for bulk-RNA sequencing.

Total RNA was isolated using the Direct-zol$^{TM}$ RNA MicroPrep (Zymo Research #R2060). Following RNA isolation, total RNA integrity was checked using a 2100

Bioanalyzer (Agilent Technologies, Santa Clara, CA). RNA concentrations were measured using the NanoDrop system (Thermo Fisher Scientific, Inc., Waltham, MA). Preparation of RNA sample library and RNA-seq were performed by the Genomics Core Laboratory at Weill Cornell Medicine. Messenger RNA was prepared using TruSeqStranded mRNA Sample Library Preparation kit (Illumina, San Diego, CA), according to the manufacturer's instructions. The normalized cDNA libraries were pooled and sequenced on Illumina NovaSeq 6000 sequencer with pair-end 50 cycles. The raw sequencing reads in BCL format were processed through bcl2fastq 2.19 (Illumina) for FASTQ conversion and demultiplexing.

The raw reads were then aligned using STAR(version 2.5.3a) with default settings using reference human genome (Ensembl, GRCh37.p13). The counts for each gene were generated by STAR using the commands quantMode and GeneCounts. The R package BiomaRt was utilized to convert mouse Ensembl gene IDs into gene symbols. The R package DESeq2 was used to determine differential gene expression between tumors. Data visualization plots were generated using the R package ggplot2.

## Chapter 3 A brain penetrant Nicotinamide-adenine dinucleotide mimetic impedes de novo guanylate synthesis and glioblastoma growth

### Introduction

The development of effective drugs for glioblastoma (GBM) has been a challenging endeavor. In order to tackle this critical issue in the GBM research field, our laboratory focused on discovering innovative therapeutics for improved GBM treatment. Through a high throughput compound screen, our group sought to identify novel therapeutic compounds with unique mechanisms of action (MoA) that target specific vulnerabilities in tumor cells rather than relying on their proliferative properties. The chemical library workflow is shown below.

With this approach, we successfully narrowed down our initial chemical library, which consisted of 200,000 compounds, to a focused selection of only three highly promising compounds. Among these, we have previously reported the first compound, Gboxin, as a potent oxidative phosphorylation inhibitor that demonstrates remarkable selectivity in targeting GBM cells over replicating astrocytes and MEFs (Shi et al., 2019). The identification of Gboxin's drug target was accomplished through a conventional affinity-based approach for protein target identification. To further elucidate its mode of action, we synthesized several Gboxin analogs that retained their activity. Employing biotin-labeled pull-down assays in conjunction with mass spectrometry, we successfully unraveled that Gboxin binds specifically to proteins associated with the oxidative phosphorylation pathway, with particular enrichment for complex V proteins.

The second compound identified from our chemical library screen is 4C12. To elucidate its mechanism of action, we conducted pathway analysis using microarray data obtained from cells treated with 4C12. Through this analysis, we discovered that 4C12 exerts its effects by suppressing the cholesterol synthesis pathway. Further investigations by Dr. Swathi Iyer, a senior research scientist in our laboratory, revealed that 4C12 specifically targets and inhibits lanosterol synthase (unpublished data). This inhibition disrupts the normal flow of the cholesterol synthesis pathway, leading to a redirection of substrates into an alternative shunt pathway. Consequently, this redirection results in the accumulation of 24,25-epoxycholesterol, which is known to suppress master regulators of cholesterol synthesis and promotes cholesterol efflux-related genes (Brown, 2009). The consequential decrease in cholesterol synthesis significantly decreased the availability of cholesterol, which is crucial for the survival and growth of tumor cells. The findings of the 4C12 study have not yet been published.

The final compound from our chemical library screen is Gliocidin, which was originally referred to as Cpd21. Our lab has previously published a study on Gliocidin's *in vivo* efficacy in targeting malignant peripheral nerve sheath tumors. However, the mechanism of action of Gliocidin and its efficacy for targeting GBM remained unknown for years. This study aims to elucidate the mechanism of action (MoA) of Gliocidin, its drug target and its preclinical efficacy.

## Results

### Gliocidin differentially induces cell death in primary GBM cells and not MEFs

A previous high throughput (>200,000) chemical compound library screen using pooled low passage primary GBM cells derived from multiple spontaneous tumors of the genotype: *hGFAP*-Cre;*Nf1*$^{-/-}$;*p53*$^{-/-}$;*Pten*$^{-/+}$ (hereafter: HTS cells, acronym for **H**igh **T**hroughput **S**creen) (Kwon et al., 2008; Shi et al., 2019), was performed to identify compounds that have half-maximal inhibitory concentrations ($IC_{50}$) in the nanomolar range. A counter screen was performed using primary low-passage replicative MEFs and neonatal astrocytes (not shown) to identify and exclude anti-mitotic agents, which have been predominant in traditional cancer cell line-based screens. Among the few promising hits, we identified a small molecule, here named Gliocidin (N-(Pyridin-3-yl)thiophene-2-carboxamide; Figure 3.1A), that is toxic to primary GBM cells but not to normal dividing primary MEFs (Figure 3.1B). With an $IC_{50}$ of ~200nM, Gliocidin induced apoptosis in HTS cells but not in MEFs, as shown by upregulation of cleaved caspase 3 and cleaved PARP (Figure 3.1C). Cell viability assays done across multiple treatment times and drug concentrations showed decreased cell viability by 18 hours (Supplemental Figure 3.1A) while a drug washout study showed irreversible growth inhibition as early as 6 hours post-Gliocidin treatment (Supplemental Figure 3.1B and 3.1C). Collectively, Gliocidin causes apoptosis in GBM cells. Transcriptomics of Gliocidin-treated HTS cells for 12 hours showed significant changes, while minimal transcriptomic changes were seen in Gliocidin-treated MEFs (Figure 3.1D and 3.1E). Enrichment analysis of the HTS differentially expressed genes after Gliocidin treatment showed upregulation of multiple metabolic processes and downregulation of ribosomal RNA, epigenetic, and other nonspecific gene sets (Supplemental Figure 3.1D and 3.1E). However,

analysis of these data failed to provide direct insights into potential mechanism of action.

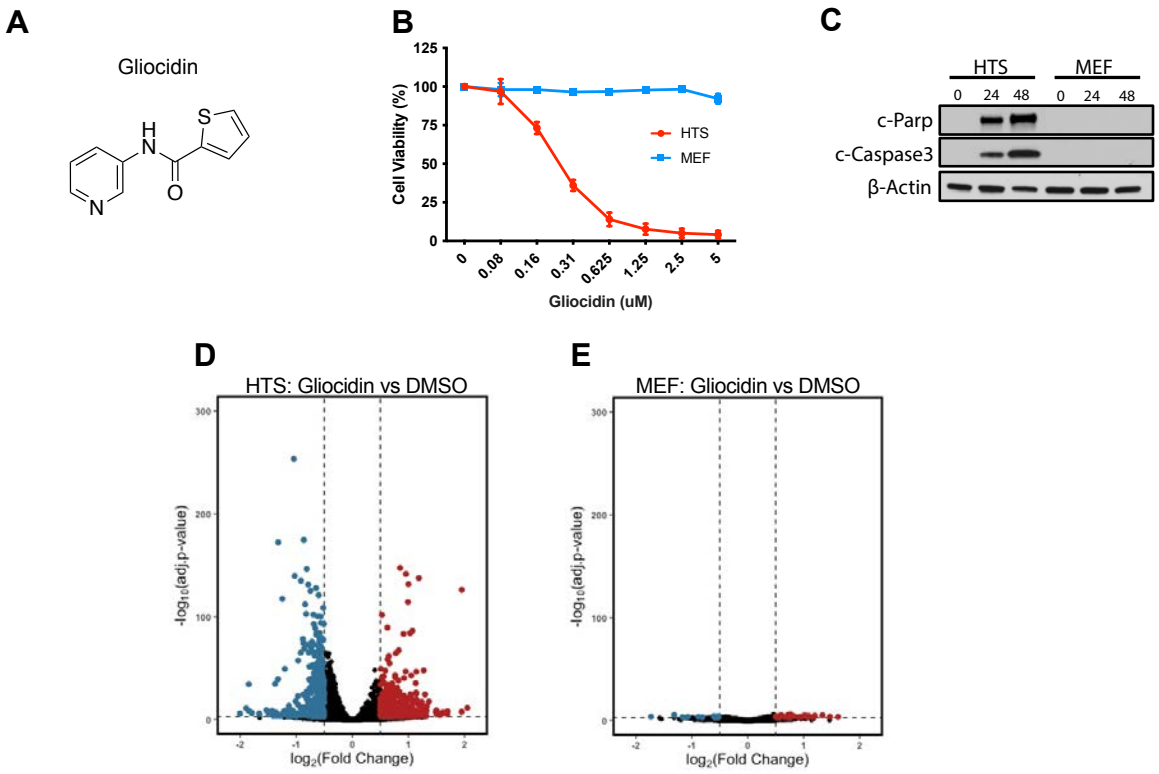


**Figure 3.1. Gliocidin differentially targets GBM over mouse embryonic fibroblasts** (A) Chemical structure of Gliocidin. (B) Gliocidin dose response curve of early passage primary HTS cells and primary MEFs (n=3). (C) Western blot of murine GBM HTS cells and MEFs treated with 1μM Gliocidin over 24-hour intervals probed for c-PARP & cleaved caspase 3 (apoptosis activity). (D and E) Volcano plots depicting transcriptomics of HTS (D) and MEFs

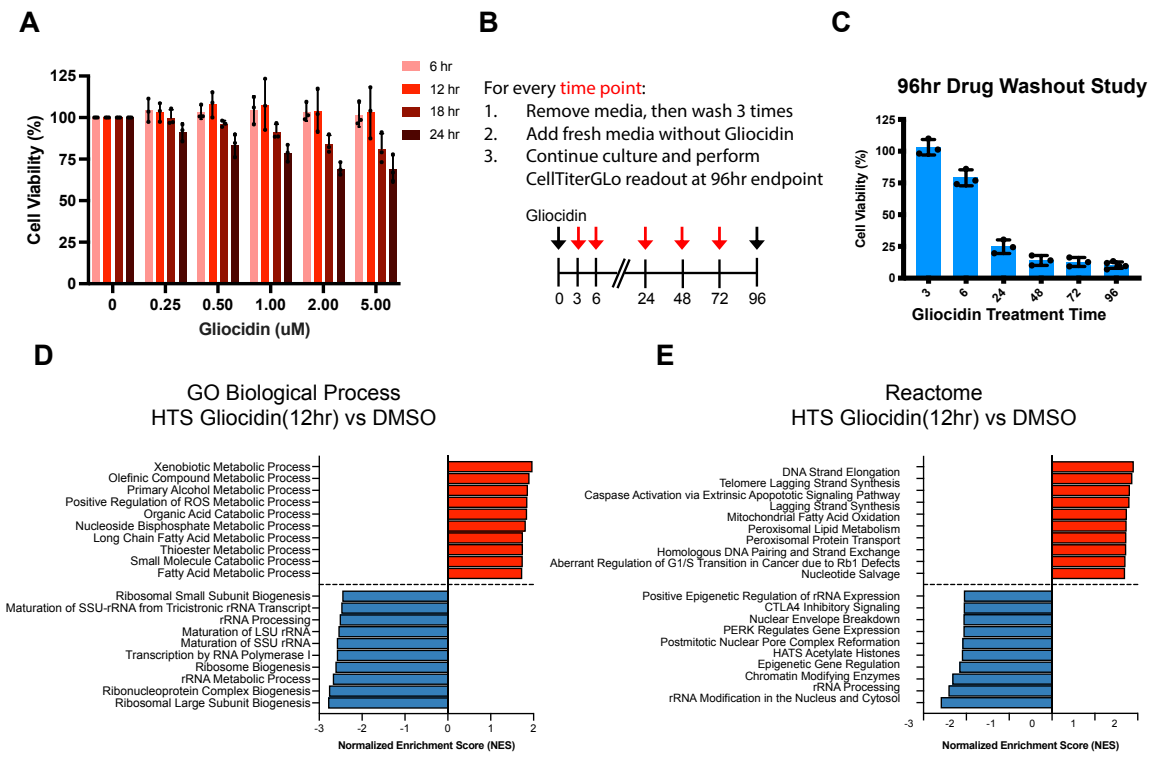


**Supplemental Figure 3.1.** (A) Time course cell viability study of HTS cells treated with increasing concentration of Gliocidin. Data indicate mean ± SD, n=3. (B) Experimental flow of drug washout assay. (C) Drug washout assay of HTS cells treated with Gliocidin for different length of time. Data indicate mean ± SD, n=3. (D) GO Biological Process enrichment analysis of HTS cells treated with 1μM Gliocidin versus DMSO. (E) Reactome enrichment analysis of HTS cells treated with 1μM Gliocidin versus DMSO.

**CRISPR-Cas9 screen reveals mTORC1 modulation of Gliocidin response**

The structure and small molecular weight of Gliocidin (M.W. = 204.25 g/mol) make it a poor candidate for chemical approaches to probe its structure-function profile. We therefore turned to a genetic approach by performing a genome-wide CRISPR-Cas9 screen using the Brie library (Doench et al., 2016) on a primary murine GBM tumor line generated from the *NG2Cre-NPP* (*Nf1*$^{f/+}$,*Trp53*$^{f/f}$,*Pten*$^{f/+}$) spontaneous GBM tumor model, with exogenously delivered Cas9 (NG2-3112 cells; Figure 3.2A). NG2-3112 cells were transduced with lentivirus sgRNA library, puromycin selected and expanded. Then tumor cells were passaged and cultured in the presence of Gliocidin ($IC_{50}$: 250nM or $IC_{80}$: 750nM), or vehicle (DMSO) for 10 doubling generations. Cells were then harvested for DNA extraction, sequencing, and analysis for single guide RNA (sgRNA) enrichment or depletiin Gliocidin treated cells compared to vehicle-treated cells (Figure 3.2B; Supplemental Figure 3.2A).

In this scheme, overrepresentation of targeting sgRNAs in the surviving tumor cells indicated that gene loss protected tumor cells from Gliocidin, while depletion of specific sgRNAs in the surviving tumor cells would indicate that loss of those genes made cells more sensitive to Gliocidin and were therefore selectively lost. Analysis of the top 200 overrepresented sgRNAs (i.e., the genes whose ablation protected tumor cells from Gliocidin) showed enrichment of anabolic pathways such as tRNA modification, *de novo* nucleotide synthesis, protein translation, and ribosome biogenesis (Supplemental Figure 3.2B). By contrast, analysis of top 200 underrepresented sgRNAs (i.e., the genes whose ablation exacerbated Gliocidin

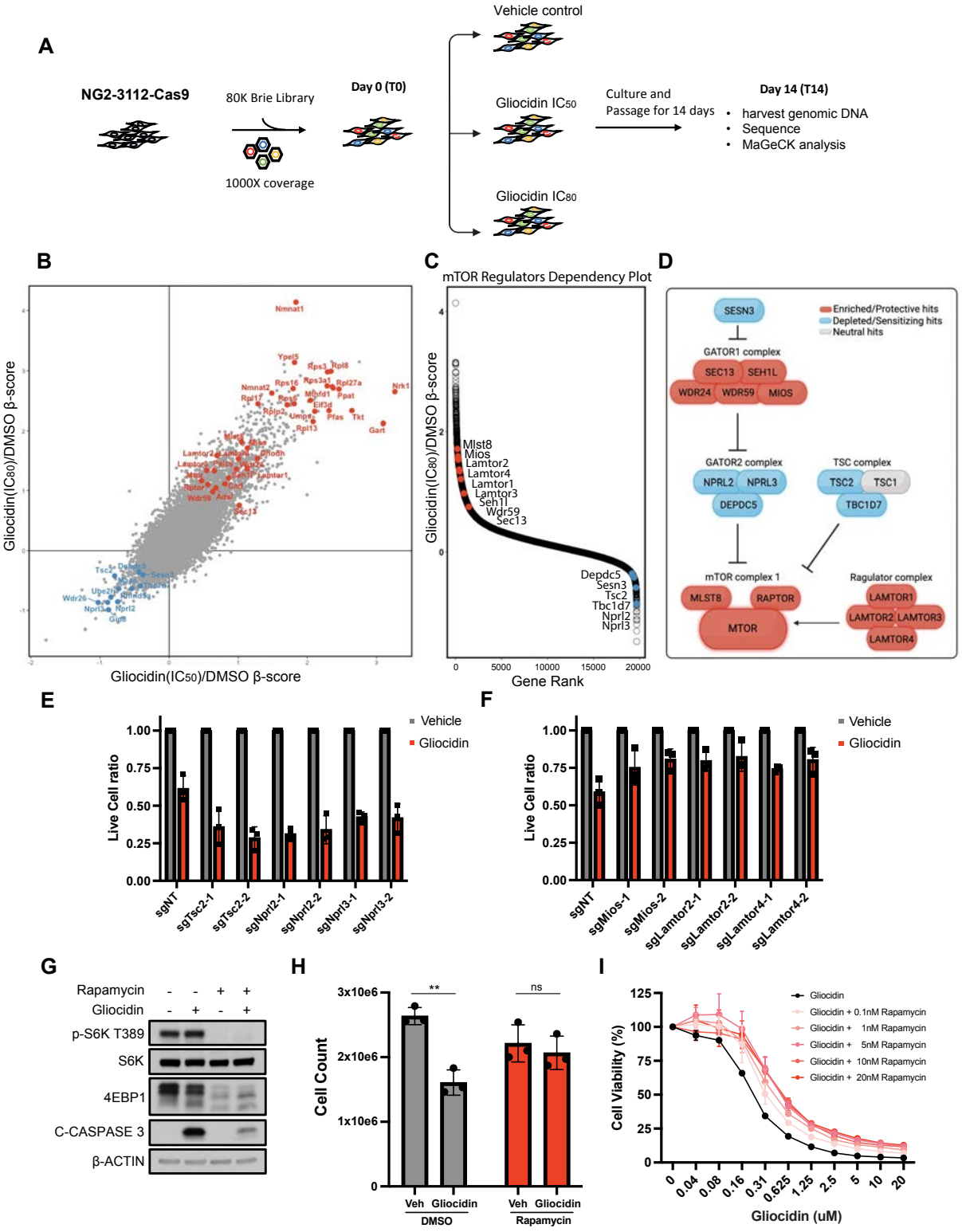
A
NG2-3112-Cas9
80K Brie Library
1000X coverage
Day 0 (T0)
Vehicle control
Gliocidin IC50
Gliocidin IC80
Culture and Passage for 14 days
Day 14 (T14)
harvest genomic DNA
Sequence
MaGeCK analysis
B
Gliocidin(IC80)/DMSO β-score
Gliocidin(IC50)/DMSO β-score
C
mTOR Regulators Dependency Plot
Gliocidin(IC80)/DMSO β-score
Mlst8
Mios
Lamtor2
Lamtor4
Lamtor1
Lamtor3
Seh1l
Wdr59
Sec13
Depdc5
Sesn3
Tsc2
Tbc1d7
Nprl2
Nprl3
Gene Rank
D
SESN3
Enriched/Protective hits
Depleted/Sensitizing hits
Neutral hits
GATOR1 complex
SEC13
SEH1L
WDR24
WDR59
MIOS
GATOR2 complex
NPRL2
NPRL3
DEPDC5
TSC complex
TSC2
TSC1
TBC1D7
mTOR complex 1
MLST8
RAPTOR
MTOR
Ragulator complex
LAMTOR1
LAMTOR2
LAMTOR3
LAMTOR4
E
Live Cell ratio
Vehicle
Gliocidin
sgNT
sgTsc2-1
sgTsc2-2
sgNprl2-1
sgNprl2-2
sgNprl3-1
sgNprl3-2
F
Live Cell ratio
Vehicle
Gliocidin
sgNT
sgMios-1
sgMios-2
sgLamtor2-1
sgLamtor2-2
sgLamtor4-1
sgLamtor4-2
G
Rapamycin
Gliocidin
p-S6K T389
S6K
4EBP1
C-CASPASE 3
β-ACTIN
H
Cell Count
**
ns
Veh
Gliocidin
DMSO
Rapamycin
I
Cell Viability (%)
Gliocidin
Gliocidin + 0.1nM Rapamycin
Gliocidin + 1nM Rapamycin
Gliocidin + 5nM Rapamycin
Gliocidin + 10nM Rapamycin
Gliocidin + 20nM Rapamycin
Gliocidin (uM)

**Figure 3.2. Genome-wide CRISPR-Cas9 Knockout screen of Gliocidin-treated GBM cells.** (A) Schematic of the genome-wide CRISPR-Cas9 screen experimental flow conducted in NG2-Cre derived 3112 murine GBM cells. (B) Merged plot of positively (red) and negatively (blue) enriched sgRNAs shown as β-scores for $IC_{50}$ (x-axis) and $IC_{80}$ (y-axis) Gliocidin-treated cells compared to vehicle-treated cells. (C) Rank order plot highlighting enrichment of sgRNAs for mTOR regulators in the $IC_{80}$ Gliocidin versus vehicle CRISPR-Cas9 screen. (D) Schematic of mTOR regulators color coded by positive or negative β-scores. (E and F) sgRNA validation of selected top (E) depleted and (F) enriched mTOR regulators from the CRISPR-Cas9 KO screen. NG2-3112 cells were treated with 0.125 μM Gliocidin for six days prior to cell counting. Data indicate mean ± SD, n=3. (G and H) Western blot for downstream mTOR effectors and apoptosis (G); and cell count (H) of NG2-3112 cells treated with Gliocidin for 48 hrs with or without rapamycin. For panel (H), data indicate mean ± SD, n=3. $^{**}p<0.01$, n.s., not significant. Two-tailed p values were determined by paired *t* test (I) NG2-3112 cell dose response curves co-treated with a range of Gliocidin concentrations with incremental Rapamycin concentrations (n=3).

activity) showed enrichment of negative mTOR regulators and protein ubiquitination related proteins, specifically the GID (glucose-induced degradation) E3 ligase complex (Supplemental Figure 3.2C and 3.2D). We noticed that the overrepresented anabolic processes are positively regulated by mTOR complex 1 (mTORC1)(Saxton & Sabatini, 2017). Therefore, we inferred that the sensitivity to Gliocidin is mediated by mTORC1 activity. Indeed, focused analysis on mTORC1 pathway regulators showed that sgRNAs for positive mTOR regulators (i.e., *Mlst8*, *Mios*, *Lamtor1-4*, *I1l*, *Wdr59* and *Sec13*) are enriched, while sgRNAs for negative mTOR regulators (i.e., *Tsc2*, *Nprl2*, *Nprl3*, *Tbc1d7*, *Sesn3* and *Depdc5*) are depleted (Figure 3.2C and 3.2D, Supplemental Figure 3.2E). This was further validated when we knocked out a selection of positive and negative mTOR

regulators, which decreased and increased tumor cell sensitivity to Gliocidin,

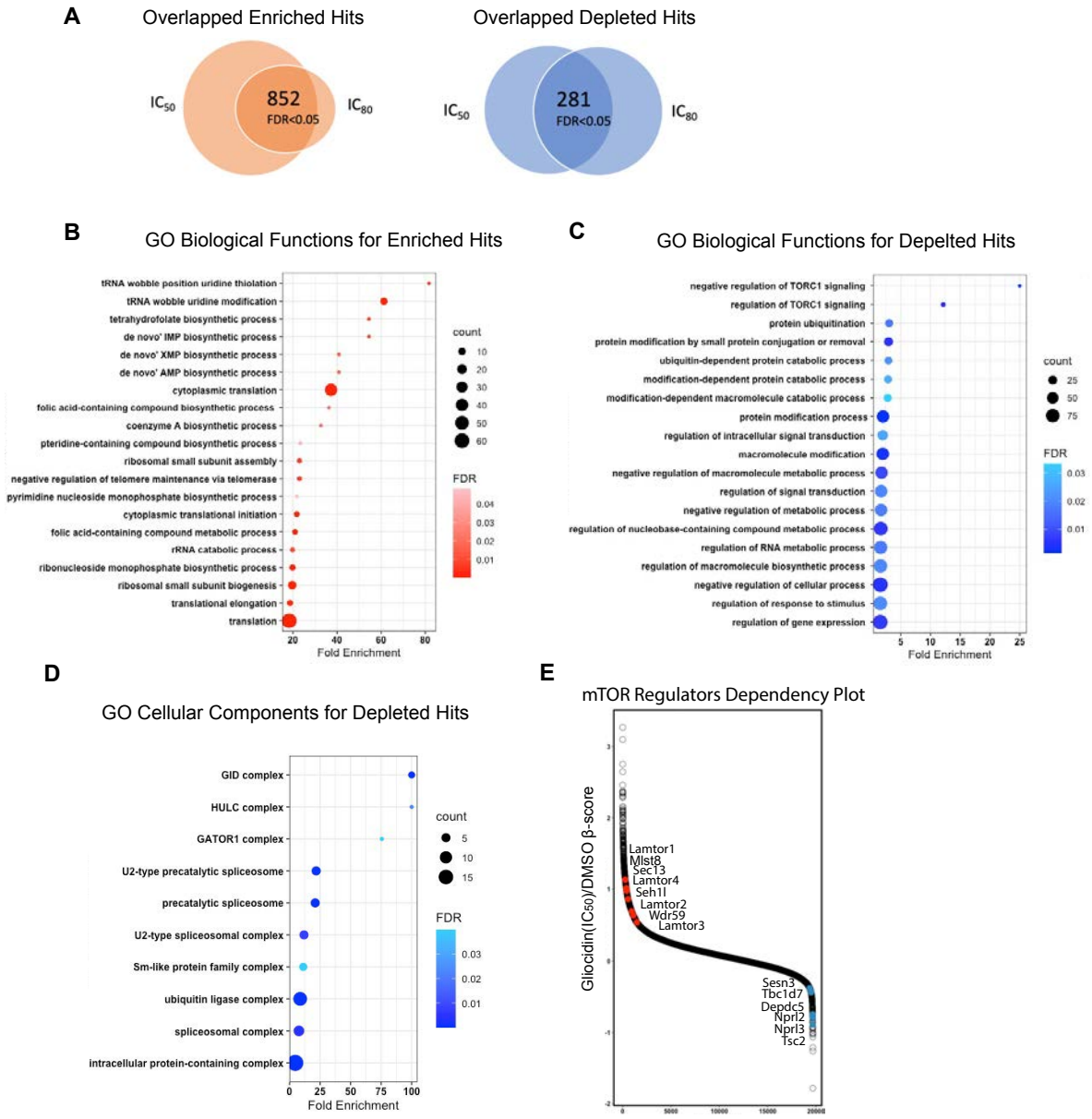


**Supplemental Figure 3.2.** (A) Venn diagram depicting number of overlapped enriched and depleted sgRNAs in $IC_{50}$ and $IC_{80}$ Gliocidin treated cells over vehicle treated cells. Hits are defined as FDR values less than 0.05, as generated by the MAGecK algorithm. (B and C) GO Biological Process enrichment analysis of Gliocidin CRISPR-Cas9 screen (B) enriched and (C) depleted hits. (D) GO Cellular Component enrichment analysis of Gliocidin CRISPR-Cas9 screen (B) enriched and (C) depleted hits. (E) Rank order plot highlighting enrichment of sgRNAs for mTOR regulators in the $IC_{80}$ Gliocidin versus vehicle CRISPR-Cas9 screen.

respectively (Figure 3.2E and 3.2F).

To directly test whether inhibiting mTORC1 activity desensitizes tumor cells to Gliocidin, we co-treated Gliocidin with the mTORC1 inhibitor Rapamycin and observed attenuated Gliocidin induced cell death (Figure 3.2G and 3.2H). In an incremental manner, Rapamycin treatment increased tumor cell tolerance to Gliocidin (Figure 3.2I). Taken together, we conclude that mTORC1 activity plays an important role in determining tumor cell response to Gliocidin.

**Gliocidin inhibits *de novo* guanine nucleotide synthesis**

The inverse correlation of mTORC1-activity with Gliocidin resistance appeared reminiscent of Mizorbine activity, a selective inhibitor of inosine monophosphate synthase 2 (IMPDH2). Thus, active mTORC1 promotes consumption of guanine nucleotides for protein translation and rRNA/ribosome biogenesis, which in the context of IMPDH inhibition, exacerbates a guanosine depletion crisis. We noted a similar inverse correlation of mTORC1-activity with Cpd21 resistance in our CRISPR-Cas9 screen results leading to the hypothesis that Cpd21 may also impede the *de novo* guanine nucleotide synthesis pathway.

Tumor cells with nucleotide deficiency undergo replicative stress (Bester et al., 2011). We therefore performed a time course study of Gliocidin treatment in three different sensitive primary murine GBM cells, NG2-3112, NG2-775 and NST-1329, and found the replication stress marker, phosphorylated Chk1 (p-CHK1), to be induced as early as 3 hours and peaking between 6 and 12 hours (Supplemental Figure 3.3A-C). We next determined whether ribonucleoside supplementation

could reverse Gliocidin tumor cell killing. The results demonstrated that of the four ribonucleosides, only guanosine supplementation rescued Gliocidin induced cell death (Figure 3.3B). Furthermore, this guanosine rescue is entirely dependent on the purine salvage pathway as demonstrated by the blockade of guanosine rescue when *Hprt* is knocked out (Figure 3.3A; Supplemental Figure 3.3D). We extended the guanosine rescue observations to primary orthotopic patient-derived xenograft (PDX) GBM cells (Supplemental Figure 3.3E-G). Finally, guanosine supplement rescued Gliocidin-induced replication stress and cell viability in a dose dependent manner (Figure 3.3D-G and Supplemental Figure 3.3H-I). Thus, in both primary mouse and human GBM cells, Gliocidin induces replicative stress cell death that can be uniquely rescued by guanosine via the purine salvage pathway. Given the inverse correlation between mTORC1 blockade and Gliocidin activity observed in the CRISPR KO screen, we tested whether mTORC1 activity was stimulated following Gliocidin treatment and saw no effect as measured by phospo-S6 kinase levels when replication stress begins (Figure 3.3D and 3.3E).

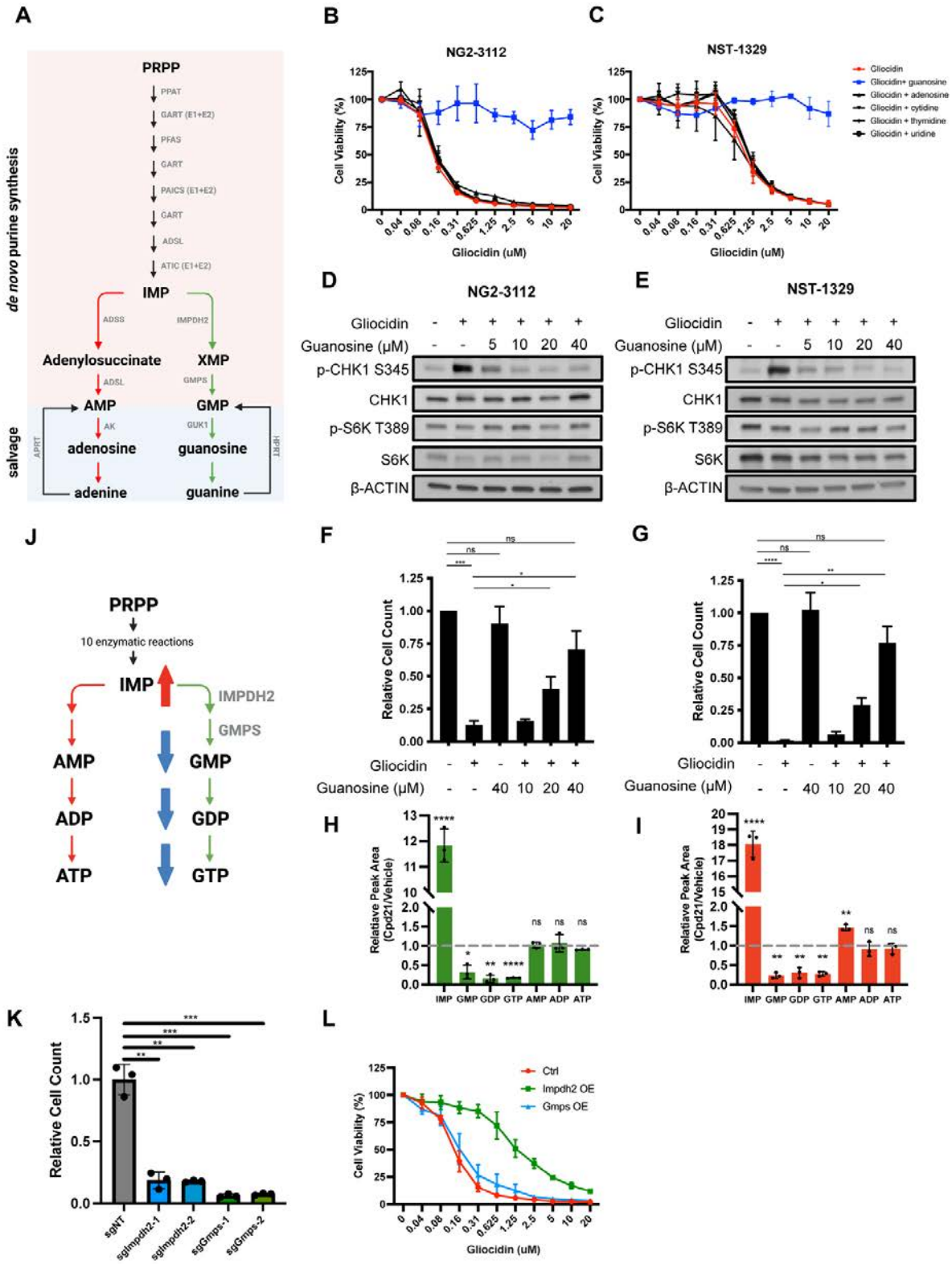
A
de novo purine synthesis
salvage
PRPP
PPAT
GART (E1+E2)
PFAS
GART
PAICS (E1+E2)
GART
ADSL
ATIC (E1+E2)
IMP
ADSS
IMPDH2
Adenylosuccinate
XMP
ADSL
GMPS
AMP
GMP
AK
GUK1
adenosine
guanosine
APRT
HPRT
adenine
guanine
B
NG2-3112
Cell Viability (%)
Gliocidin (uM)
C
NST-1329
Cell Viability (%)
Gliocidin (uM)
Gliocidin
Gliocidin+ guanosine
Gliocidin + adenosine
Gliocidin + cytidine
Gliocidin + thymidine
Gliocidin + uridine
D
NG2-3112
Gliocidin
Guanosine (μM)
p-CHK1 S345
CHK1
p-S6K T389
S6K
β-ACTIN
E
NST-1329
Gliocidin
Guanosine (μM)
p-CHK1 S345
CHK1
p-S6K T389
S6K
β-ACTIN
J
PRPP
10 enzymatic reactions
IMP
IMPDH2
GMPS
AMP
GMP
ADP
GDP
ATP
GTP
F
Relative Cell Count
Gliocidin
Guanosine (μM)
G
Relative Cell Count
Gliocidin
Guanosine (μM)
H
Relatiave Peak Area (Cpd21/Vehicle)
IMP GMP GDP GTP AMP ADP ATP
I
Relatiave Peak Area (Cpd21/Vehicle)
IMP GMP GDP GTP AMP ADP ATP
K
Relative Cell Count
sgNT
sgImpdh2-1
sgImpdh2-2
sgGmps-1
sgGmps-2
L
Cell Viability (%)
Ctrl
Impdh2 OE
Gmps OE
Gliocidin (uM)

**Figure 3.3. Gliocidin targets the *de novo* guanine nucleotide synthesis pathway in GBM cells.** (A) Schematic of *de novo* (pink) and salvage (blue) purine synthesis pathway. (B and C) of NG2-3112 and NST-1329 cell dose-response curves co-supplemented with ribonucleosides (n=3). (D and E) Western blot of Gliocidin-treated with or without guanosine supplementation NG2-3112 and NST-1329 cells probed for replication stress activity. (F and G) NG2-3112 and NST-1329 cell counts after 96-hour Gliocidin treatment, with or without guanosine supplementation. Data indicate mean ± SD, n=3. (H and I) Steady state quantification of the indicated metabolites in (H) NG2-3112 and (I) NST-1329 cells treated 6 hours with 2μM Gliocidin or DMSO, measured by LC-MS/MS. Data shown are fold change difference of metabolite between Gliocidin over DMSO. Data indicate mean ± SD, n=3. ****$p$<0.0001, ***$p$<0.001, **$p$<0.01, *$p$<0.05, ns, not significant. Two-tailed $p$ values were determined by unpaired $t$ test. (J) Schematic of purine metabolite changes upon Gliocidin treatment. (K) Cell counts of non-targeting control, *Impdh2* and *Gmps* knockout NG2-3112 cells (n=3). (L) NG2-3112 cell dose-response curve comparing vector control, with overexpressed (OE) *Gmps* or *Impdh2* cDNA treated with Gliocidin (n=3).

Effective enzymatic blockade of the anabolic purine synthesis pathway would predict accumulation of upstream precursors and depletion of downstream intermediates. We therefore next measured and compared the purine metabolite level between Gliocidin and vehicle treated cells using liquid chromatography with tandem mass spectrometry (LC-MS/MS). We observed a significant accumulation of inosine monophosphate (IMP;10-22 fold) upstream of IMPDH2 activity and a drastic reduction of the immediate downstream product guanine nucleotides GMP, GDP and GTP (Figure 3H, 3I, 3J, and Supplemental Figure 3J). These results drew focus on the steps catalyzed by the enzymes, IMPDH2 and GMPS as the primary target candidates for Gliocidin mediated blockade of guanylate synthesis (Figure 3J). In alignment with our CRISPR-Cas9 screen results, directed CRISPR

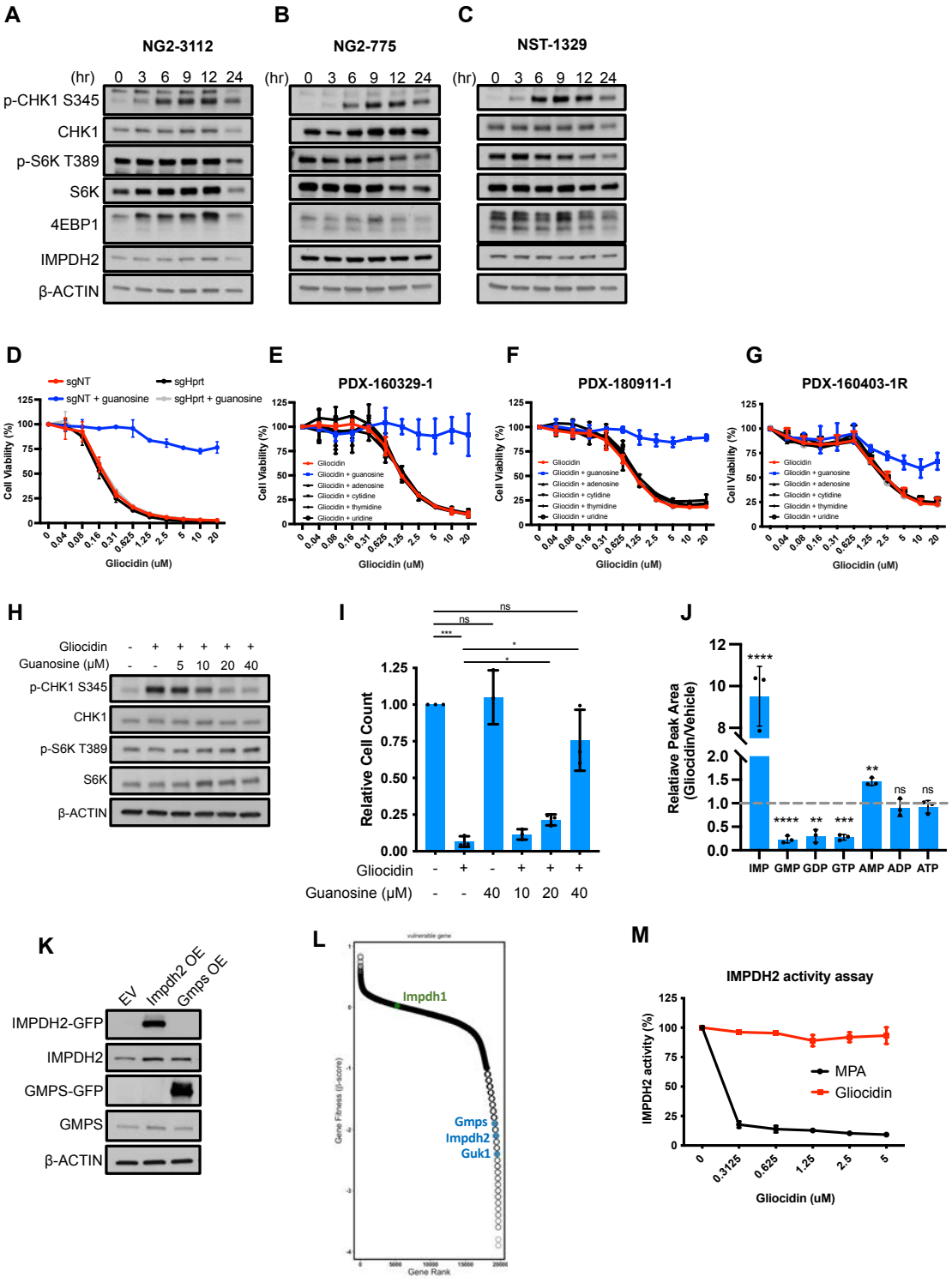
A
NG2-3112
(hr) 0 3 6 9 12 24
p-CHK1 S345
CHK1
p-S6K T389
S6K
4EBP1
IMPDH2
β-ACTIN
B
NG2-775
(hr) 0 3 6 9 12 24
C
NST-1329
(hr) 0 3 6 9 12 24
D
sgNT
sgHprt
sgNT + guanosine
sgHprt + guanosine
Cell Viability (%)
Gliocidin (uM)
E
PDX-160329-1
Gliocidin
Gliocidin + guanosine
Gliocidin + adenosine
Gliocidin + cytidine
Gliocidin + thymidine
Gliocidin + uridine
F
PDX-180911-1
G
PDX-160403-1R
H
Gliocidin - + + + + +
Guanosine (μM) - - 5 10 20 40
p-CHK1 S345
CHK1
p-S6K T389
S6K
β-ACTIN
I
Relative Cell Count
Gliocidin - + - + + +
Guanosine (μM) - - 40 10 20 40
J
Relative Peak Area (Gliocidin/Vehicle)
IMP GMP GDP GTP AMP ADP ATP
K
EV
Impdh2 OE
Gmps OE
IMPDH2-GFP
IMPDH2
GMPS-GFP
GMPS
β-ACTIN
L
Impdh1
Gmps
Impdh2
Guk1
Gene Fitness (β-score)
Gene Rank
M
IMPDH2 activity assay
IMPDH2 activity (%)
MPA
Gliocidin
Gliocidin (uM)

**Supplemental Figure 3.3** (A to C) Western blot of (A) NG2-3112, (B) NG2-775 and (C) NST-1329 treated with 1μM Gliocidin across different time points, probed for replication stress and mTORC1 activity markers. (D) Gliocidin dose response curve of non-targeting control (NT) or *Hprt* knockout NG2-3112 cells co-supplemented with or without 20μM guanosine (n=3 biological replicates). (E-G) Gliocidin dose-response curves of different PDX GBM cells co-supplemented with or without ribonucleosides (n=3). (H) Western blot of Gliocidin-treated NG2-775 cells co-supplemented with or without guanosine, probed for replication stress markers. (I) Cell counting of NG2-775 cells treated with Gliocidin for 96 hours, with or without guanosine supplementation. Data indicate as mean ± SD, n=3. ****$P$<0.0001, ***$P$<0.001, **$P$<0.01. Two tailed $p$ values were determined paired student's $t$ test. (J) Steady state quantification of the indicated metabolites in NG2-775 cells treated with 6 hours 2μM Gliocidin or DMSO, measured by LC-MS/MS. Data shown are fold change difference of metabolite between Gliocidin over DMSO. Data indicate mean ± SD, n=3. ****$p$<0.0001, ***$p$<0.001, **$p$<0.01, n.s., not significant. Two-tailed $p$ values were determined by unpaired $t$ test. (K) Western blot of *Gmps* and *Impdh2* overexpressing NG2-3112 cells in experiment Figure 3L. (L) Rank-order plot of NG2-3112 essential genes shown as

knockout (KO) of the *Impdh2* and *Gmps* genes in NG2-3112 GBM cells, caused cell death (Figure 3.3K). However, overexpression of *Impdh2* but not of *Gmps* provided rescue to Gliocidin indicating that IMPDH2 marks the rate limiting step (Figure 3.3L, Supplemental Figure 3.3K). *Impdh1*, which is primarily expressed in non-dividing cells, is not a vulnerable gene in NG2-3112 cells (Supplemental Figure 3.3L).

To test whether Gliocidin directly inhibits IMPDH2 enzymatic activity, we performed *in vitro* enzymatic assays using the well-established IMPDH inhibitor Mycophenolic (MPA, the active form of Mycophenolate Mofetil, or MMF, CellCept®) as a positive control. Results indicated that in contrast to MPA inhibition of IMPDH2 activity, Gliocidin itself had no inhibitory effect (Supplemental Figure 3.3M). Thus, either Gliocidin acts indirectly on IMPDH activity, or it requires cellular context to be modified into an active form.

**Nucleotide synthesis dependency switch in GBM contributes to Gliocidin resistance**

We also noticed from our CRISPR screen analysis that knock out of the *de novo* nucleotide synthesis enzymes contributes to Gliocidin resistance. At first glance, it may seem counterintuitive given that knockout of these essential enzymes conferred Gliocidin resistance to tumor cells. However, the CRISPR screen analysis for identifying Gliocidin resistance and sensitive genes is based on the sgRNA reads between Gliocidin-treated and DMSO-treated cells and is irrespective of gene essentiality.

Considering the nucleotide synthesis in cells can occur through either the *de novo* pathway or the salvage pathway, we formulated a hypothesis that knocking out the *de novo* genes would prompt the cells to shift their nucleotide synthesis dependency towards the salvage pathway. We first showed that knockout of the salvage pathway gene hypoxanthine-guanine phosphoribosyltransferase (*Hprt*) did not affect steady state NG-3112 cell growth (Supplemental Figure 3A). This showed the NG2-3112 cells do not rely on the salvage pathway to proliferate *in vitro*. Next, to validate our hypothesis, we conducted experiments to knock out specific *de novo* purine synthesis (DNPS) genes, namely *Pfas*, *Ppat*, and *Gart*, and treated the cells with Gliocidin (Supplemental Figure 3.4B). The results showed that the knockout of these genes made the tumor cells less responsive to Gliocidin compared to the non-targeting control cells.

To further investigate the nucleotide dependency switch, we sought to inhibit the salvage pathway, which could potentially re-sensitize the DNPS gene knockout

cells to Gliocidin. To achieve this, we performed double CRISPR knockouts of *Hprt* along with *Pfas*, *Ppat*, or *Gart*. It is important to note that *Hprt* is not an essential enzyme for NG2-3112 cells under normal conditions. Nevertheless, *Hprt* knockout increased the sensitivity of NG2-3112 cells to Gliocidin, although not to a statistically significant extent. As expected, the double knockout of *Hprt* with *Pfas*, *Ppat*, or *Gart* reversed the Gliocidin resistance observed in the single knockout cells (Supplemental Figure 3.4B).

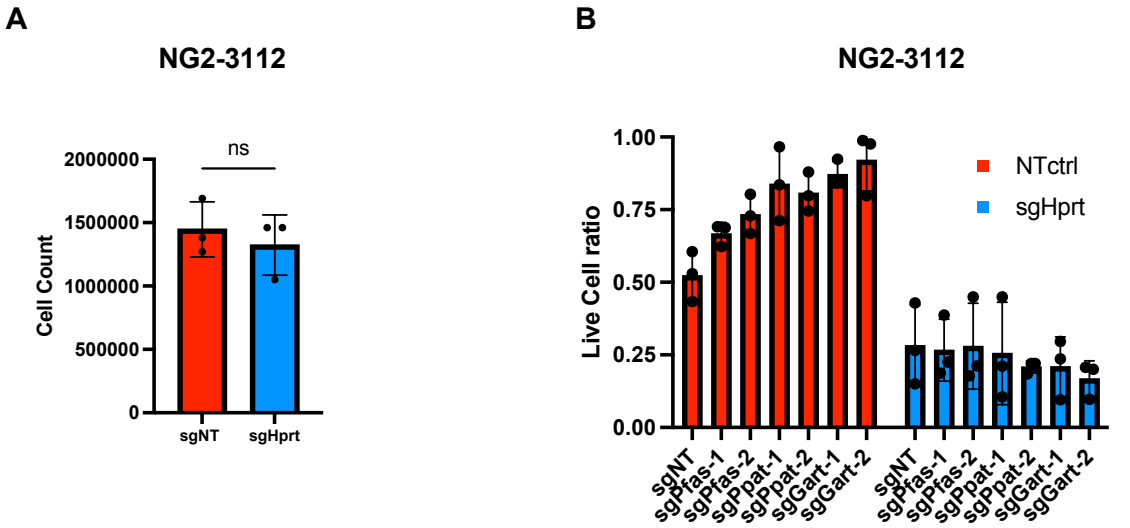


**Supplemental Figure 3.4** (A) Cell count of non-targeting (NT) and *Hprt* KO NG2-3112 cells that were cultured for 6 days. (B) NT and Hprt1 KO cells with additional *de novo* purine synthesis gene KO were treated with 0.125 μM Gliocidin. Cells were counted six days after treatment. Data indicate mean ± SD, n=3.

These findings indicate three critical insights: Firstly, NG2-3112 cells primarily rely on the de novo pathway for survival in a drug-free state. Secondly, when the *de novo* purine synthesis pathway is inhibited (by Gliocidin targeting IMPDH2), the cells exhibit an increased reliance on the salvage pathway for survival. Lastly, when both *de novo* and *salvage* pathways are inhibited, NG2-3112 cells lose their

last remaining source of nucleotides and succumb to Gliocidin exposure. This underscores the significance of the nucleotide synthesis dependency plasticity in the context of Gliocidin resistance in tumor cells.

**$NAD^+$ salvage pathway enzymes are required for Gliocidin activity**

The genome-wide CRISPR-Cas9 screen data had also revealed that following Gliocidin exposure, genes encoding enzymes of the $NAD^+$ salvage pathway ranked high among the positively enriched sgRNA guides (Figure 3.4A). Nicotinamide riboside kinase (NRK1) catalyzes the phosphorylation of nicotinamide riboside (NR) to nicotinamide mononucleotide (NMN), while nicotinamide nucleotide adenylyltransferases (NMNAT1 and NMNAT2) catalyze the transfer of AMP to NMN (Figure 3.4B). We first validated the screen results by individually knocking out *Nmnat1*, *Nmnat2* and *Nrk1* in NG2-3112 and NST-1329 primary tumor cells. In both GBM lines, knockout of *Nmnat1* promoted Gliocidin resistance by shifting the $IC_{50}$ to greater than 5μM, and though less pronounced, *Nrk1* knockout also shifted the $IC_{50}$ significantly (Figure 3.4C). *Nmnat2* knockout conferred mild resistance to Gliocidin in NG2-3112 but not in NST-1329 GBM cells. NMNAT1 and Nmnat2 are isozymes with 35.3% identity and 53.8% amino acid similarity. Quantitative proteomics of the NG2-3112 and NST-1329 GBM cell lines failed to detect NMNAT2

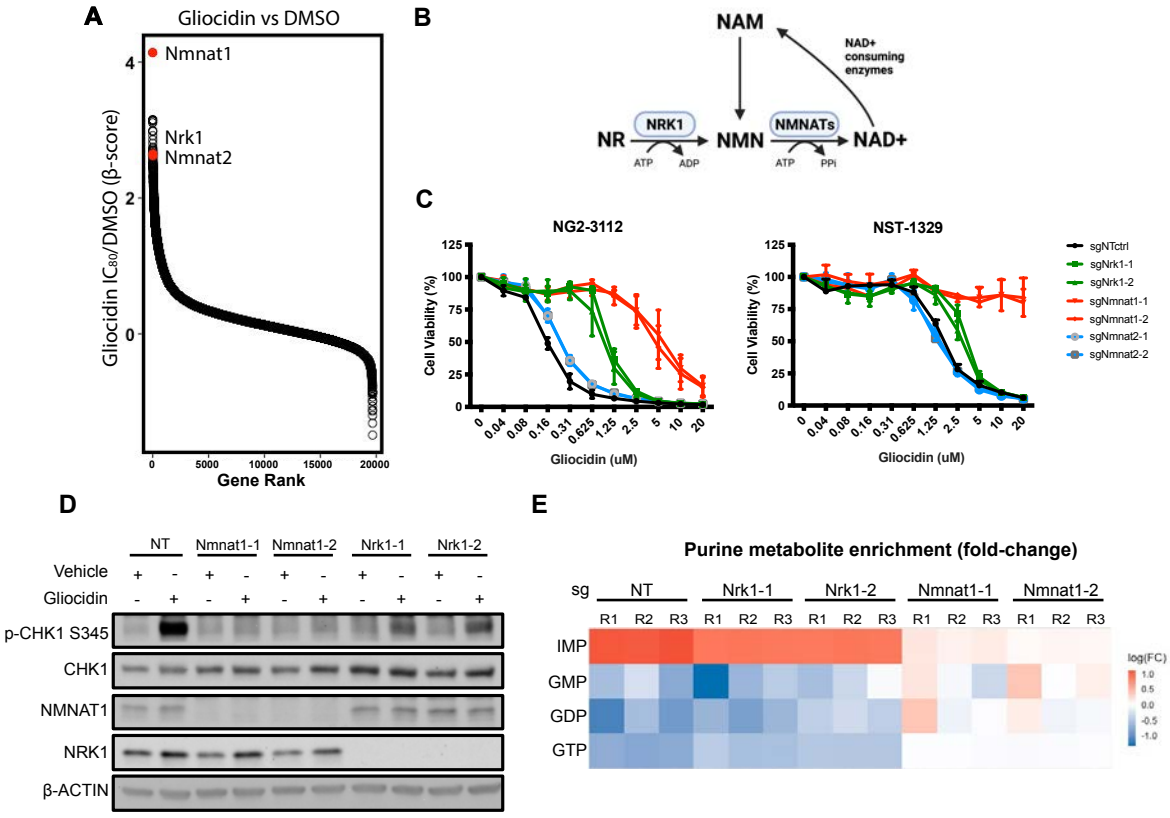


**Figure 3.4. Nmnat1 expression is required for Gliocidin cytotoxicity.** (A) Gliocidin gene dependency rank-order plot showing enriched and depleted sgRNAs from $IC_{80}$ Gliocidin versus vehicle CRISPR-Cas9 screen. (B) Diagram of $NAD^+$ salvage pathway. (C) Gliocidin dose response curves of non-targeting (NT), *Nrk1*, *Nmnat1* and *Nmnat2* knockout NG2-3112 and NST-1329 cells. (D) Western blot of NT, *Nrk1* and *Nmnat1* KO NG2-3112 treated with 1μM Gliocidin for 6 hours blotted for NMNAT1, NRK1 and p-CHK1. (E) Heatmap of purine metabolite level fold changes in 6 hours Gliocidin treated NT, *Nrk1* and *Nmnat1* KO NG2-3112 cells, measured by LC-

peptide. We extended these *Nmnat1* shRNA knockdown studies to orthotopic GBM PDX-160329-1 derived cells and observed similar Gliocidin resistance (Supplementary Figure 3.5A-B). We therefore conclude that NMNAT1 plays the dominant role in determining Gliocidin activity in the context of these two primary mouse GBM cells and focus on *Nmnat1* for the remainder of this study.

Knockout of *Nmnat1* and *Nrk1* attenuated Gliocidin-induced replication stress as shown by decreased p-Chk1 activation (Figure 3.4D). We further compared the

purine metabolite changes in *Nrk1* and *Nmnat1* KO cells to control cells. *Nrk1* and *Nmnat1* KO attenuated Gliocidin-induced IMP accumulation and guanine nucleotide depletion (Figure 3.4E) as measured by LC-MS/MS. Of note, the magnitude of replication stress and accumulated IMP attenuation is greater in *Nmnat1* than *Nrk1* knockout, which correlates with their degree of resistance to Gliocidin (Figure 3.4C). Thus, NMNAT1 activity is essential for the Gliocidin-induced cytotoxicity in tumor cells.

We also tested whether drug resistance induced by *Nmnat1* knockout is specific to Gliocidin or can be generalized to the additional IMPDH inhibitors, MPA and Mizoribine. $NAD^+$ salvage enzyme knockouts did not confer drug resistance to MPA or Mizoribine (Supplemental Figure 3.5C and 3.5D). Thus, the observed $NAD^+$ salvage enzyme dependence is specific to Gliocidin, and indicates a unique MoA compared to direct IMPDH inhibitors.

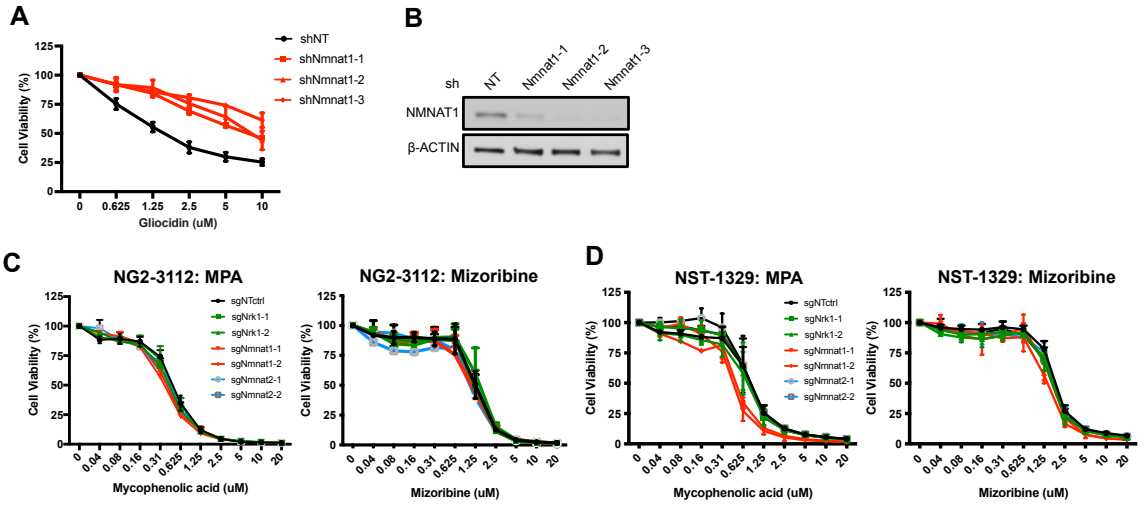


**Supplemental Figure 3.5.** (A) Gliocidin dose response curve of *Nmnat1* knockdown PDX-160329-1 cells (n=3). (B) Western blot validation of *Nmnat1* knockout in PDX-160329-1 cells in (A). (C and D) Dose response curve of (C) NG2-3112 or (D) NST-1329 cells treated with MPA or Mizoribine.

**Gliocidin is a prodrug requiring NAD salvage enzymes for metabolic activation**

Our preceding data fit into a model whereby Gliocidin may co-opt the $NAD^+$ salvage pathway enzymes, NRK1 and NMNAT1 (Supplemental Figure 3.6A), for conversion to its metabolically active form (Bieganowski & Brenner, 2004; Cooney et al., 1983). We hypothesized that by analogy to the synthesis of $NAD^+$ from nicotinamide riboside (NR), Gliocidin metabolic activation was initiated by Gliocidin ribosylation at the nitrogen of the pyridine ring to form Gliocidin-riboside (Gliocidin-R; Figure 3.5A). This step would be followed by NRK1-mediated phosphorylation to form Gliocidin-mononucleotide (Gliocidin-MN), with the final transfer of the adenylyl moiety by NMNAT1 to generate the final bioactive form, Gliocidin-adenine dinucleotide (Gliocidin-AD; Figure 3.5A). This model is in line with our *Nmnat1* and *Nrk1* knock out validation studies (Figure 3.4C), and further, because NMNAT1 depletion generates stronger resistance to Gliocidin than NRK1, all points to NMNAT1 as the likely rate limiting step of the activation pathway.

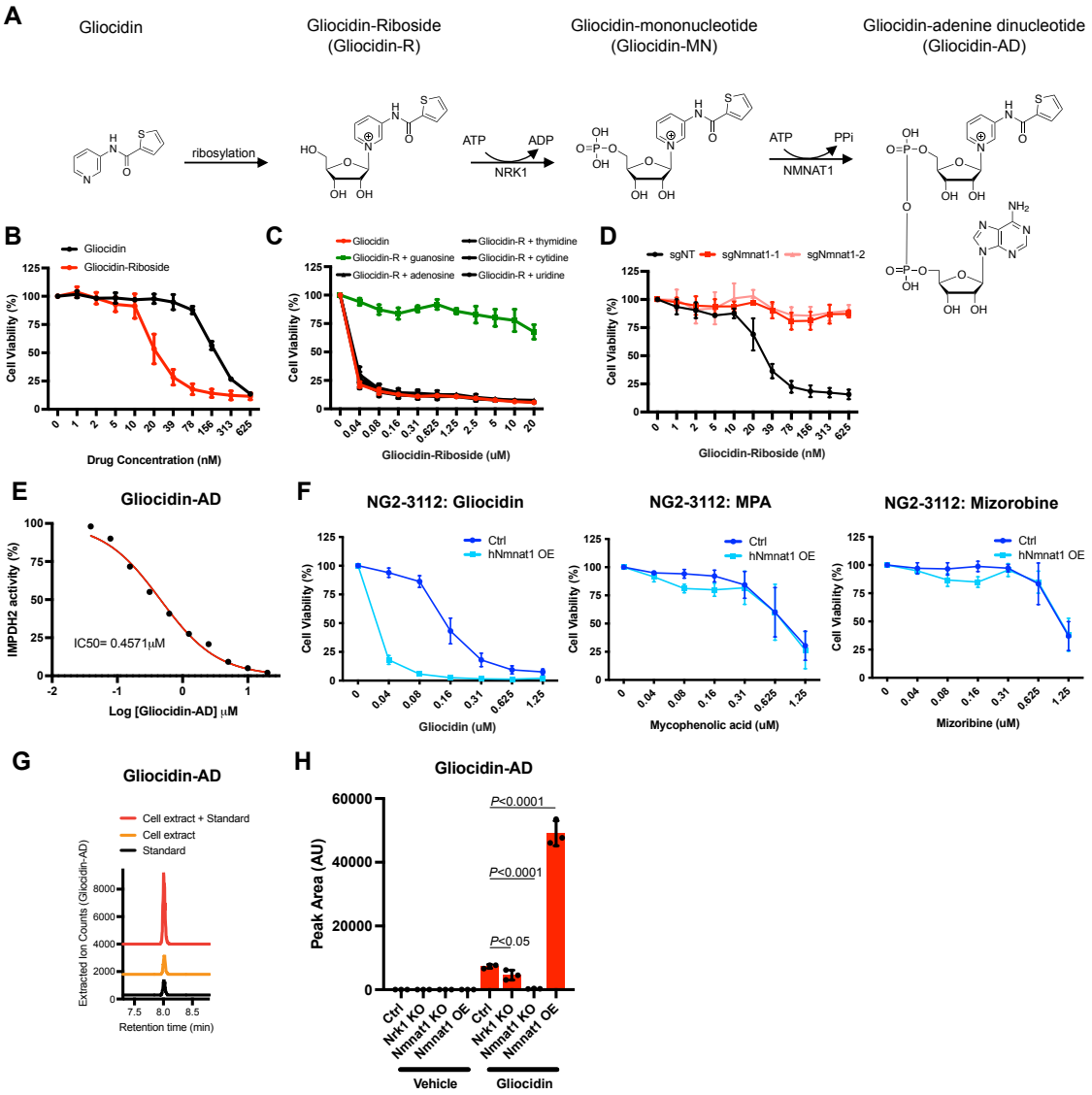


**Figure 3.5. Gliocidin is a prodrug that utilizes NAD salvage enzymes for drug activation.** (A) Diagram of proposed Gliocidin drug metabolism pathway. (B) Dose response curves of NG2-3112 cells treated with Gliocidin and Gliocidin-Riboside (n=3). (C) Dose response curves of NG2-3112 cells treated with Gliocidin-R co-supplemented with ribonucleosides (n=3). (D) Gliocidin-R dose response curves of non-targeting control (NT) or *Nmnat1* KO NG2-3112 cells (n=3). (E) IMPDH2 enzymatic activity assay of Gliocidin-AD. (F) Dose response curve of vector control and human Nmnat1 cDNA overexpressed NG2-3112 cells treated with Gliocidin, MPA or Mizoribine. (G) Extracted ion chromatograms of Gliocidin-AD (m/z=746.1041) in NG2-3112 cells treated with Gliocidin in comparison with synthetic standard. (H) Quantification of Gliocidin-Adenine dinucleotide levels in NG2-3112 control, *Nrk1* KO, *Nmnat1* KO and h*Nmnat1* OE cells by LC-MS/MS. Cells were treated with vehicle or Gliocidin for 10 hours. Data indicate mean ± SD (n=3, technical replicates). Two-tailed *p*-values were determined by unpaired student's *t* test.

To directly test the prodrug activation model, we synthesized all three proposed Gliocidin derivatives: Gliocidin-riboside, Gliocidin-mononucleotide, and Gliocidin-adenine dinucleotide (-R, -MN and -AD: Supplemental Figure 3.6A and Methods). Administration of Gliocidin-R to primary GBM NG2-3112 cells demonstrated a 7.5-fold higher toxicity ($IC_{50}$ of 20nM) than Gliocidin ($IC_{50}$: 150nM; Figure 3.5B). In addition, Gliocidin-R induced cytotoxicity was also uniquely rescued by guanosine supplement (Figure 3.5C). Moreover, like Gliocidin, *Nmnat1* knockout also generates Gliocidin-R drug resistance (Figure 3.5D). Thus, Gliocidin-R maintains the same MoA as Gliocidin and supports our model that Gliocidin-R is a first intermediate of the prodrug activation pathway. A further prediction of this model would be that the proposed mature form of the prodrug, Gliocidin-AD, should directly inhibit IMPDH2 activity. *In vitro* IMPDH enzyme assays confirmed the inhibitory properties of Gliocidin-AD (Figure 3.5E).

If as proposed, NMNAT1 activity is indeed the rate-limiting step required for synthesis of metabolically active Gliocidin-AD, we reasoned that elevating *Nmnat1* expression should increase Gliocidin-AD levels, and therefore commensurately increase its anti-tumor activity. As human and murine NMNAT1 proteins share high amino acid similarity (91.0%), we overexpressed human *Nmnat1* cDNA in murine GBM cells and assayed for Gliocidin activity. Overexpression of h*Nmnat1* shifted the $IC_{50}$ five-fold from 160nm to ~35nm, while the sensitivity to MPA or Mizoribine remained unchanged (Figure 3.5F). This hypersensitivity phenotype was also observed in PDX GBM cells overexpressing h*Nmnat1* (Supplemental Figure 3.6C

and 3.6D). Moreover, as expected, h*Nmnat1* overexpression in PDX GBM cells also hypersensitized cells to Gliocidin-R (Supplemental Figure 3.6E and 3.6F). Taken together, these data are consistent with our model where Gliocidin-R modification proceeds to NRK/NMNAT1 mediated production of Gliocidin-AD whose activity can be potentiated by enhancing *Nmnat1* activity.

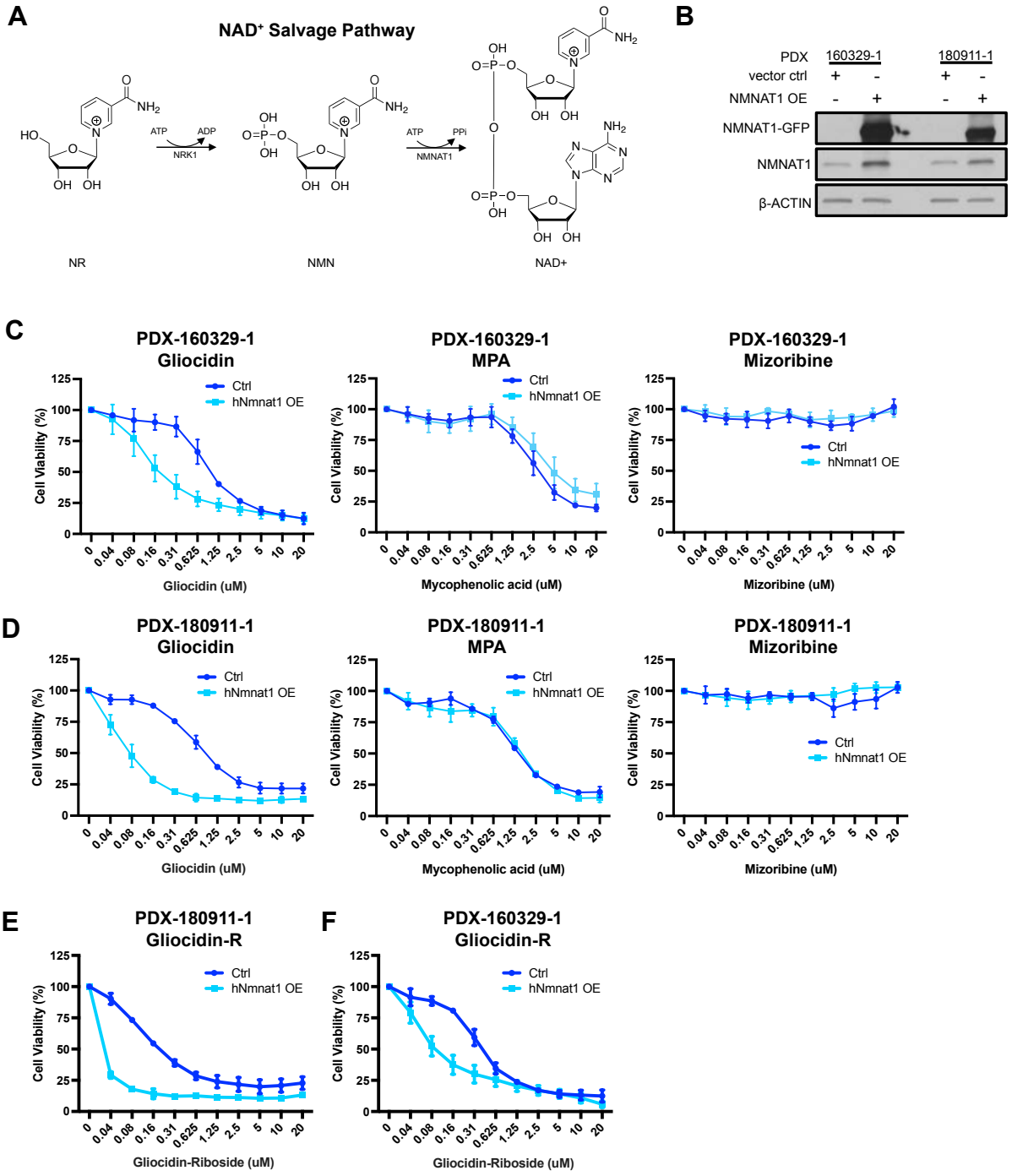


**Supplemental Figure 3.6.** (A) Schematic of NAD$^+$ salvage pathway. (B) Western blot validating human NMNAT1 overexpression in GBM PDX cells. (C and D) Dose response curves of (C) PDX-160329-1 and (D) PDX-180911-1 cells treated with Gliocidin, MPA or Mizoribine (n=3). (E and F) Gliocidin-Riboside dose response curves of vector control or human *Nmnat1* cDNA overexpressed (E) PDX-160329-1 and (F) PDX-180911-1 cells (n=3). NR: nicotinamide riboside; NMN: nicotinamide mononucleotide; NAD: nicotinamide adenine dinucleotide.

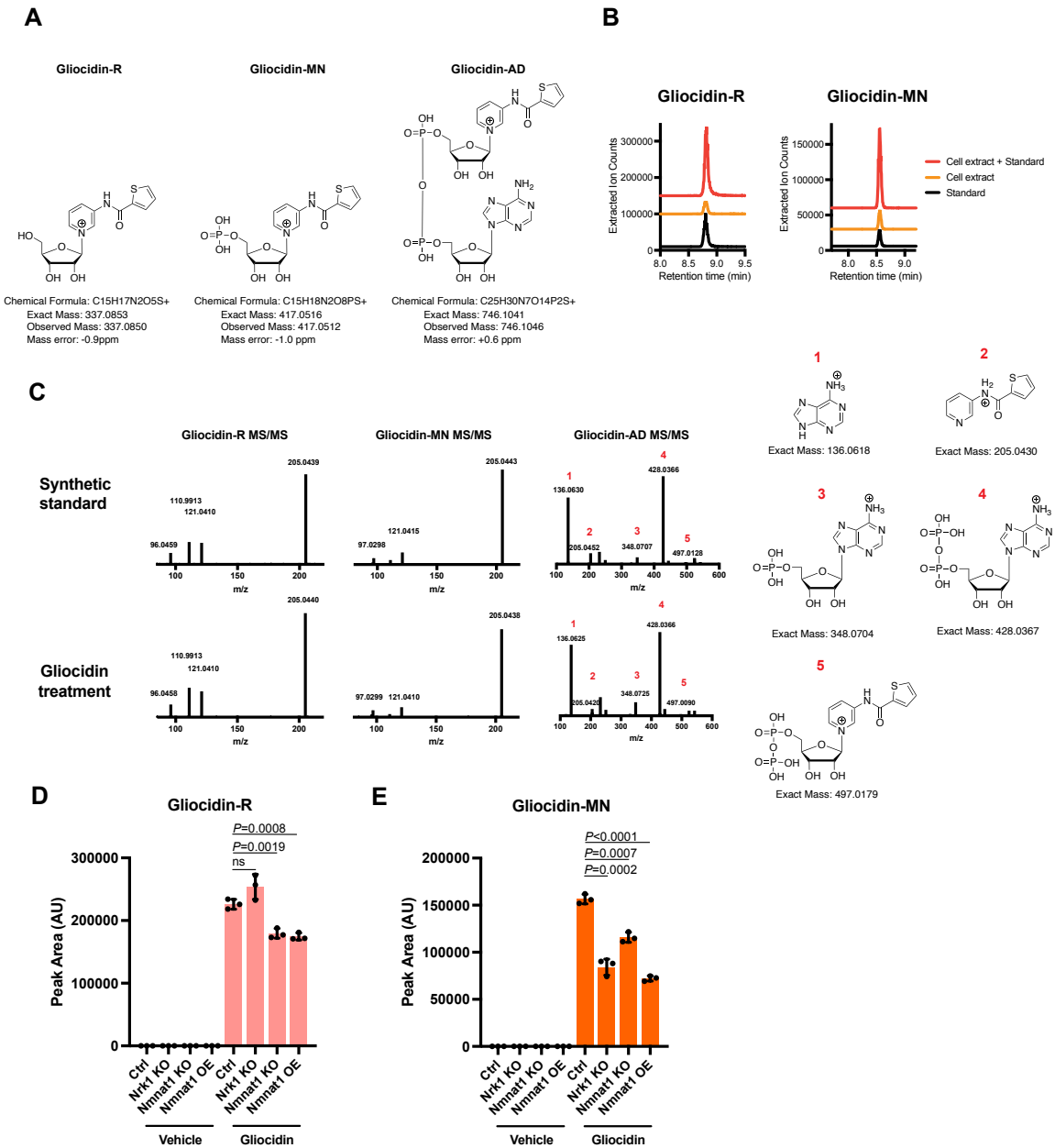
A
Gliocidin-R
Gliocidin-MN
Gliocidin-AD
Chemical Formula: C15H17N2O5S+
Exact Mass: 337.0853
Observed Mass: 337.0850
Mass error: -0.9ppm
Chemical Formula: C15H18N2O8PS+
Exact Mass: 417.0516
Observed Mass: 417.0512
Mass error: -1.0 ppm
Chemical Formula: C25H30N7O14P2S+
Exact Mass: 746.1041
Observed Mass: 746.1046
Mass error: +0.6 ppm
B
Gliocidin-R
Gliocidin-MN
Extracted Ion Counts
Retention time (min)
Cell extract + Standard
Cell extract
Standard
C
Gliocidin-R MS/MS
Gliocidin-MN MS/MS
Gliocidin-AD MS/MS
Synthetic standard
Gliocidin treatment
m/z
Exact Mass: 136.0618
Exact Mass: 205.0430
Exact Mass: 348.0704
Exact Mass: 428.0367
Exact Mass: 497.0179
D
Gliocidin-R
P=0.0008
P=0.0019
ns
Peak Area (AU)
Ctrl
Nrk1 KO
Nmnat1 KO
Nmnat1 OE
Vehicle
Gliocidin
E
Gliocidin-MN
P<0.0001
P=0.0007
P=0.0002

**Supplemental Figure 3.7.** (A) Chemical structures of Gliocidin-R, -MN and -AD synthetic standards used for LC-MS. Observed mass is m/z found in NG2-3112 cells treated with Gliocidin. (B) Extracted ion chromatograms of Gliocidin-R (m/z=337.0853) and Gliocidin-MN (m/z=417.0516) in NG2-3112 cells treated with Gliocidin in comparison with synthetic standard. (C) Comparison of MS/MS fragmentation spectra of Gliocidin-R, -MN and -AD between Gliocidin treated NG2 cells to synthetic standard. In Gliocidin-AD spectrum, numbers highlighted in red are characteristic ions, assigned as 1: adenine, 2: Gliocidin, 3: AMP, 4: ADP, 5: Gliocidin-diphosphate ions. (D) Quantification of Gliocidin-R and -MN levels in NG2-3112 control, *Nrk1* KO, *Nmnat1* KO and h*Nmnat1* OE cells by LC-MS/MS. Cells were treated with vehicle or 2.5μM Gliocidin for 10 hours. Data indicate mean ± SD, n=3. Two-tailed *p*-values were determined by unpaired student's

To evaluate if Gliocidin is intracellularly converted to Gliocidin-AD through its various proposed intermediates, we performed LC-MS/MS to detect the presence of Gliocidin derivatives using the synthetic standards (-R, -MN and -AD; Supplemental Figure 3.7A) as controls. Control, *Nrk1* KO, *Nmnat1* KO and h*Nmnat1* OE NG2-3112 cells exhibited the presence of all Gliocidin derivatives (-R, -MN and -AD) in Gliocidin treated, but not vehicle-treated, cells (Figure 3.5G and Supplemental Figure 3.7A-E). All structures were validated by exact mass, retention time, and MS/MS matching (Supplemental Figure 6A-C). Of note, adenine and Gliocidin ions were found in Gliocidin-AD MS/MS, which further supports the conjugation of adenine dinucleotide to Gliocidin. As predicted, a significantly higher amount of Gliocidin-AD was detected in h*Nmnat1* OE cells than in the control cells (7-fold increase; Figure 3.5H), while Gliocidin-AD was nearly undetectable in *Nmnat1* KO cells. *Nrk1* KO cells also exhibited reduced Gliocidin-AD compared to control cells, which is commensurate with its intermediate Gliocidin resistance. In aggregate, we demonstrate that within tumor cells, the

prodrug Gliocidin is converted to its predicted derivatives and that NMNAT1 is the rate determining enzyme for Gliocidin-AD production.

**The GID E3 ligase complex regulates NMNAT1 degradation in mouse GBM cells**

A further result from the genome wide CRISPR screen, was the observed depletion of GID complex structural proteins (Figure 3.2B and Supplemental Figure 3.2D). The GID complex is an evolutionarily conserved supramolecular multiprotein E3 ligase complex originally discovered in yeast to degrade gluconeogenic enzymes under glucose-sufficient growth conditions (Regelmann et al., 2003). Its core component consists of two RING-like subunits (Maea and Rmnd5a) and five scaffold subunits (Wdr26, Gid8, Ranbp9, Armc8 and Ypel5; Supplemental Figure 3.8A). Ube2h is its upstream E2 conjugating enzyme (Lampert et al., 2018; Schule et al., 2000).

Our CRISPR data showed depletion of sgRNAs for Wdr26, Ube2h, Gid8, Maea, Armc8 and Rmnd5a, but conversely, only one GID component sgRNA, Ypel5, appeared as one of the top enriched hits (Supplemental Figure 3.8B). Wdr26 is an essential component of the GID complex, whose absence causes disintegration (Sherpa et al., 2021). Knocking out of *Wdr26* (as a representative gene of the absent GID complex sgRNAs) in NG2-3112 and NST-1329 tumor cells increased Gliocidin sensitivity. In contrast, *Ypel5* KO cells developed resistance to Gliocidin (Supplemental Figure 3.8C-D). Knockout of *Wdr26* or *Ypel5* in both lines did not affect tumor cell sensitivity to the known IMPDH2 inhibitors MPA or Mizoribine

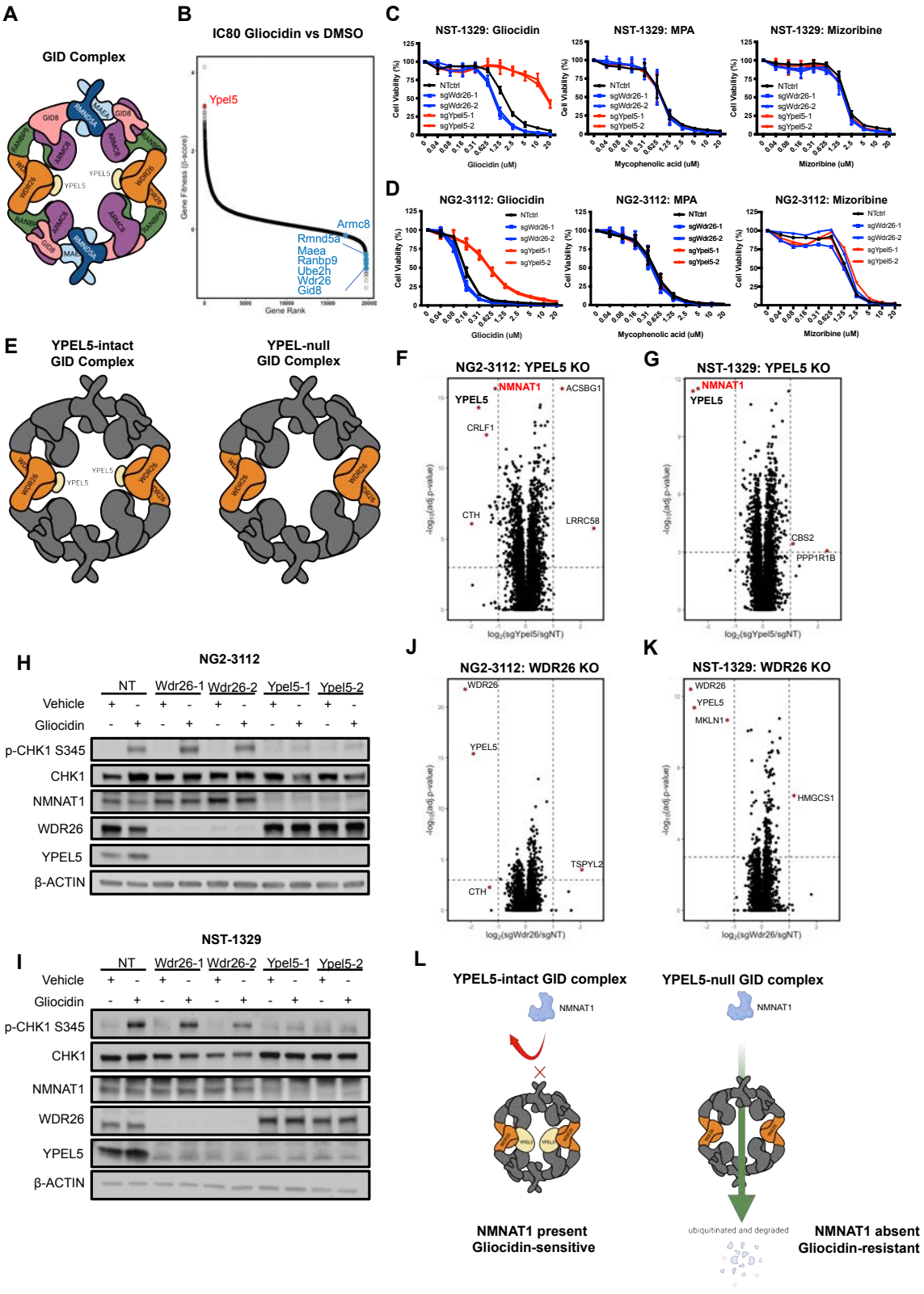
A
GID Complex
B
IC80 Gliocidin vs DMSO
Ypel5
Armc8
Rmnd5a
Maea
Ranbp9
Ube2h
Wdr26
Gid8
Gene Fitness (β-score)
Gene Rank
C
NST-1329: Gliocidin
NST-1329: MPA
NST-1329: Mizoribine
Cell Viability (%)
NTctrl
sgWdr26-1
sgWdr26-2
sgYpel5-1
sgYpel5-2
Gliocidin (uM)
Mycophenolic acid (uM)
Mizoribine (uM)
D
NG2-3112: Gliocidin
NG2-3112: MPA
NG2-3112: Mizoribine
E
YPEL5-intact GID Complex
YPEL-null GID Complex
F
NG2-3112: YPEL5 KO
NMNAT1
ACSBG1
YPEL5
CRLF1
CTH
LRRC58
G
NST-1329: YPEL5 KO
CBS2
PPP1R1B
H
NG2-3112
NT
Wdr26-1
Wdr26-2
Ypel5-1
Ypel5-2
Vehicle
Gliocidin
p-CHK1 S345
CHK1
NMNAT1
WDR26
YPEL5
β-ACTIN
I
NST-1329
J
NG2-3112: WDR26 KO
TSPYL2
K
NST-1329: WDR26 KO
WDR26
MKLN1
HMGCS1
L
YPEL5-intact GID complex
YPEL5-null GID complex
NMNAT1 present
Gliocidin-sensitive
ubiquitinated and degraded
NMNAT1 absent
Gliocidin-resistant

**Supplemental Figure 3.8.** (A) Cartoon diagram of the GID complex. (B) Gliocidin gene dependency rank-order plot showing enriched and depleted sgRNAs from genome wide CRISPR-Cas9 KO screen treated with $IC_{80}$ Gliocidin over vehicle. (C and D) Dose response curves of non-targeting (NT), *Wdr26* and *Ypel5* knockout in (C) NG2-3112 and (D) NST-1329 cells treated with Gliocidin, MPA or Mizoribine. (E) Diagram model of YPEL5-intact and YPEL5-null GID complex. (F and G) Volcano plot of quantitative multiplexed proteomics data showing enriched and depleted peptides in *Ypel5* KO over control (F) NG2-3112 and (G) NST-1329 cells. (H and I) Western blot of NT, *Wdr26* and *Ypel5* KO (H) NG2-3112 and (I) NST-1329 cells treated with 6 hr of 0.5μM Gliocidin blotted for replications stress activity marker and GID complex proteins. (J and K) Volcano plot of quantitative multiplexed proteomics data showing enriched and depleted peptides in *Wdr26* KO over control (J) NG2-3112 and (K) NST-1329 cells. (L) Schematic of the proposed mechanism of YPEL5-GID complex mediated NMNAT1 degradation.

(Supplemental Figure 3.8C-D). Taken together, GID complex gene KOs specifically affect Gliocidin sensitivity, but not sensitivity to other IMPDH inhibitors. This implies that the GID complex is affecting Gliocidin activity not by perturbing IMPDH inhibition, but instead through a unique mechanistic feature of Gliocidin.

Although the structural details of the GID complex have been elegantly resolved, the functional role of YPEL5 in this complex is still unclear (Sherpa et al., 2021). Unlike WDR26, an essential component of the GID complex, YPEL5 is non-essential for the integrity or E3 ligase activity of the complex (Lampert et al., 2018). That removal of *Ypel5* in our GBM cells resulted in resistance to Gliocidin while complex disassembly by removal of structural components conferred sensitivity, invokes a regulatory role for *Ypel5*. We therefore hypothesized that YPEL5 functions as a negative regulator of the GID complex, and that the absence of YPEL5 removes blockade of GID complex dependent degradation of an essential protein for Gliocidin activity. To identify candidate protein GID complex substrates,

we performed quantitative multiplex proteomics on non-targeting (NT) control, *Ypel5* KO and *Wdr26* KO NG2-3112 and NST-1329 GBM cells. Comparison of the proteome between *Ypel5* KO and NT control showed that aside from YPEL5, NMNAT1 is one of the most depleted proteins in NG2-3112 cells (Supplemental Figure 3.8F) and the only significantly depleted protein in NST-1329 cells (Supplemental Figure 3.8G). Western blot confirmed that *Ypel5* KO depletes NMNAT1 protein expression and attenuates Gliocidin-induced p-CHK1 activation, which is consistent with the Gliocidin resistant phenotype (Supplemental Figure 3.8H-I).

It is important to note here that knockout of *Wdr26* also induces YPEL5 expression loss. The exact mechanistic regulation is currently unknown, but we postulate as WDR26 and YPEL5 are direct interactor, the presence of WDR26 is necessary for the stability of YPEL5. This co-downregulation of YPEL5 in WDR26 KO cells may seem contradictory, however, it is important to note the the loss of WDR26 disintegrates the GID complex. As NMNAT1 is a substrate of the GID complex, the loss of the GID complex (in this case, induced by *Wdr26* KO) will prevent NMNAT1 from being degraded. In this context of an absent GID complex, the presence or absence of YPEL5 is not important for NMNAT1 regulation.

Taken together, these data independently confirm our earlier finding that NMNAT1 is required for Gliocidin activation and provide genetic evidence that in the absence of the GID complex negative regulator, YPEL5, NMNAT1 degradation is accelerated resulting in blockade of maturation of Gliocidin-MN into Gliocidin-AD (Figure 3.5H). Taken together, our results identify NMNAT1 as a substrate of

the GID complex and identify YPEL5 is a negative regulator of the GID complex for NMNAT1 degradation (Supplemental Figure 3.8L). Thus, Gliocidin therapy is enhanced by disruption of GID E3 ligase activity.

**Gliocidin crosses the BBB and targets GBM *in vivo***

We next evaluated Gliocidin anti-tumor activity *in vivo*. First, *in vivo* tolerability was examined by administering vehicle or Gliocidin (50 mg/kg, twice per day, I.P.) to C57BL/6J mice for 28 days. Consistent with our previous studies, no body weight change or notable behavioral abnormalities were observed (Supplemental Figure 3.9A) (Chau et al., 2014). In addition, complete blood count panel studies of Gliocidin treated mice were normal (Supplemental Figure 3.9B). Next, we evaluated the anti-tumor effect of Gliocidin in subcutaneous tumor mouse models. MRI imaging showed that 10-12 days of Gliocidin administration (50 mg/kg, twice per day, I.P.) effectively reduced tumor progression of mouse glioma cell subcutaneous tumors (NST-1329; Supplemental Figure 3.9C) relative to vehicle.

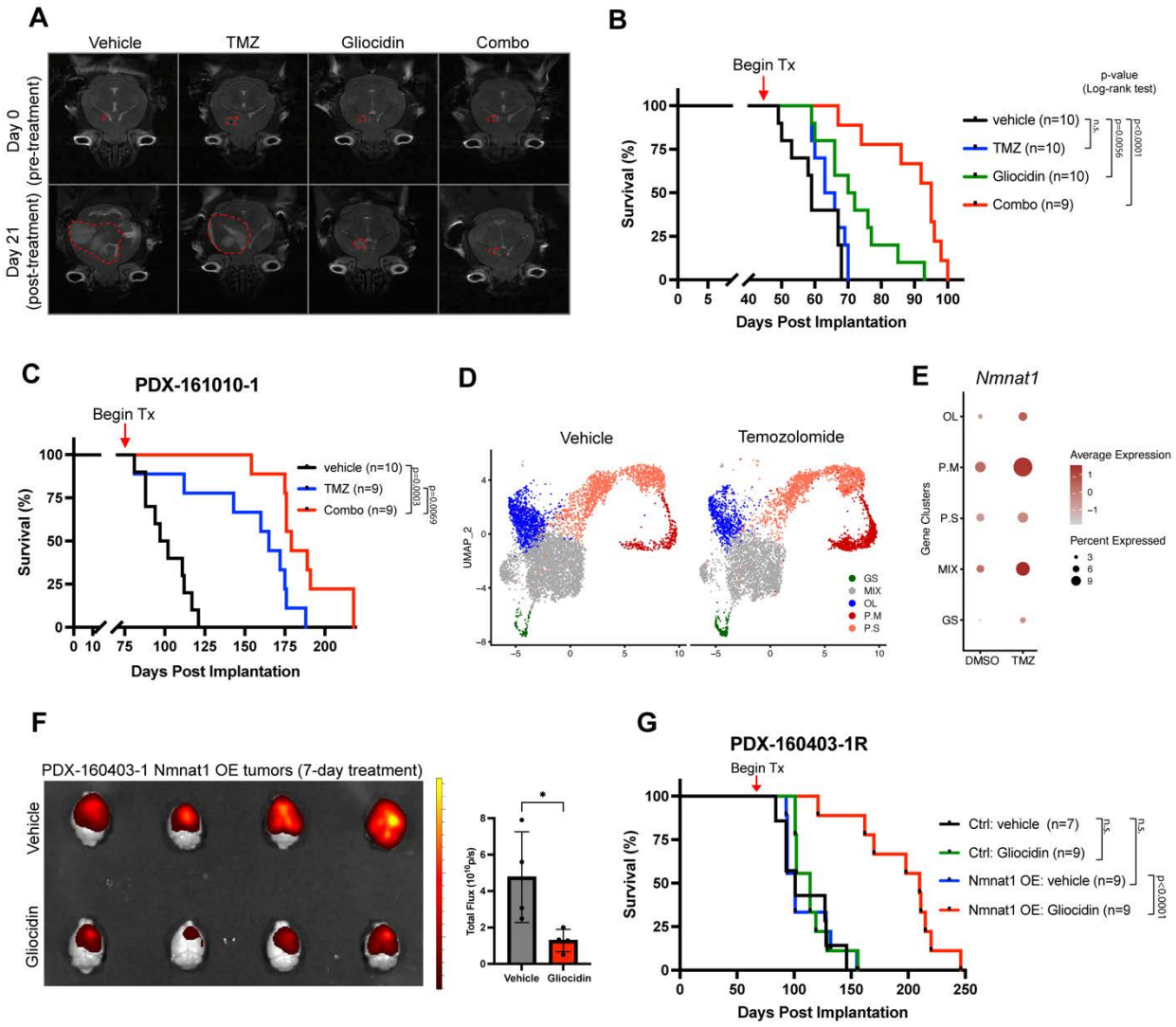


**Figure 3.6. Gliocidin prolongs survival of orthotopic GBM mice.** (A) T2-weighted Brain MRI of mice performed at day 0 (pretreatment) and day 21 (21 days of treatment). Tumor regions are highlighted in red dashed lines. (B) Kaplan-Meier curves of NST-1329 orthotopic GBM mice (C57BL/6) administered with vehicle, TMZ, Gliocidin or combination of Gliocidin and TMZ. *P* values were calculated with Log-rank test. (C) Kaplan-Meier curves of PDX-161010-1 orthotopic GBM mice treated with vehicle, TMZ or combo (TMZ + Gliocidin). *P* values were calculated with Log-rank test. (D) Merged single cell sequencing data of PDX-180911-1 tumors treated with vehicle (n=3 independent tumors) or Temozolomide (n=3 independent tumors) depicted in UMAP. Cell clusters annotation: GS (green): Glioma-stem cell, Mix (gray): undefined mixed population, PS (red): proliferation S-phase, PM (orange): proliferation M-phase, OL (blue): oligodendrocytic lineage, NPC (purple): neural progenitors. (E) Dot plot of single cells from panel (D) showing *Nmnat1* expression across cell clusters and treatment conditions. (F) *Ex vivo* GFP Fluorescent imaging of dissected brain from PDX-160403-1-R tumor mice treated with vehicle (n=4) or Gliocidin (n=4, 50mg/kg/day, I.P., two doses per day) for 7 days. Bar plot data indicate mean ± SD. Total flux is quantified. *p<0.05. Two tailed *p* value determined by Mann-Whitney test. (G) Survival analysis of vector-control and *Nmnat1* OE 160403-1-R orthotopic GBM mice treated with vehicle or Gliocidin (50 mg/kg, I.P., two doses per day). P-values were calculated with Log-rank test.

Since we envisage Gliocidin for treatment of GBM and potentially other intracranial tumors, we performed pharmacokinetics (PK) studies on Gliocidin-treated versus vehicle-treated mice to evaluate its blood-brain-barrier (BBB) penetrating capability. The results showed that the brain to plasma ratio of Gliocidin is 4:1 (Supplemental Figure 3.9D), demonstrating effective BBB penetrability and the potential for Gliocidin to reach GBM.

The DNA alkylating agent, Temozolomide (TMZ), is the current chemotherapeutic standard of therapy for GBM. We therefore evaluated the efficacy of Gliocidin alone and in combination with TMZ in orthotopic murine GBM mice. Immunocompetent orthotopic GBM mice were generated by implanting NST-1329 cells into the striatum of C57BL/6 mice. For survival studies, mice were administered with vehicle (Veh), Gliocidin (50mg/kg, twice daily for one month), TMZ (50 mg/kg, total two doses) or a combination of Gliocidin and TMZ (Combo; 50mg/kg Gliocidin twice daily for one month and two doses of 50mg/kg TMZ). We monitored tumor burden evolution by performing brain magnetic resonance imaging (MRI) before and 21 days after treatment. While tumor size progressed rapidly in vehicle and TMZ-treated mice, minimal changes in tumor size were noted in the Gliocidin and Combo-treated group (Figure 3.6A). Gliocidin monotherapy prolonged survival relative to vehicle-treated mice, while TMZ alone prolonged survival mildly. However, the combination of Gliocidin plus TMZ greatly prolonged survival over Gliocidin alone (Figure 3.6B; median survival of Veh, TMZ, Gliocidin and Combo: 59, 64.5, 71 and 95 days; Log-rank test, Veh vs Gliocidin: $p = 0.0056$, Veh vs TMZ: $p = 0.1267$, TMZ vs Gliocidin: $p = 0.0225$, Veh vs Combo: $p < 0.0001$).

As the GBM tumor microenvironment is thought to be immunosuppressive, we further evaluated whether the absence of an intact immune system affects the anti-tumor effect of Gliocidin in GBM mouse models. We generated orthotopically implanted NST-1329 cells in athymic nude mice and administered vehicle or Gliocidin (50mg/kg, twice per day, IP) beginning at 45 days post implantation. Like immunocompetent mice, Gliocidin treatment inhibited intracranial tumor growth (Supplemental Figure 3.9E) and prolonged survival (Supplemental Figure 3.9F; median survival of Veh: 64 days, Gliocidin: 80.5 days; Log-rank test) relative to vehicle-treated mice. Thus, it appears that the absence of T-cells had minimal effect in the therapeutic efficacy of Gliocidin.

A

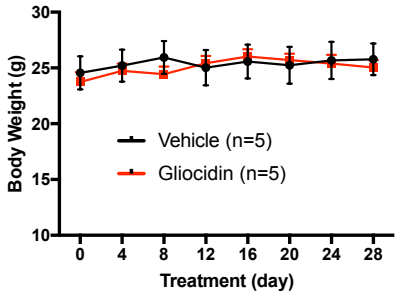


B

| | Vehicle (n=4) | Gliocidin (n=4) | *P*-value | Reference Range | Units |
|---|---|---|---|---|---|
| Hemoglobin | 14.48 | 14.05 | 0.9714 | 10.80 - 19.20 | g/dL |
| WBC | 8.45 | 8.8 | 0.8857 | 3.90 - 13.96 | x1000/uL |
| Platelets | 876.5 | 885.25 | 0.8857 | 565.00 - 2159.00 | x1000/uL |
| Neutrophil | 9.99 | 17.85 | 0.4857 | 7.36 - 28.59 | % |
| Lymphocyte | 83.73 | 77.83 | >0.9999 | 61.26 - 87.12 | % |

C

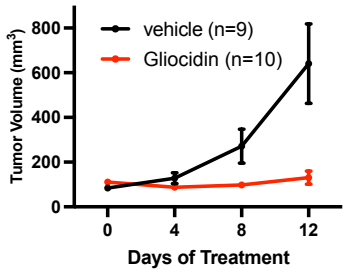


D

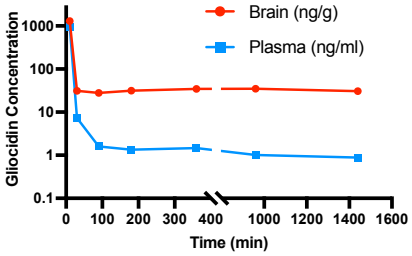


E

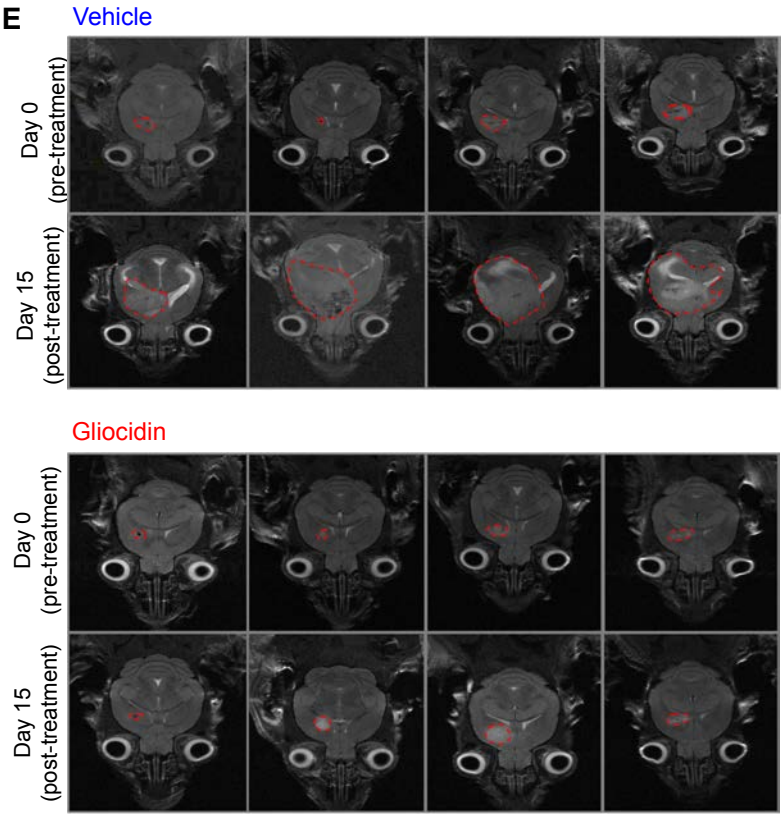


F

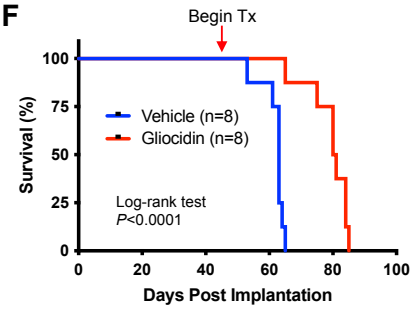


G

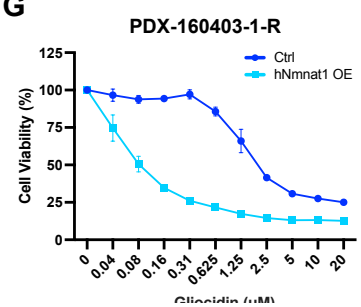


H

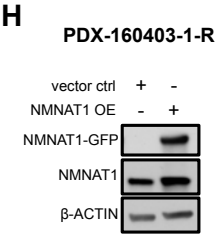

**Supplemental Figure 3.9.** (A) Body weight measurement of wildtype C57BL/6 administered with vehicle or Gliocidin (50 mg/kg, I.P., two doses per day). (B) Hemogram data of wildtype C57BL/6 administered with vehicle or Gliocidin (50 mg/kg, I.P., two doses per day) over 10 days. Statistics performed by Mann-Whitney test. (C) Tumor volume measurement of NST-1329 subcutaneous tumor mice administered with Gliocidin (50 mg/kg, I.P., two doses per day) or vehicle for 10-12 days. Tumors were implanted at the flank of athymic nude mice. (D) Pharmacokinetic study of mice injected with Gliocidin (10 mg/kg I.P.) and quantified in plasma or brain over time. (E) T2-weighted brain MRI were performed on vehicle and Gliocidin-treated athymic nude mice at day 0 and day 15 of treatment. Tumor regions are highlighted in red dashed lines. (F) Kaplan-Meier curves of NST-1329 orthotopic GBM mice (athymic nude) administered with vehicle or Gliocidin (50 mg/kg, I.P., two doses per day). *P*-value were calculated with Log-rank test. (G) Gliocidin dose-response curve of vector-control and Nmnat1 OE 160403-1-R. (H) Western blot validating human *Nmnat1* cDNA overexpression in GBM PDX-160403-1-R cells.

Finally, we evaluated the effect of Gliocidin together with Temozolomide in orthotopic GBM PDX mice. We treated GBM PDX mice with vehicle, TMZ alone, or a combination of Gliocidin and TMZ. TMZ alone significantly prolonged survival (Figure 6C; median survival: vehicle=99.5 days, TMZ=165 days, $p$=0.0003, Log-rank test). However, addition of Gliocidin further prolonged survival (Figure 6C; median survival: Combo=179 days; TMZ vs Combo: $p$=0.0069, Log-rank test).

To understand the mechanism behind the additional benefit of Gliocidin over TMZ alone, we treated orthotopic GBM mice with vehicle or TMZ and harvested the tumors for single cell sequencing. Transcriptional cell clusters were defined by previously described gene signatures (Figure 6D) (Xie et al., 2022). As *Nmnat1* expression levels determine the amount of Gliocidin-AD, we probed for *Nmnat1* expression levels between TMZ and vehicle treated tumors. Analysis showed that Temzolomide treatment increases *Nmnat1* expression in most GBM transcriptional cell clusters (Figure 6E). The relatively low per-cell depth of transcript sequencing results in a low estimate of the absolute number of cells having upregulation in a

given cluster (Haque et al., 2017). We reasoned that the increase in survival of the combination group is attributed to Temozolomide induced upregulation of *Nmnat1* in tumor cells.

### *In vivo* Gliocidin tumor sensitivity is modulated by *Nmnat1* expression

To further probe the role and degree of influence of *Nmnat1* expression in sensitizing tumors to Gliocidin, we turned to a PDX (160403-1R) established from a recurrent GBM patient that is resistant to Gliocidin *in vitro* ($IC_{50}$=2μM). In culture, *Nmnat1* overexpression in 160403-1R tumor cells lowered its $IC_{50}$ by 25-fold (from 2μM to 80nM) (Supplemental Figure 8G-H). We generated orthotopic GBM PDX mice bearing either 160403-1R GFP control and *Nmnat1*-GFP overexpressing (OE) tumors and administered either vehicle or Gliocidin. For a short treatment period of 7 days, Gliocidin greatly reduced tumor burden as shown by a significant reduction in total GFP flux ($p$=0.0286, Mann-Whitney test; Figure 6F). Over time, control and *Nmnat1* OE mice treated with vehicle have no survival difference (median survival: Ctrl Veh=101 days, *Nmnat1* OE Veh: 101 days, $p$=0.6078, Log-rank test; Figure 6G). Gliocidin treatment of control mice also did not affect survival (median survival: Ctrl Veh=101 days, Ctrl Gliocidin: 114 days, $p$=0.5557, Log-rank test; Figure 6G). In contrast, Gliocidin strikingly prolonged the survival of *Nmnat1* OE mice by more than doubling their median survival from 100 days to 210 days (median survival: *Nmnat1* OE Veh=101 days, *Nmnat1* OE Gliocidin: 210 days, $p$<0.0001, Log-rank test; Figure 6G). This illustrates in proof of principle that elevating *Nmnat1* expression greatly sensitizes *in vivo* tumors to Gliocidin and

provides further rationale for Gliocidin to be administered in tumors with high *Nmnat1* expression.

**Gliocidin induces global metabolic alterations in tumor**

To gain insight into the *in vivo* anti-tumor mechanism of Gliocidin, we profiled tumor metabolite levels on NST-1329 intracranial tumors treated with vehicle or Gliocidin for 6 hours (to be comparable with the *in vitro* metabolomic study also done at 6hr). Based on the 81 metabolites measured, 56 metabolites had significant changes (Supplemental Figure 3.10A). PCA analysis based on these 81 metabolites separated DMSO and Gliocidin-treated tumors into two distinct clusters (Supplemental Figure 3.10B), demonstrating a significant change in tumor metabolism. Western blot analysis of these tumors showed p-Chk1 activation, indicative of Gliocidin-induced replication stress (Supplemental Figure 3.10C). Further, *in vivo* Gliocidin reduced not only guanine nucleotide levels (Supplemental Figure 3.10D-G; although GTP reduction is not statistically significant), but also AMP and UMP levels (Supplemental Figure 3.10H and 3.10I, respectively). This additional reduction of nucleotides (AMP and UMP), as compared to only guanylate reduction *in vitro*, was also observed in other tumor types treated with IMPDH inhibitors MMF (Mycophenolate Mofetil, or CellCept) and Mizoribine as previously reported (Valvezan et al., 2020). The underlying mechanisms of this *in vivo* effect remain unclear, but many possible feedback mechanisms promoted by tumor microenvironment interactions could likely contribute. In aggregate, these data show the same Gliocidin activity *in vivo* tumors

as observed in primary cultured tumor cells but with additional effects specific to the *in vivo* context.

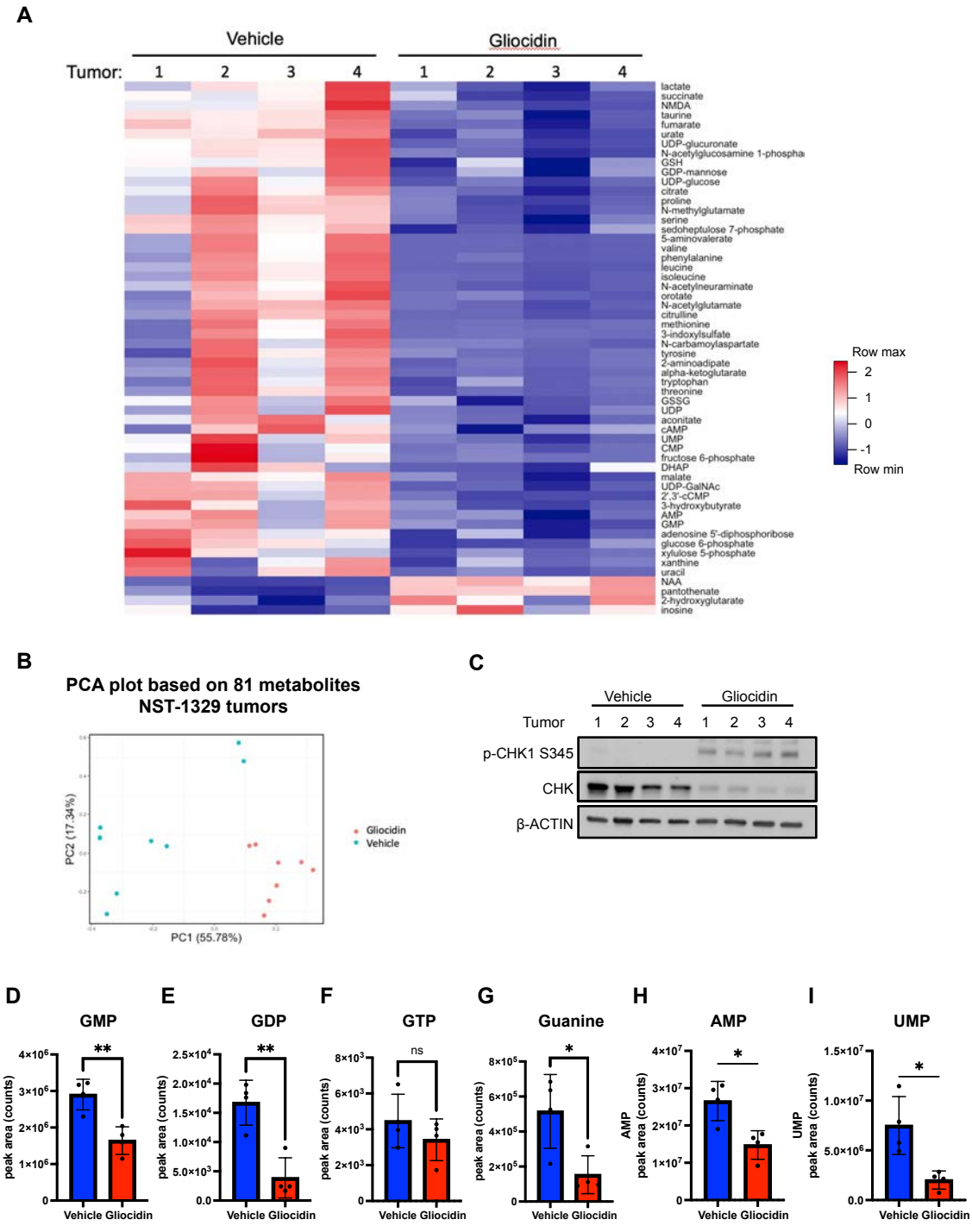

**Supplemental Figure 3.10.** (A) Heatmap of NST-1329 tumor tissues from orthotopic tumor mice that were administered with vehicle or Gliocidin for 6 hours. Heatmap rows showed the metabolites with levels that are significantly changed after Gliocidin treatment. (B) PCA plot of the metabolite profile of vehicle and Gliocidin-treated tumors (n=4 from each group, with two technical replicates). (C) Western blot of vehicle and Gliocidin-treated tumors for p-Chk1 activity. (D-I) Individual comparison of peak areas across different metabolites between vehicle and Gliocidin treated tumors.

## Discussion

### Targeting IMPDH2 as a GBM vulnerability

Although targeting *de novo* nucleotide synthesis in tumor has long been a major component within chemotherapeutic regimens in various solid tumors, its role as a brain tumor vulnerability has traditionally not been properly assessed due to the inaccessibility of conventional drugs into the brain. Recently, several studies have revealed the *de novo* pyrimidine synthesis pathway as a vulnerability and actionable target of non-GBM brain tumors (ie. IDH-mutant, DIPG and medulloblastoma) by inhibiting orthotopic tumor growth with BAY2402234, a brain penetrable drug that targets dihydroorotate dehydrogenase (DHODH) (Gwynne et al., 2022; Pal et al., 2022; Shi et al., 2022). GBM, on the other hand, is more complicated as it is dependent on both *de novo* purine and pyrimidine synthesis (Wang et al., 2019; X. Wang et al., 2017) and possess plasticity to interchange its nucleotide reliance between *de novo* and salvage pathways (Shi et al., 2022). In our study, we screened for chemical compounds that solely kill murine GBM cells but spares MEFs to enrich for anti-GBM specific compounds. By performing a genome-wide CRISPR knockout screen on Gliocid treated cells and forming a hypothesis of its MoA from results therein, we elucidated Gliocid as an IMPDH inhibitor that inhibits *de novo* guanine nucleotide synthesis. We further showed that both murine and human GBM cells are sensitive to Gliocid with $IC_{50}$ at a submicromolar level. This corroborates with known studies on IMPDH2 dependency of GBMs (Kofuji et al., 2019). Although IMPDH inhibitors have been extensively studied for their anti-tumor potential in various tumor types (Naffouje

et al., 2019), Valvezan and colleagues (Valvezan et al., 2020) have shown that among the clinically approved IMPDH inhibitors, only Mizoribine showed possible on-target activity (using AICAR accumulation as readout) in brain tissue while MPA performed poorly. Unfortunately, in the GBM patient-derived lines that we have tested, all were resistant to Mizoribine.

As mentioned, the finding that IMPDH2 is a vulnerability of GBM has previously been reported (Kofuji et al., 2019). Patient GBM express high levels of IMPDH2, the rate-limiting enzyme that commits the conversion of inosine monophosphate (IMP) to guanosine monophosphate (GMP) (Kofuji et al., 2019). Recent studies have reported that GBM derived cell lines can be dependent on de novo purine synthesis relative to its surrounding normal tissue or to non-tumor cells that utilize the nucleotide salvage pathway to satisfy rapid proliferative demand (Kofuji et al., 2019; X. Wang et al., 2017). Genetic knockdown of IMPDH2 in U87MG glioma derived cell lines reduced orthotopic GBM growth (Kofuji et al., 2019). The importance of guanylates to GBM has been also illustrated following radiation therapy, where guanylates are required for repairing DNA double strand breaks. Direct inhibition of de novo guanine nucleotide synthesis with mycophenolic acid (MPA) lowered guanylate levels and further sensitized GBM derived cells to radiation induced cell death (Zhou et al., 2020). Such precedents point to a potentially actionable GBM vulnerability should effective BBB penetrating agents become available (Kofuji et al., 2019; Valvezan et al., 2020).

Mycophenolate mofetil (MMF), also known as CellCept®, is currently widely used in the clinic as an immunosuppressant for organ transplantations and

autoimmune diseases. It is the prodrug of MPA. Its active form, MPA, was first isolated from the fungus P. brevicompactum in 1893 and regained scientific and clinical attention around the 1950s. It is now known that MMF/MPA functions as an IMPDH inhibitor, with MPA being five times more potent in inhibiting IMPDH2 than IMPDH1. MMF was eventually approved by the FDA in 1995 for clinical use.

Personal communications with Dr. Sasaki (the corresponding author of Kofuji et al., 2019, which demonstrated IMPDH2 as a vulnerability in GBM) revealed their unsuccessful attempts to work with MMF *in vivo*. However, there have been two recent studies demonstrating that the combination of MMF with Temozolomide (Shireman et al., 2021) or radiation (Zhou et al., 2020) increases the survival of PDX GBM models. Moreover, a recent phase 1 clinical trial involving thirty recurrent glioblastoma patients treated with chemoradiation plus MMF reported successful detection of the drug in tumor tissue (harvested during surgery) using mass spectrometry (Umemura et al., 2022). However, though this suggests that MMF may have the ability to reach brain tumor tissue, the details for MMF concentration in tumor tissue was not disclosed. A formal evaluation of the blood-brain barrier penetrability of MMF is still needed.

**Identifying the drug target of for small molecules**

The most challenging aspect of the Gliocidin project is to determine its drug target. In contrast to Gboxin and 4C12 (i.e. the other two candidate compounds that were derived from the chemical library screen), where drug target and mechanistic insights were elucidated through conventional chemical labeling

coupled with mass spectrometry (Gboxin) and transcriptomic analysis (4C12), respectively, the process of identifying the drug target of Gliocidin presentedgreater complexity and challenges.

Being a small molecule, we have conducted studies with various Gliocidin analogs, synthesized in collaboration with the DeBrabander lab at UTSW, to explore its structure-activity relationship. However, all synthesized analogs exhibited no activity against tumor cells, indicating that the chemical structure of Gliocidin may have reached its minimalistic limit and was not amenable to further modification. Furthermore, gene set enrichment analysis of Gliocidin-treated transcriptomic data (shown in supplemental figure 1) failed to identify specific biological pathways or enzymes associated with its action. Consequently, we contemplated employing a genome-wide CRISPR-Cas9 screen to identify functional regulators of Gliocidin sensitivity in tumor cells. Moreover, we endeavored to deduce the potential biological pathway through which Gliocidin exerts its effects and, if possible, hypothesize potential Gliocidin target protein.

Through our CRISPR screen, we made two significant biological observations that led us to identify IMPDH in the *de novo* purine synthesis pathway as the drug target for Gliocidin. The first observation was that tumor cells became resistant to Gliocidin when we knocked out the *de novo* nucleotide synthesis genes. Initially, this finding seemed counterintuitive, as these enzymes are essential for tumor cells to proliferate. However, we hypothesized that the loss of *de novo* synthesis genes might cause a shift of nucleotide source to the salvage pathway. We have demonstrated this point by co-deleting *Hprt* and *de novo* purine synthesis

enzymes, which re-conferred the tumor cells sensitivity to Gliocidin. This nucleotide dependency shift suggested that the activation of the salvage pathway is a resistance mechanism to Gliocidin. By backwards reasoning, this implied that Gliocidin mechanistically inhibits *de novo* synthesis of nucleotides.

The second observation from our CRISPR screen revealed that the sensitivity of tumor cells to Gliocidin depends on mTORC1 activity. Specifically, the activation of mTORC1 sensitizes tumor cells to Gliocidin, while dampening mTORC1 activity renders cells resistant to Gliocidin. To understand the relationship between mTORC1 activity and *de novo* nucleotide synthesis, we conducted a literature search and found studies from the lab of Dr. Brendan Manning indicating that the *de novo* purine synthesis pathway is regulated by mTORC1. Knockout of core *de novo* purine enzymes, such as *Pfas*, *Ppat*, and *Gart*, decreased mTORC1 activity in cells, signaling a regulatory feedback to decrease mTORC1-dependent anabolic processes, such as translation, rRNA, and ribosome biogenesis in the deficiency of nucleotides.

In contrast, knockout of enzymes in the guanylate synthesis branch, such as IMPDH, does not lead to feedback inhibition of mTORC1. Valvezan et al. demonstrated that Mizoribine, an IMPDH inhibitor, phenocopies the effect of IMPDH2 knockout in terms of mTORC1 activity. The biological consequence of IMPDH2 inhibition is the blockage of guanine nucleotide synthesis without toning down mTORC1, causing a constant flux of nucleotide consumption for anabolic processes. This double blow, synthesis inhibition and lack of brakes on mTORC1

mediated nucleotide consumption, exacerbates the intracellular nucleotide pool deficiency, eventually leading to replication stress and cell death.

In summary, these two important pieces of data led us to hypothesize that Gliocidin may be inhibiting *de novo* guanine nucleotide synthesis. This was immediately tested by co-supplementing Gliocidin treated tumor cells with guanosine. After multiple drug target hypotheses were tested and rejected in the early phase of this project, the strong phenotype of guanosine rescue paved the way for the study of the remaining mechanistic underpinnings onwards.

Hence, in scenarios involving small molecules where conventional label affinity approach for target identification or transcriptomic analyses fall short in yielding substantive biological insights, the implementation of functional experiments through genome-wide CRISPR screens becomes useful. Nevertheless, assiduous and meticulous interpretations of the CRISPR screen must be ensured, as essential information may inadvertently elude attention.

**Identification of the first substrate of the mammalian GID complex**

The structure of the GID complex has been elucidated through cryo-electron microscopy techniques, shedding light on its organizational framework (Sherpa et al., 2021). However, a comprehensive understanding of the role of mammalian GID complex remains incomplete. Despite notable homology between the yeast and mammalian GID complexes, their regulatory functions diverge, particularly concerning substrate degradation.

The GID complex, denoting glucose-induced degradation, was originally identified in yeast cells. Under conditions rich in glucose, gluconeogenic enzymes (fructose-1,6-bisphosphatase (Fbp1), phosphoenolpyruvate carboxykinase (Pck1), cytoplasmic malate dehydrogenase (Mdh2), and isocitrate lyase (Icl1)) undergo degradation via the CTLH/GID complex (Santt et al., 2008). Efforts have been made to extrapolate this mechanism to the mammalian GID complex. However, disparities persist, and this phenomenon does not seem to hold true in the context of the mammalian GID complex. Consequently, the quest for identifying substrates of the mammalian GID complex remains ongoing.

Recently, the potential designation of Hbp1 as a substrate for the human GID complex emerged (Lampert et al., 2018). Perturbing the essential component of the GID complex, WDR26, led to elevated HBP1 protein levels. An in vitro ubiquitination assay involving reconstituted GID complex and HBP1 corroborated this proposition, although ubiquitination levels remained modest. Our own investigations using murine glioma cells did not validate this finding, as HBP1 upregulation was absent in our proteomic data. Correspondence with the Schulman group corroborates the absence of definitive evidence concerning mammalian GID complex substrates.

The GID complex, a supramolecular assembly of 1.5 MDa, exhibits remarkable conservation across eukaryotes, implying its functional importance throughout evolution. Our serendipitous discovery of YPEL5 as a negative regulator of the GID complex, governing NMNAT1 degradation, was an unforeseen breakthrough in the GID complex biology. Through personal communications with

the Schulman group, we initially presented our hypothetical model proposing the role of YPEL5 as a negative regulator of the GID complex for NMNAT1 regulation. Subsequently, we were informed that they have also reached a similar conclusion through orthogonal approach involving an *in vitro* ubiquitylome asasy. In which later our *in vivo* (i.e., referring to the cellular context, as opposed to their *in vitro* biochemical context) findings prompted the Schulman team to conduct an in vitro ubiquitination assay involving NMNAT1 within the reconstituted GID complex, both in the presence and absence of YPEL5. Their subsequent biochemical analyses underscored substantial ubiquitylation of the NMNAT1 protein solely within the reconstituted GID complex in the absence of YPEL5, and not when YPEL5 is present.

In a broader context, it is evident that both yeast and mammalian GID complexes exert an impact on metabolic enzymes, thereby emphasizing their potential roles in carbohydrate enzyme metabolism. This prompts consideration that the regulatory reach of the GID complex could extend to further enzymes, contingent upon distinct cellular contexts.

## Methods

### Cell culture experiments

All *in vitro* murine tumor cells were maintained in a 5% oxygen cell culture incubator and cultured with serum-free media (SFM). The SFM consisted of DMEM/F-12, N2 (GeminiBio #400-163), B27 without vitamin A (Gibco #17-504-044), EGF (10ng/mL; Gibco #PHG0311), bFGF (10ng/mL; Gemini #300-113P), glutamine (Gibco #25030081), sodium pyruvate (Gibco #11360070), penicillin/streptomycin (Gibco #15140122), glucose (Sigma #G8270), bicarbonate (Gibco # 25080-094), and HEPES (Sigma #3375). Primary mouse embryonic fibroblasts (MEFs) were generated from E13.5-14.5 mouse embryos. The MEFs were maintained in a normoxia oxygen (21% $O_2$) cell culture incubator and cultured in DMEM (Sigma #5796) supplemented with 10% heat-inactivated fetal bovine serum (Sigma #12303C) and 1% penicillin/streptomycin.

For all compound dose-response experiments, cells were seeded at a density of 1.0 x $10^3$ (NG2-3112 and NST-1329) or 2.0 x $10^3$ (human PDXs) per well in a 96-well plate. They were incubated for 14-16 hours before drug treatment and cultured for an additional 96 hours before luminescence reading (CellTiterGlo®) using a Cytation 5 image reader (Agilent).

### GBM PDX primary culture

Patient-derived xenograft (PDX) tumors were harvested from mice bearing intracranial PDX and dissociated into a single-cell suspension using papain (Worthington Biochemical #NC9597281) in L15 media, as described previously

(Xie et al., 2022). PDX tumor cells were cultured and passaged in serum-free media (SFM) with the addition of PDGF-AA (10ng/mL).

**Chemical Compounds**

The following chemical compounds were added into the culture medium at final concentrations indicated in the figure legends: Mizoribine (Sigma #M3047), Mycophenolic acid (Sigma #M3536), Rapamycin (MedChemExpress #HY-10219), Temozolomide (Sigma #PHR1437), guanosine (Sigma #G6752), adenosine (Sigma #01890), thymidine (Sigma #T1895), cytidine (Sigma #122106), uridine (Sigma #U3750). All Gliocidin and its derivatives were synthesized by the MSKCC Organic Synthesis Core as described in the Gliocidin and Derivatives Synthesis method section below.

**Genome-wide CRISPR-Cas Screen and validation experiments**

NG2-3112 cells were transduced with lentiCas9-Blast (Addgene #52962) and selected with 10 mg/ml blasticidin for one week. A single clone was chosen, expanded, and validated for Cas9 expression before downstream applications. The Brie Mouse CRISPR Knockout Pooled Library (Addgene #73633), which targets the mouse genome, was used for the genome-wide CRISPR-Cas9 screen. This library contains sgRNAs targeting 78,637 genes and 1,000 non-targeting controls. For the screen, 150 mm dishes (Corning 430599) coated with laminin (Cultrex Mouse Laminin I, Pathclear; R&D 3400-010-02) and Poly-D-Lysine (Sigma P6407) were utilized. To ensure 1,000-fold representation of sgRNAs, 2.66

x $10^8$ cells were seeded into multiple 150 mm dishes at a confluency of 50% and transduced with the Brie Mouse CRISPR Knockout Pooled Library at a MOI of 0.3. Cells were incubated for 48 hours, followed by the addition of 3 ug/mL puromycin for another 48 hours of selection. After puromycin selection, the dishes were replaced with fresh media for three additional days to allow for recovery. At T0 (time point zero), 2.274 x $10^8$ cells were harvested, pelleted, and frozen as the T0 control. Subsequently, 7.7441 x $10^7$ cells were seeded and treated with vehicle, 250nM (IC50) Gliocidin, or 750nM (IC80) Gliocidin for 10 doubling times (T14). Cells were passaged every 4-5 days. At T14, the cells were harvested, pelleted, and frozen. The experiments were performed in duplicates. Samples were then extracted for genomic DNA and sequenced using the Illumina HiSeq platform at MSKCC Gene Editing and Screening Core.

**Genome CRISPR-Cas9 screen analysis**

The raw sequencing data from the CRISPR-Cas9 screen were aligned and analyzed using the MAGeCK algorithm (Doench et al., 2016). Quality control was conducted on all datasets using the MAGeCK count function. All replicate samples showed a mapping success rate of approximately 80% (range: 77.1-80.7%). The MAGeCK MLE method was employed to analyze the read counts of sgRNAs and to curate two types of gene list: 1) "essential genes" based on differential sgRNA abundance between T0 and T14 DMSO samples, and 2) "Gliocidin-dependent genes" by examining the differential sgRNA abundance between T14 DMSO-treated and Gliocidin-treated ($IC_{50}$ or $IC_{80}$) samples. For each gene list, a β score

was assigned to all genes: a positive β score indicated positive (enrichment) selection, and a negative β score indicated negative (depletion) selection of sgRNAs. A gene was considered significantly enriched or depleted if the false discovery rate (FDR) was less than 0.05.

**Hit validation experiments**

sgRNAs for target validation were cloned into LentiGuide-Puro vector backbone (Addgene #52963) using methods decribed previously by the Zheng group. Lentivirus was generated by co-transfecting the LentiGuide-Puro plasmids containing sgRNAs, pMD2.G (Addgene #12259), and psPAX2 (Addgene #12260) into 293T cells. Tumor cells were transduced, and knockout was confirmed by the loss of protein expression through Western Blot analysis. For knockout experiments targeted against mTOR regulators (Figure 2), 10,000 cells were seeded into each well of 6-well plate and treated the following day with 0.125 μM Gliocidin for 6 days before cell counting using the Countess II Automated Cell Counter. For all other KO cells treated with compounds, experiments were conducted as described in the “Cell culture experiments” section above.

**Drug Washout Assay**

Prior to cell seeding, 96-well plates were coated overnight with Poly-D-lysine (33.3 μg/mL, Sigma #P6407) and laminin (20 μg/mL, R&D #3400-010-02). A total of 1.0 x $10^3$ cells per well were seeded and incubated overnight before Gliocidin treatment. At the designated time points (3, 6, 24, 48, 72, and 96 hours), fresh

serum-free media were added to each well and subsequently removed by gentle pipet aspiration. This process was repeated two more times. The plates were then placed back in a 37°C incubator. At the 96-hour time point, the plates were subjected to luminescence reading (CellTiterGlo®) using the Cytation 5 image reader to assess cell viability.

**Western Blots**

Tumor cells were harvested and lysed in RIPA buffer containing protease inhibitor cocktail (cOmplete™, Mini, EDTA-free Protease Inhibitor Cocktail; Sigma# 11836170001) and phosphatase inhibitor (PhosSTOP™, Sigma# 4906837001). The lysates were incubated on ice for 15 minutes. Subsequently, the cells were homogenized by sonication and centrifuged at 10,000g for 15 minutes at 4°C. The supernatant was collected, and 4x Pierce™ LDS Sample Buffer (Thermo Scientific #84788) was added to the samples, which were then boiled at 95°C for 10 minutes. SDS-PAGE was performed using 4-20% precast protein gels (Bio-Rad #4561096). For membrane transfer, PVDF membranes was utilized and wet transferred at a constant voltage of 100V for one hour at 4°C. 5% bovine serum albumin (BSA, Sigma#A9647) in TBST (0.1% Tween20) solution was used for membrane blocking at room temperature for one hour. Primary and secondary antibodies were prepared in 5% BSA-TBST. The membranes were incubated overnight with the primary antibody. After three 5-minute washes, the membranes were incubated with secondary HRP antibodies for one hour. Following three more rounds of washing with TBST, the membranes were incubated with an enhanced

chemiluminescent detection reagent (Cytiva RPN2106), and the protein signal was detected using autoradiography films (LabScientific XAR ALF 1318).

**RNA Bulk Sequencing and analysis**

Total RNA was isolated from tumors using the Direct-zol™ RNA MicroPrep (Zymo Research #R2060). Following RNA isolation, total RNA integrity was checked using a 2100 Bioanalyzer (Agilent Technologies, Santa Clara, CA). RNA concentrations were measured using the NanoDrop system (Thermo Fisher Scientific, Inc., Waltham, MA). Preparation of RNA sample library and RNA-seq were performed by the Genomics Core Laboratory at Weill Cornell Medicine. Messenger RNA was prepared using TruSeqStranded mRNA Sample Library Preparation kit (Illumina, San Diego, CA), according to the manufacturer's instructions. The normalized cDNA libraries were pooled and sequenced on Illumina NovaSeq 6000 sequencer with pair-end 50 cycles. The raw sequencing reads in BCL format were processed through bcl2fastq 2.19 (Illumina) for FASTQ conversion and demultiplexing.

The raw reads were then aligned using STAR(version 2.5.3a) with default settings using reference human genome (Ensembl, GRCh37.p13). The counts for each gene were generated by STAR using the commands quantMode and GeneCounts. The R package BiomaRt was utilized to convert mouse Ensembl gene IDs into gene symbols. The R package DESeq2 was used to determine differential gene expression between Gliocidin and DMSO treated samples. Data visualization plots were generated using the R package ggplot2.

**Tissue processing and single cell sequencing of temozolomide treated PDX tumors**

Low-passage PDX tumor tissue was orthotopically implanted into independent athymic nude mice. Tumor development was confirmed by whole brain MRI, and mice randomized to treatment groups. TMZ was dissolved in DMSO and prepared as 20mg/ml stock. Prior to drug administration, TMZ stock solution was further diluted four-fold by PBS into 5mg/ml working solution. The mice were administered either the vehicle or TMZ (50mg/kg/day) for five consecutive days and euthanized on day 6. Fresh PDX tumor tissue was dissociated into a single-cell suspension, enriched for viable cells, and immediately processed using the ChromiumTM instrument (10X Genomics). The experimental details regarding tumor dissociation and single-cell sequencing were previously described (Xie et al., 2022).

**Single Cell RNA Sequencing Analysis**

**Count Matrix Construction and individual sample data curation**

The Illumina fastq files containing the barcoding metadata and transcriptome were demultiplexed using the Sequence Quality Control (SEQC) pipeline (Azizi et al., 2018) into a single fastq file generate error-corrected and uniquely aligned count matrix for each multiplexed sequencing run. Individual samples were analyzed with Seurat (v.4.1.0) in the R environment (v.4.1.3). Empty cells were identified by analyzing percentage of mitochondrial contamination distributions and number of molecules detected in cell (nCount_RNA) and dropped

by applying mitochondrial gene contamination cut off. Doublets and multipletes were identified by analyzing number of features and number of molecules detected in cell and dropped by applying UMI cut off. Dead cells identification of the unsupervised cluster with the lowest spectrum of features and molecules per cell counts (lower than the quiescent cell type) was conducted after projecting integrated samples data into a lower dimension with linear and non-linear (PCA and UMI) reductions methods.

**Individual samples data integration and dimension reductions**

A list of pre-filtered objects was subjected to a feature-wise natural log transformation. This transformation involved dividing the feature counts for each cell by the total counts for that cell, and then multiplying the result by the default scale factor of 10,000 (Seurat::NormalizeData). Subsequently, the data was scaled (Seurat::ScaleData). Linear dimension reduction using PCA was performed based on integration features (Seurat::RunPCA, Seurat::FindVariableFeatures, Seurat::SelectIntegrationFeatures). To integrate the samples, anchors, which represent common sources of variation, were identified through canonical correlation analysis (Seurat::FindIntegrationAnchors, anchor.features = FindIntegrationFeatures, reduction = "cca"). In brief, clusters of co-expressed genes among different samples were identified, evaluated, and used to merge the cells (Butler et al., 2018).

The Elbow plot (Seurat::ElbowPlot) was utilized to analyze the standard deviations explained by each principal component. Consequently, 20 PC

dimensions were selected to represent the initial data in a lower dimension. For projecting unsupervised clusters in two dimensions, UMAP non-linear dimension reduction (Seurat::RunUMAP) was employed. The neighborhood graph was constructed using weighted nearest neighbors (Seurat::FindNeighbors, PC=20, k=30 as the default). Unsupervised clusters were obtained through the Louvain algorithm, employing various resolution parameters (Seurat::FindClusters).

**Identification of cell types**

Cell clusters were determined using previously published GBM cell type (Xie et al., 2022), which includes quiescent glioblastoma stem cells, transcriptionally mixed cells, proliferating cells in S and M phases, oligodendrocytes, and neuronal progenitor cells.

To identify enrichments of these signatures within the clusters, the AUCell non-parametric method (Aibar et al., 2017) was employed. This method assigns a score to each cell based on its similarity to a specific signature. The top 5% of ranked genes per cell were used to determine the proportion of expressed genes within each signature, according to the recommendation of the developers. The subsequent cutoff threshold for enrichment activity per cell was determined based on the distribution of AUC scores. Enrichments of cell types were visualized using kernel-weighted density estimation plots for both the raw and thresholded enriched scores (Nebulosa::plot_densensity)(Alquicira-Hernandez & Powell, 2021).

**Individual gene expression statistics**

The significantly varying distributions of individual log-transformed Nmnat1 expressions among cell groups, differentiated by conditions, were analyzed using a paired Mann-Whitney U non-parametric test. The results were visualized using dot plots (Seurat::DotPlot) to represent the varying scaled expressions.

**Metabolomic Profiling of cellular extracts using LC-MS/MS**

$1.0x10^6$ of NG2-3112, NG2-775 or NST-1329 cells were seeded in a 6-well plate in 2 mL of SFM. Sixteen hours after seeding, Gliocidin was added. After six hours cells of Gliocidin exposure, media was aspirated, cells were placed on ice, and lysed with 1 mL of dry-ice cold 80% methanol/20% water solution. Immediately after, 6-well plates were transferred to -80°C and incubated overnight to allow protein precipitation. Metabolite extracts were clarified by centrifugation at 20,000 g for 20 min at 4 °C and dried in a vacuum evaporator (Genevac EZ-2 Elite) for 3 hours. For metabolomic profiling dried extracts were resuspended in 50 µL of water, vortexed, and incubated on ice for 20 min. Samples were further clarified by centrifugation at 20,000 g for 20 min at 4°C and transferred to autosampler vials for LC-MS acquisition. Ion pair LC-MS/MS analysis was performed with a separation on a Zorbax RRHD Extend-C18 column (150 mm × 2.1 mm, 1.8 µm particle size, Agilent Technologies), and using gradient of solvent A (10 mM tributylamine and 15 mM acetic acid in 97:3 water:methanol) and solvent B (10 mM tributylamine and 15 mM acetic acid in methanol) according to the manufacturer's instructions (MassHunter Metabolomics dMRM Database and

Method, Agilent Technologies). For this analysis, acquisition was performed using an Agilent 6470 LC-MS/MS triple quadrupole. Data analysis was performed with MassHunter Workstation Software for Quantitative analysis vB10.2 (Agilent Technologies).

**LC-MS/MS for Gliocidin derivatives**

8.0 x $10^6$ NG2-3112 cells were seeded in 100mm dishes and treated with vehicle or 2.5uM Gliocidin for 10 hours. The cells were then resuspended in 1 mL of an ice-cold mixture of methanol and water in a 4:1 ratio. The sample was subsequently incubated at -80 °C for 1 hour and centrifuged at 21,000 g for 10 minutes to precipitate protein. From the resulting clarified supernatant, 850 µL was transferred to a 96-well plate, dried using a speedvac, and resuspended in 140 µL of a 1:1 mixture of methanol and water for LC-MS analysis. The LC-MS/MS analysis was performed using a Sciex X500R quadrupole time-of-flight (qTOF) mass spectrometer coupled to ExionLC. The Turboionspray ESI source was set with the following parameters: curtain gas at 30 psi, ion source gas1 at 50 psi, ion source gas 2 at 50 psi, temperature at 500 °C, positive polarity, spray voltage at 5500 V, CAD gas at 7, declustering potential at 80 V, collision energy at 5 V, TOF start mass at 100 Da, and TOF stop mass at 1000 Da. MS/MS was conducted with the same parameters, except the collision energy was set at 40 V, and the TOF start mass was set at 50 Da. The sample was separated using a Waters Acquity UPLC HSST3 1.8 µm 2.1 x 100 mm column maintained at 40 °C. The mobile phase consisted of buffer A (0.1% formic acid in water) and buffer B (0.1% formic acid in

acetonitrile). The LC gradient was as follows: 0-1.5 min: 5% B, 1.5-10 min: linear gradient from 5% to 20% B, 10-12 min: 95% B, 12-15 min: 5% B. The flow rate was set at 0.4 mL/min. The raw wiff2 data was converted to mzXML format using MSConvert (Chambers et al., 2012) in ProteoWizard, and the targeted feature detection of MZmine 2.53 (Pluskal et al., 2010) was used to quantify the indicated m/z with a tolerance of 20 ppm.

**Quantitative Proteomics**

Cell pellets were lysed with 300 µL buffer containing 8 M urea and 200 mM EPPS (pH at 8.5) with protease inhibitor (Roche) and phosphatase inhibitor cocktails 2 and 3 (Sigma). Benzonase (Millipore) was added to a concentration of 50u/mL and incubated (RT, 15 min) followed by water bath sonication. Samples were centrifuged at 4°C, 14,000 g's for 10 min and supernatant extracted. The Pierce bicinchoninic acid (BCA) protein concentration assay was used for determining protein concentration. Protein disulfide bonds were reduced with 5 mM tris (2-carboxyethyl) phosphine (room temperature, 15 min), then alkylated with 10 mM iodoacetamide (RT, 30 min, dark). The reaction was quenched with 10 mM dithiothreitol (RT, 15 min). Aliquots of 100 ug were taken for each sample and diluted to approximately 100 µL with lysis buffer. Samples were subject to chloroform/methanol precipitation as previously described[1]. Pellets were reconstituted in 200mM EPPS buffer and digested with Lys-C (1:50 enzyme-to-protein ratio) and trypsin (1:50 enzyme-to-protein ratio). Digested at 37°C overnight.

Peptides were TMT-labeled as described (Navarrete-Perea et al., 2018). Briefly, peptides were TMT-tagged by addition of anhydrous ACN and TMTPro reagents (16plex) for each respective sample and incubated for 1 hr (RT). A ratio check was performed by taking a 1 µL aliquot from each sample and desalted by StageTip method (Rappsilber et al., 2007). TMT-tags were then quenched with hydroxylamine to a final concentration of 0.3% for 15 min (RT). Samples were pooled 1:1 based on the ratio check and vacuum-centrifuged to dryness. Dried peptides were reconstituted in 1mL of 3% ACN/1% TFA, desalted using a 100mg tC18 SepPak (Waters), and vacuum-centrifuged overnight.

Peptides were centrifuged to dryness and reconstituted in 1 mL of 1% ACN/25mM ABC. Peptides were fractionated into 48 fractions. Briefly, an Ultimate 3000 HPLC (Dionex) coupled to an Ultimate 3000 Fraction Collector using a Waters XBridge BEH130 C18 column (3.5 um 4.6 x 250 mm) was operated at 1 mL/min. Buffer A, B, and C consisted of 100% water, 100% ACN, and 25mM ABC, respectively. The fractionation gradient operated as follows: 1% B to 5% B in 1 min, 5% B to 35% B in 61 min, 35% B to 60% B in 5 min, 60% B to 70% B in 3 min, 70% B to 1% B in 10min, with 10% C the entire gradient to maintain pH. The 48 fractions were then concatenated to 12 fractions, (i.e. fractions 1, 13, 25, 37 were pooled, followed by fractions 2, 14, 26, 38, etc.) so that every $12^{th}$ fraction was used to pool. Pooled fractions were vacuum-centrifuged then reconstituted in 1% ACN/0.1% FA for LC-MS/MS.

Total peptide fractions were analyzed by LC-MS/MS using a Thermo Easy-nLC 1200 (Thermo Fisher Scientific) with a 50 cm (inner diameter 75µm) EASY-Spray

Column (PepMap RSLC, C18, 2µm, 100Å) heated to 60°C coupled to a Orbitrap Fusion Lumos Tribrid Mass Spectrometer (Thermo Fisher Scientific). Peptides were separated at a flow rate of 300nL/min using a linear gradient of 1 to 30% acetonitrile (0.1% FA) in water (0.1% FA) over 4 hours and analyzed by SPS-MS3. MS1 scans were acquired over a range of m/z 375-1500, 120 K resolution, AGC target (4.0 e5), and maximum IT of 50 ms. MS2 scans were acquired on MS1 scans of charge 2-7 using an isolation of 0.7 m/z, collision induced dissociation with activation of 32%, turbo scan and max IT of 50 ms. MS3 scans were acquired using specific precursor selection (SPS) of 10 isolation notches, m/z range 100-1000, 50K resolution, AGC target (1.0 e5), HCD activation of 45%, and max IT of 150ms. The dynamic exclusion was set at 60s.

Raw data files were processed using Proteome Discoverer (PD) version 2.4.1.15 (Thermo Scientific). For each of the TMT experiments, raw files from all fractions were merged and searched with the SEQUEST HT search engine with a Mouse UniProt protein database downloaded on 2019/12/13. Cysteine carbamidomethylation was specified as fixed modifications, while oxidation (M), acetylation of the protein N-terminus, TMTpro (K) and TMTpro (N-term), Deamidation (NQ), and Phosphorylation (S, T, Y) were set as variable modifications. The precursor and fragment mass tolerances were 10 ppm and 0.6 Da respectively. A maximum of two trypsin missed cleavages were permitted. Searches used a reversed sequence decoy strategy to control peptide false discovery rate (FDR) and 1% FDR was set as threshold for identification.

**Animal Studies**

All mouse experiments were approved and performed in accordance with the guidelines of the Instiutional Animal Care and Use Committee (IACUC) of Memorial Sloan Kettering Cancer Center.

**Gliocidin subcutaneous tumor model**

NST-1329 cells ($2.0x10^5$) were subcutaneously implanted onto the flanks of athymic nude mice. Palpable tumors ($50mm^3$) appeared three weeks after implantation. Administration of Gliocidin (50mg/kg, I.P., twice per day) or vehicle started three weeks after tumor cell implantation, and tumor size was measured every four days using a digital caliper. After receiving 12 days of vehicle or Gliocidin administration, the mice were euthanized.

**Orthotopic tumor implantation models**

To generate NST-1329 orthotopic tumor mice, $5.0 \times 10^4$ cells were injected into the dorsal striatum of 5-6-week-old athymic nude or C57BL/6J mice. To generate orthotopic PDX-160403-1R mice carrying control GFP or Nmnat1-GFP overexpression tumors, PDX-160403-1R cells were first transduced in vitro with lentivirus carrying either the pLV-C-GFPSpark control plasmid (SinoBiological #LVCV-35) or the pLV-NMNAT1-GFPSpark overexpression plasmid (SinoBiological #HG11448-ACGLN). GFP-expressing tumor cells were enriched using fluorescence-activated cell sorting (FACS) and expanded in culture to obtain a sufficient quantity for stereotactic intracranial injection. Subsequently, $5.0 \times 10^4$

cells were injected into 5-6-week-old athymic nude mice. All mice were injected at the following coordinates: 0.5mm AP, -1.7mm ML, 4.0mm DV with respect to the bregma.

### *In vivo* Gliocidin administration

The *in vivo* Gliocidin formulation consists of 25g of Gliocidin powder, 500uL ethanol, 500uL PEG400 and 4000uL PBS (added in this exact sequence with vortexing in between each addition). Final solution is vortexed until the mixture becomes transparent. For *in vivo* administration of 50mg/kg per 25g mouse, 200µL of Gliocidin solution was administered intraperitoneally.

### Patient Derived Xenografts

PDXs were established by the Brain Tumor Center at Memorial Sloan Kettering Cancer Center as previously described (Xie et al., 2022). All patients provided written informed consent for use of specimens and all studies were performed under approval and oversight by the MSKCC Institutional Review Board and IACUC.

### Blood counts and electrolytes

Eight C57BL/6J mice were administered either the vehicle or Gliocidin (50mg/kg, IP, twice a day) for 10 days. On day 10, the mice were euthanized with Ketamine, and blood was drawn through intra-cardiac puncture. Complete blood counts were analyzed using the Idexx Procyte Dx Hematology Analyzer.

**Pharmacokinetics Study**

Female NCR-nu/nu mice were dosed IP with 10 mg/kg Gliocidin, 0.2 ml/mouse formulated as 10% Ethanol, 10% PEG400, 80% D5W pH 7.4 (5% dextrose in $dH_20$). Whole blood was harvested. Plasma was processed from whole blood by centrifugation of the anti-coagulant (acidified citrate dextrose) treated blood for 10' at 9,600 x g in a standard microcentrifuge. Brain and liver were collected and gently washed with 1x PBS to remove residual circulating blood. Then tissue was weighed and snap frozen in liquid nitrogen.

For plasma processing, standards and quality control (QC) samples were prepared by spiking blank CD1 mouse plasma (BioIVT, Westbury, NY) with varying concentrations of Gliocidin DMSO stocks. A two-fold volume of methanol containing 0.15% formic acid (ThermoFisher Scientific, Waltham, MA) and the internal standard n-benzylbenzamide (Sigma, St. Louis, MO) was added to each standard and sample to precipitate plasma proteins. The samples were vortexed 15 sec, incubated at room temp for 10' and spun 2x 16,100 x g in a standard microcentrifuge. The supernatant was then analyzed by LC-MS/MS as described below.

For brain processing, brain tissues were homogenized in a three-fold volume of PBS by weight and then the supernatant was processed as described above. Blank brain from untreated CD1 mice was used to prepare standards and QCs Using literature values for the volume of blood in the blood vessels of the

brain (Kwon, 2001) and the measured concentration of Giocidin in plasma, tissue brain concentrations were adjusted to account for drug present in brain vasculature.

Gliocidin levels in mouse plasma and brain were monitored by LC-MS/MS using an AB Sciex (Framingham, MA) 4000 QTRAP® mass spectrometer coupled to a Shimadzu (Columbia, MD) Prominence LC. Gliocidin was detected with the mass spectrometer in positive MRM (multiple reaction monitoring) mode by following the precursor to fragment ion transitions 205.193 to 111.0. An Agilent C18 XDB column (5 micron, 50 X 4.6 mm) was used for chromatography for PK studies with the following conditions: Buffer A: dH20 + 0.1% formic acid, Buffer B: methanol + 0.1% formic acid, 0 - 1.5 min 3% B, 1.5 – 3.0 min gradient to 100% B, 3.0 - 4.0 min 100% B, 4.0 – 4.1 min gradient to 3% B, 4.1- 5.0 3% B. N-benzylbenzamide (transition 212.12 to 91.0) was used as an internal standard (IS).

**Whole Brain GFP Fluorescent Imaging**

PDX-160403-1R cells overexpressing Nmnat1 were injected into the striatum of mice. Brain tumors were confirmed using MRI, and the mice were subsequently injected with either the vehicle or Gliocidin (50mg/kg, IP, twice daily) for 7 days. Afterward, the mice were euthanized, and their brains were extracted. The tumor signal was quantified using IVIS imaging.

**Chemical Synthesis of Gliocidin and derivatives**

All reagents were purchased in highest quality available from commercial vendors and were used without further purification. Proton, carbon, fluorine and phosphorus

NMRs were run on a Bruker Avance III 600 (Bruker Daltonics). Reaction monitoring was done an Acquity Premier SQD2 (Waters) with parallel detection by mass spec, diode array and evaporative light scattering (ELS). Preparative HPLC was run on an AutoPure system (Waters) also using similar parallel detection setting as above.

**Brain Magnetic Resonance Imaging (MRI)**

Mouse brains were imaged on a 9.4-Tesla Biospec scanner (Bruker Biospin Corp., Billerica, MA) with a 12-cm Bruker gradient coil (maximum gradient strength 528 mT/m). A Bruker ID 4 cm quadrature volume coil was used for RF excitation and detection. During imaging sessions mice were anesthetized with 1-2% isoflurane gas in oxygen and were positioned prone in the scanner. First T2-weighted scout images along 3 orthogonal orientations were acquired. Then T2-weighted mouse brain images along the trans-axial orientation were acquired covering the whole brain using the RARE (Rapid Acquisition with Relaxation Enhancement) fast spin-echo sequence with the following acquisition parameters: slice thickness of 0.5 mm, repetition time 2.5 s, echo time, 33 ms, RARE factor 8, and a spatial resolution of 98 x 78 mm.

**Chemical Structures**

All chemical structures were generated by ChemDraw 22.

**Synthesis of Gliocidin (N-3-Pyridinyl-2-thiophenecarboxamide)(Zhang et al., 2007)**

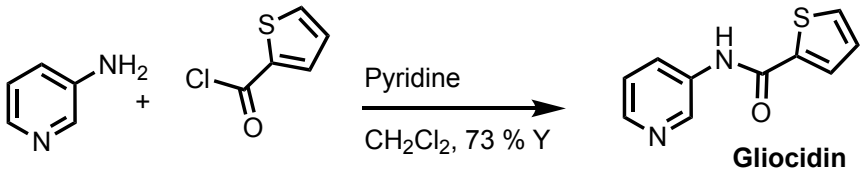


**Gliocidin**

A solution of thiophene-2-carbonyl chloride (16.77 g, 0.114 mol) in dichloromethane (DCM) (50 mL) was added dropwise to a solution of 3-amino pyridine (10.34 g, 0.11 mol) in DCM (100 mL) and anhydrous pyridine (10.8 mL) at 0 °C. After 3 h of stirring at room temperature, the precipitate was filtered and washed with DCM, the organic solution was washed with water followed by sat. $NaHCO_3$. The combined organic layers were washed with brine, dried over anhydrous $Na_2SO_4$, and then concentrated in vacuo. The crude product was treated with ethyl acetate and hexanes to get white solids as HCl salt. The white solids (18 g) were dissolved in MeOH (100 mL), then treated with prewashed basic resin 20 g of Dowex 550A-OH, stirred for 1 h. The mixture was then filtered and washed the resin with MeOH. The filtrate was concentrated in vacuo and the product was dried under vacuum to afford 16.1 g product as white powder (73% yield). $^1$H NMR (600 MHz, $CDCl_3$), $\delta$ 8.71 (d, J = 2.5 Hz, 1H), 8.37 (dd, J = 1.4, 4.7 Hz, 1H), 8.30 (m, 1H), 8.22 (brs, 1H), 7.74 (dd, J = 1.1, 3.8 Hz, 1H), 7.58 (dd, J = 1.1, 5.0 Hz, 1H), 7.32 (dd, J = 4.7, 8.3 Hz, 1H), 7.13 (dd, J = 3.7, 4.9 Hz, 1H); $^{13}$C NMR (600 MHz, $CDCl_3$), $\delta$ 160.46, 145.06, 141.16, 138.44, 134.88, 131.50, 129.15, 128.01, 123.94; ); ES MS calc. for $C_{10}H_8N_2OS$ 204.04, found 205.19 (M+H); mp 144.5-145.5 °C, comparing to mp 143-145 °C (Bollenbach et al., 2017) and 145-146 °C (Ikawa et al., 2007).

**Synthesis of Gliocidin-Ribose**

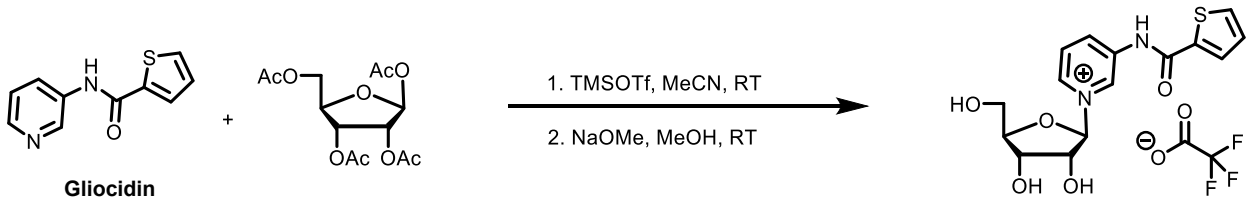


**Gliocidin** **Gliocidin-R**

To a solution of Gliocidin (500.0 mg, 2.27 mmole) and β-D-ribofuranose 1,2,3,5-tetraacetate (873 mg, 2.74 mmole) in acetonitrile (20 mL) were added TMSOTf (0.5 mL, 2.75 mmole) dropwise at RT under an argon atmosphere over about 6 minutes. The resulting mixture was stirred at RT overnight. The solvents were then concentrated under reduced pressure and the residue was dissolved in MeOH (12 mL), and 0.5 Molar sodium methoxide in methanol was added to the reaction mixture until the pH reaches 9.0 (pH paper). After stirring at RT for 3h, the reaction was neutralized by addition of 2.0 N HCl. When pH 7.0 (pH paper) is reached, the reaction mixture was concentrated under reduced pressure and the residue was purified by reverse phase HPLC (Column: XBridge Prep C18, 5µm OBD, 19x150 mm; using the gradient: 15 to 25% acetonitrile (with 0.05% TFA) in water (with 0.05% TFA). The appropriate elution fractions were pooled and lyophilized, giving Gliocidin-R (667 mg, 65%) and unreacted starting material GLIOCIDIN-21 (173 mg). $^{1}$H NMR (600 MHz, $D_2O$) δ 9.60 (s, 1H), 8.78 (d, J = 6.1 Hz, 1H), 8.55 (ddd, J = 8.5 Hz, J = 2.0 Hz, J = 0.8 Hz, 1H), 8.02 (dd, J = 8.5 Hz, J = 6.1 Hz, 1H), 7.88 (dd, J = 3.8 Hz, J = 1.1 Hz, 1H), 7.77 (dd, J = 5.0 Hz, J = 1.1 Hz, 1H), 7.18 (dd, J = 5.0 Hz, J = 3.9 Hz, 1H), 6.10 (d, J = 5.5 Hz, 1H), 4.43-4.40 (m, 2H), 4.27 (dd, J = 4.9 Hz, J = 4.0 Hz, 1H), 3.94 (dd, J = 12.8 Hz, J = 3.1 Hz,

1H), 3.84 (dd, J = 12.8 Hz, J = 4.2 Hz, 1H). $^{13}$C NMR (150.9 MHz, $D_2O$) δ 163.1, 139.0, 137.3, 136.2, 135.5, 133.9, 131.8, 131.6, 128.6, 128.1, 99.8, 87.9, 77.6, 70.3, 60.7. $^{19}$F NMR (564.7 MHz, $D_2O$) δ -75.60. HRMS (ESI) $[M]^+$ calculated for $C_{15}H_{17}N_2O_5S^+$: 337.0858. Found: 337.0871.

**Synthesis of Gliocidin-Mononucleotide**

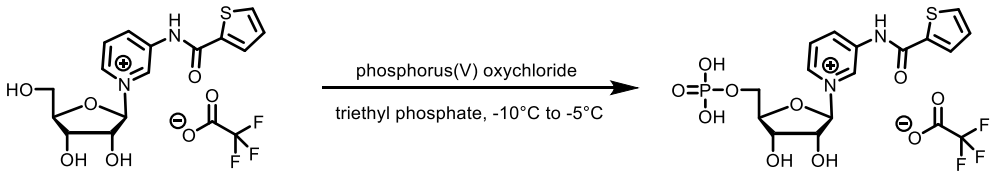


**Gliocidin-R** **Gliocidin-MN**

To a solution of Gliocidin-R (82 mg, 0.18 mmol) in triethyl phosphate (300 µL) was added a solution of phosphoryl chloride (37.5 µL, 0.4 mmol) in triethyl phosphate (300 µL) dropwise while maintaining temperature between -10 °C and -5 °C. Stirring was maintained at -10 °C to -5 °C for 3 hours before additional phosphoryl chloride (25 µL, 0.27 mmol) in triethyl phosphate (200 µL) was introduced in a dropwise fashion. After 2 hours at -10 °C to -5 °C, ice (1 g) was carefully added and stirring was continued for another hour at -10 °C to -5 °C. The reaction mixture was then treated with 2.0 N sodium hydroxide (1.2 mL) slowly at the same temperature and until a final pH reached 11 (pH paper). The reaction mixture was allowed to warm up to the ambient before washing with ethyl acetate (2 mL × 5). The aqueous layer was diluted to 5 mL with acetonitrile / water (1 / 1 both containing 0.05% TFA) and purified by prep HPLC (Column: XBridge Prep C18 5µm OBD, 19x150 mm; using the gradient: 5 to 20% acetonitrile (with 0.05% TFA)in water (with 0.05% TFA). The combined elution fractions were lyophilized, giving Gliocidin-MN (46 mg, 48% yield) as white foam. $^1$H NMR (600 MHz, $D_2O$) δ

9.45 (s, 1H), 8.75 (d, J = 5.8 Hz, 1H), 8.71 (d, J = 8.4 Hz, 1H), 8.01 (t, J = 7.3 Hz, 1H), 7.91 (d, J = 3.3 Hz, 1H), 7.74 (d, J = 4.7 Hz, 1H), 7.15 (t, J = 4.2 Hz, 1H), 6.06 (d, J = 5.0 Hz, 1H), 4.53 (s, 1H), 4.43 (t, J = 4.9 Hz, 1H), 4.35 (t, J = 2.9 Hz, 3H), 4.23 (d, J = 10.9 Hz, 1H), 4.07 (d, J = 11.6 Hz, 1H). $^{13}$C NMR (150.9 MHz, $D_2O$) δ 163.1, 162.8 (q, J = 35.6 Hz, $CF_3$**C**$O_2^-$), 138.9, 137.2, 136.3, 135.1, 133.8, 131.8, 131.7, 128.6, 128.2, 116.3 (q, J = 291.6 Hz, **C**$F_3CO_2^-$), 99.7, 86.9 (d, J = 8.9 Hz), 77.8, 70.2, 64.2 (d, J = 5.0 Hz). $^{31}$P NMR (202.5 MHz, $D_2O$) δ -0.30. $^{19}$F NMR (470.6 MHz, $D_2O$) δ -75.62. HRMS (ESI) $[M]^+$ calculated for $C_{15}H_{18}N_2O_8PS^+$: 417.0522. Found: 417.0527.

**Synthesis of Gliocidin-adenine dinucleotide**

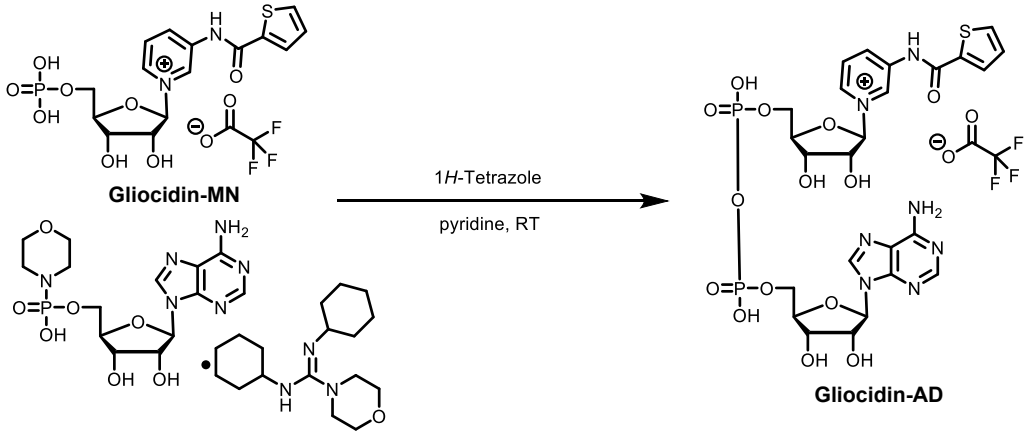


Gliocidin-MN (10.6 mg, 0.02 mmol) was co-evaporated with anhydrous pyridine (1 ml x 3) and then dissolved in 0.5 mL anhydrous pyridine under argon. Adenosine 5'-monophosphomorpholidate 4-morpholine-N,N'-dicyclohexylcarboxamidine salt (28 mg, 0,04 mmol) and 1H-tetrazole solution (0.4 mL, 0.18 mmol, 0.45M in acetonitrile) were added. The resulting mixture was concentrated to dryness and then treated with anhydrous pyridine (0.4 mL). The reaction mixture was stirred under argon at room temperature for 48 hours. The solvents were removed by

rotary evaporation. The residue was dissolved in 5 mL acetonitrile / water (1 / 1 with 0.05% TFA) and purified by prep HPLC (Column: XBridge Prep C18 5µm OBD, 19x150 mm; using the gradient: 5 to 20% acetonitrile (with 0.05% TFA) in water (with 0.05% TFA). The combined elution fractions were lyophilized, giving Gliocidin-AD (6.8 mg, 40% yield) as white foam. $^{1}$H NMR (600 MHz, $D_2O$) δ 9.29 (s, 1H), 8.90 (d, J = 8.0 Hz, 1H), 8.54 (d, J = 5.5 Hz, 1H), 8.37 (s, 1H), 8.20 (s, 1H), 7.90 (s, 1H), 7.75 (d, J = 2.2 Hz, 1H), 7.48 (s, 1H), 6.88 (s, 1H), 5.96 (d, J = 5.4 Hz, 1H), 5.86 (d, J = 4.4 Hz, 1H), 4.47 (s, 1H), 4.43 (t, J = 4.7 Hz, 1H), 4.39 (t, J = 5.1 Hz, 1H), 4.33 (t, J = 2.8 Hz, 1H), 4.28 (d, J = 11.8 Hz, 1H), 4.18 (t, J = 4.8 Hz, 1H), 4.11 (m, 3H), 4.02 (m, 1H).$^{13}$C NMR (150.9 MHz, $D_2O$) δ 162.9 (q, J = 35.6Hz, CF3**C**$O_2^-$), 162.7, 149.5, 147.8, 144.4, 142.4, 139.5, 136.8, 136.4, 135.4, 133.5, 131.6, 131.2, 128.5, 128.0, 118.4, 116.3 (q, J = 291.6 Hz, **C**$F_3CO_2^-$), 99.7, 88.5, 86.7 (d, J = 9.2 Hz), 83.7 (d, J = 8.7 Hz), 77.6, 74.6, 70.7, 69.6, 64.9, 64.7. $^{31}$P NMR (202.5 MHz, $D_2O$) δ -11.48. $^{19}$F NMR (470.6 MHz, $D_2O$) δ -75.61. HRMS (ESI) $[M]^+$ calculated for $C_{25}H_{30}N_7O_{14}P_2S^+$: 746.1047. Found: 746.1031.

**Statistical Analysis**

Statistical analysis for each experiment can be found in the corresponding figure legends. All statistical analyses were performed using GraphPad Prism 9. The error bars in all figures represent the standard deviation. The statistical significance of *in vitro* cell count studies was calculated using a two-tailed paired student's *t* test. For metabolomics and Gliocidin derivatives LC-MS/MS experiments, statistical analysis was performed using a two-tailed, unpaired student's *t* test. In

the case of *in vivo* samples, a non-parametric Mann-Whitney test was used to calculate statistical significance. *P* values less than 0.05 were considered statistically significant for all tests.

## Chapter 4 Conclusion and Future Perspectives

Glioblastoma remains as one of the most malignant tumors without optimal treatment options. Despite the large number of studies on GBM, much remains to be learned in terms of its biology and tumor vulnerability. In this thesis, we explored a potential novel cell of origin for GBM and investigated the mechanistic and preclinical efficacy of a novel drug that targets tumor metabolic vulnerability.

In chapter 2, we utilized the CGD transgene and investigated whether the $GFP^{low}SOX2^{+}$ cells in murine young adult basilar pons could give rise to GBM. Results showed that these cells are $OLIG2^{-}PDGFR\alpha^{+}$ and are extremely quiescent. Only upon supplying these cells with FGF and PDGF-AA *in vitro* does it activate the cells into proliferation, albeit with limited proliferative capacity. We further showed that most of the tumors generated from these cells showed high resemblance in terms of transcriptome with the already known OPC-originated type II tumors. Taken together, this is expected as $OLIG2^{-}PDGFR\alpha^{+}$ cells represent a quiescent OPC population, hence, they give rise to type II-like tumors.

In chapter 3, we investigated the MoA and preclinical efficacy of Gliocidin. Through conducting a genome-wide CRISPR-Cas9 screen, we elucidated its reliance on mTORC1 activity for drug sensitivity modulation. Furthermore, based on its nucleotide dependency switch to the salvage pathway as an alternative resistant mechanism, in addition to established studies on Mizoribine by the Manning group, we elucidated the MoA pathway of Gliocidin to be targeting the *de novo* guanylate synthesis pathway, specifically IMPDH2. We further demonstrated the Gliocidin is a prodrug and requires enzymes of the NAD+ salvage pathway for

activation. Specifically, the sensitivity of tumors to Gliocidin largely depends on the expression level of the rate-limiting enzyme NMNAT1. Finally, we demonstrated Gliocidin to have BBB penetrability, which enables it for drug development for treating various brain tumors, including GBM.

## Future Directions

### Investigating COP as a potential cell of origin

Despite having demonstrated that the majority of pontine-derived tumors are most likely originated from OPCs, it remains to be of biological interest to investigate the tumorigenic potential of COP. Moreover, this is not limited to GBM but pertains to other oligodendrocytic brain tumors as well. We would expect the COPs may have weaker tendency for tumor formation, mainly because it is differentiation committed. However, lower grade glioma such as oligodendroglioma and IDH-mutant astrocytomas. Of course, one also has to take the distinct genetic mutations induced into considerations. For example, single deletion or combination of the *Nf1* and *Trp53* could be tested in both COPs and OPCs for their tumorigenic potential.

### Searching for the mechanistic explanation for mesenchymal tumors

The advent of TCGA database for various tumors has contributed to enabling molecular subtyping based on genomic, mutation and expression profiles. Molecular subtyping has stratified GBM into classical, proneural and mesenchymal (Q. Wang et al., 2017). In murine GBMs derived from GEMMs, we have

established that GBM can be stratified, based on their cell of origins, into type I and II tumors. The expression profiles of classical and proneural highly resembles that of type I and II, respectively. However, mouse modeling with GBM relevant mutations has not been successful for mesenchymal GBM.

From our RNA-sequencing data of both tumor tissues and tumor cells derived from over 40 different independent murine GBMs, we have demonstrated that a mesenchymal-like GBM could be generated using the exact same mutations (*NPP*) from the same cell of origin. This begs the question on the mechanistic explanation for mesenchymal tumor formation. We currently favor the theory that mesenchymal tumors may acquire additional injury or mutation along its tumorigenesis process, which propels it to develop into a tumor that attracts immune infiltrates. Developing a reliable mesenchymal tumor also will assist in the study of potential immunotherapies using mouse models. It is important to mention that up until now, most mouse GBM studies investigating immunotherapeutic potential utilized the infamous cell line GL-261. GL-261 is not an ideal GBM model as it was generated through injection of methylchloranthrene pellets into the brain of C57BL/6 mice, a method that has no relevance to primary GBM developed in the general human population. It harbors more than 5000 mutations, which explains its high sensitivity to immunotherapy. However, the number of mutations of GBM patients usually are within 100 prior to surgical resection and treatment.

Mesenchymal GBM, given its observation to have high tumor immune cell infiltrate, has been a candidate tumor for immunotherapy. However, a proper GBM model must be established in order to perform accurate and correct

immunotherapy studies. According to GBM TCGA datasets, *Nf1* and *Trp53* mutations co-occurs with statistical significance. This supports the use of our type I and II *NPP* GBM lines as models for testing GBM in an immunocompetent setting. Moreover, to establish recurrent GBM models, mice bearing type I or II tumors orthotopically could undergo Temozolomide and radiation treatment. These tumor models could then utilized as recurrent GBM models for testing immunotherapy in an immunocompetent setting.

**Developing Gliocidin as a tumor-agnostic drug**

The fact that Gliocidin heavily depends on the expression level of its activation enzyme, NMNAT1, provides the rationale that careful patient selection criteria must be employed if the drug ever enters clinical trial. This property deems that only patients with high tumor expression of NMNATs be suitable for treatment, while low expression patients should be excluded.

On the other hand, the correlation of NMNAT expression could allow Gliocidin to also be used in other tumor types with high NMNAT expression. For example, according to TCGA, 12% of all ovarian tumors have amplification of either Nmnat1, 2 or 3. Thus, to successfully develop Gliocidin, it is recommened to assume the role of a tumor agnostic drug, drugs based on the cancer specific genes or protein changes, regardless of the tissue type.

**Furthering the study of NMNAT1 regulation**

Studies of *Nmnat1* primarily revolves around its neuroprotective role in the retina and other neurological related disease models. In terms of its molecular biology, it has been previously shown that the expression of NMNAT1 increases as tumor cells are exposed to DNA damaging agents (Kiss et al., 2020). Moreover, knocking out *Nmnat1* hypersensitizes tumor cells to chemotherapeutic DNA-crosslinking agents cisplatin and doxorubicin, further illustrating its importance in inducing DNA damage response. This may partially explain the increase in *Nmnat1* expression upon Temozolomide treatment in our study. However, to improve *in vivo* tumor response to Gliocidin, it is crucial to study the expressional regulation of *Nmnat1*.

An interesting result we came across while studying *Nmnat1* is its strong correlation with the *de novo* nucleotide synthesis pathway. By using the database of DepMap (https://depmap.org/portal/), which includes genome-wide CRISPR-Cas9 screens done across 1095 different cancer cell lines (DepMap Public version 23Q2), we probed for *Nmnat1* and searched for its co-essentiality genes. Co-essentiality analysis revealed genes that are participating in the same biological pathway based on their essentiality across multiple CRISPR screens (Wainberg et al., 2021). Based on the co-essential genes provided on DepMap for *Nmnat1*, almost all genes encode metabolic enzymes and are heavily enriched for *de novo* purine (ie. *Ppat*, *Gart*, *Adsl*, *Paics*, *Atic*, *Pfas* and *Impdh2*) and pyrimidine (ie. *Dhodh*, *Cad* and *Umps*) synthesis enzymes. Thus, this implied that *Nmnat1* is essential for *de novo* nucleotide synthesis. It is also of biological interest to

understand the distinction between *Nmnat1* with *Nmnat2* or *3* in terms of its role in the *de novo* nucleotide synthesis pathway.

## References


Ahn, S., & Joyner, A. L. (2005). In vivo analysis of quiescent adult neural stem cells responding to Sonic hedgehog. *Nature*, *437*(7060), 894-897. https://doi.org/10.1038/nature03994

Aibar, S., Gonzalez-Blas, C. B., Moerman, T., Huynh-Thu, V. A., Imrichova, H., Hulselmans, G., Rambow, F., Marine, J. C., Geurts, P., Aerts, J., van den Oord, J., Atak, Z. K., Wouters, J., & Aerts, S. (2017). SCENIC: single-cell regulatory network inference and clustering. *Nat Methods*, *14*(11), 1083-1086. https://doi.org/10.1038/nmeth.4463

Alcantara Llaguno, S., Chen, J., Kwon, C. H., Jackson, E. L., Li, Y., Burns, D. K., Alvarez-Buylla, A., & Parada, L. F. (2009). Malignant astrocytomas originate from neural stem/progenitor cells in a somatic tumor suppressor mouse model. *Cancer Cell*, *15*(1), 45-56. https://doi.org/10.1016/j.ccr.2008.12.006

Alcantara Llaguno, S., Sun, D., Pedraza, A. M., Vera, E., Wang, Z., Burns, D. K., & Parada, L. F. (2019). Cell-of-origin susceptibility to glioblastoma formation declines with neural lineage restriction. *Nat Neurosci*, *22*(4), 545-555. https://doi.org/10.1038/s41593-018-0333-8

Alcantara Llaguno, S. R., Wang, Z., Sun, D., Chen, J., Xu, J., Kim, E., Hatanpaa, K. J., Raisanen, J. M., Burns, D. K., Johnson, J. E., & Parada, L. F. (2015). Adult Lineage-Restricted CNS Progenitors Specify Distinct Glioblastoma Subtypes. *Cancer Cell*, *28*(4), 429-440. https://doi.org/10.1016/j.ccell.2015.09.007

Alquicira-Hernandez, J., & Powell, J. E. (2021). Nebulosa recovers single-cell gene expression signals by kernel density estimation. *Bioinformatics*, *37*(16), 2485-2487. https://doi.org/10.1093/bioinformatics/btab003

Azizi, E., Carr, A. J., Plitas, G., Cornish, A. E., Konopacki, C., Prabhakaran, S., Nainys, J., Wu, K., Kiseliovas, V., Setty, M., Choi, K., Fromme, R. M., Dao, P., McKenney, P. T., Wasti, R. C., Kadaveru, K., Mazutis, L., Rudensky, A. Y., & Pe'er, D. (2018). Single-Cell Map of Diverse Immune Phenotypes in the Breast Tumor Microenvironment. *Cell*, *174*(5), 1293-1308 e1236. https://doi.org/10.1016/j.cell.2018.05.060

Benner, E. J., Luciano, D., Jo, R., Abdi, K., Paez-Gonzalez, P., Sheng, H., Warner, D. S., Liu, C., Eroglu, C., & Kuo, C. T. (2013). Protective astrogenesis from the SVZ niche after injury is controlled by Notch modulator Thbs4. *Nature*, *497*(7449), 369-373. https://doi.org/10.1038/nature12069

Bester, A. C., Roniger, M., Oren, Y. S., Im, M. M., Sarni, D., Chaoat, M., Bensimon, A., Zamir, G., Shewach, D. S., & Kerem, B. (2011). Nucleotide deficiency promotes genomic instability in early stages of cancer development. *Cell*, *145*(3), 435-446. https://doi.org/10.1016/j.cell.2011.03.044

Bieganowski, P., & Brenner, C. (2004). Discoveries of nicotinamide riboside as a nutrient and conserved NRK genes establish a Preiss-Handler independent route to NAD+ in fungi and humans. *Cell*, *117*(4), 495-502. https://doi.org/10.1016/s0092-8674(04)00416-7

Bollenbach, M., Aquino, P. G. V., de Araujo-Junior, J. X., Bourguignon, J. J., Bihel, F., Salome, C., Wagner, P., & Schmitt, M. (2017). Efficient and Mild Ullmann-Type N-Arylation of Amides, Carbamates, and Azoles in Water. *Chemistry*, *23*(55), 13676-13683. https://doi.org/10.1002/chem.201700832

Brennan, C. W., Verhaak, R. G., McKenna, A., Campos, B., Noushmehr, H., Salama, S. R., Zheng, S., Chakravarty, D., Sanborn, J. Z., Berman, S. H., Beroukhim, R., Bernard, B., Wu, C. J., Genovese, G., Shmulevich, I., Barnholtz-Sloan, J., Zou, L., Vegesna, R., Shukla, S. A., . . . Network, T. R. (2013). The somatic genomic landscape of glioblastoma. *Cell*, *155*(2), 462-477. https://doi.org/10.1016/j.cell.2013.09.034

Brown, A. J. (2009). 24(S),25-epoxycholesterol: a messenger for cholesterol homeostasis. *Int J Biochem Cell Biol*, *41*(4), 744-747. https://doi.org/10.1016/j.biocel.2008.05.029

Buffo, A., Vosko, M. R., Erturk, D., Hamann, G. F., Jucker, M., Rowitch, D., & Gotz, M. (2005). Expression pattern of the transcription factor Olig2 in response to brain injuries: implications for neuronal repair. *Proc Natl Acad Sci U S A*, *102*(50), 18183-18188. https://doi.org/10.1073/pnas.0506535102

Butler, A., Hoffman, P., Smibert, P., Papalexi, E., & Satija, R. (2018). Integrating single-cell transcriptomic data across different conditions, technologies, and species. *Nat Biotechnol*, *36*(5), 411-420. https://doi.org/10.1038/nbt.4096

Cancer Genome Atlas Research, N. (2008). Comprehensive genomic characterization defines human glioblastoma genes and core pathways. *Nature*, *455*(7216), 1061-1068. https://doi.org/10.1038/nature07385

Casper, K. B., Jones, K., & McCarthy, K. D. (2007). Characterization of astrocyte-specific conditional knockouts. *Genesis*, *45*(5), 292-299. https://doi.org/10.1002/dvg.20287

Chambers, M. C., Maclean, B., Burke, R., Amodei, D., Ruderman, D. L., Neumann, S., Gatto, L., Fischer, B., Pratt, B., Egertson, J., Hoff, K., Kessner, D., Tasman, N., Shulman, N., Frewen, B., Baker, T. A., Brusniak, M. Y., Paulse, C., Creasy, D., . . . Mallick, P. (2012). A cross-platform toolkit for mass spectrometry and proteomics. *Nat Biotechnol*, *30*(10), 918-920. https://doi.org/10.1038/nbt.2377

Chau, V., Lim, S. K., Mo, W., Liu, C., Patel, A. J., McKay, R. M., Wei, S., Posner, B. A., De Brabander, J. K., Williams, N. S., Parada, L. F., & Le, L. Q. (2014). Preclinical therapeutic efficacy of a novel pharmacologic inducer of apoptosis in malignant peripheral nerve sheath tumors. *Cancer Res*, *74*(2), 586-597. https://doi.org/10.1158/0008-5472.CAN-13-1934

Chen, J., Kwon, C. H., Lin, L., Li, Y., & Parada, L. F. (2009). Inducible site-specific recombination in neural stem/progenitor cells. *Genesis*, *47*(2), 122-131. https://doi.org/10.1002/dvg.20465

Chen, J., Li, Y., Yu, T. S., McKay, R. M., Burns, D. K., Kernie, S. G., & Parada, L. F. (2012). A restricted cell population propagates glioblastoma growth after chemotherapy. *Nature*, *488*(7412), 522-526. https://doi.org/10.1038/nature11287

Chinot, O. L., Wick, W., Mason, W., Henriksson, R., Saran, F., Nishikawa, R., Carpentier, A. F., Hoang-Xuan, K., Kavan, P., Cernea, D., Brandes, A. A., Hilton, M., Abrey, L., & Cloughesy, T. (2014). Bevacizumab plus radiotherapy-temozolomide for newly

diagnosed glioblastoma. *N Engl J Med*, *370*(8), 709-722. https://doi.org/10.1056/NEJMoa1308345

Chow, L. M., Endersby, R., Zhu, X., Rankin, S., Qu, C., Zhang, J., Broniscer, A., Ellison, D. W., & Baker, S. J. (2011). Cooperativity within and among Pten, p53, and Rb pathways induces high-grade astrocytoma in adult brain. *Cancer Cell*, *19*(3), 305-316. https://doi.org/10.1016/j.ccr.2011.01.039

Clevers, H. (2011). The cancer stem cell: premises, promises and challenges. *Nat Med*, *17*(3), 313-319. https://doi.org/10.1038/nm.2304

Codega, P., Silva-Vargas, V., Paul, A., Maldonado-Soto, A. R., Deleo, A. M., Pastrana, E., & Doetsch, F. (2014). Prospective identification and purification of quiescent adult neural stem cells from their in vivo niche. *Neuron*, *82*(3), 545-559. https://doi.org/10.1016/j.neuron.2014.02.039

Cooney, D. A., Jayaram, H. N., Glazer, R. I., Kelley, J. A., Marquez, V. E., Gebeyehu, G., Van Cott, A. C., Zwelling, L. A., & Johns, D. G. (1983). Studies on the mechanism of action of tiazofurin metabolism to an analog of NAD with potent IMP dehydrogenase-inhibitory activity. *Adv Enzyme Regul*, *21*, 271-303. https://doi.org/10.1016/0065-2571(83)90019-5

deCarvalho, A. C., Kim, H., Poisson, L. M., Winn, M. E., Mueller, C., Cherba, D., Koeman, J., Seth, S., Protopopov, A., Felicella, M., Zheng, S., Multani, A., Jiang, Y., Zhang, J., Nam, D. H., Petricoin, E. F., Chin, L., Mikkelsen, T., & Verhaak, R. G. W. (2018). Discordant inheritance of chromosomal and extrachromosomal DNA elements contributes to dynamic disease evolution in glioblastoma. *Nat Genet*, *50*(5), 708-717. https://doi.org/10.1038/s41588-018-0105-0

Doench, J. G., Fusi, N., Sullender, M., Hegde, M., Vaimberg, E. W., Donovan, K. F., Smith, I., Tothova, Z., Wilen, C., Orchard, R., Virgin, H. W., Listgarten, J., & Root, D. E. (2016). Optimized sgRNA design to maximize activity and minimize off-target effects of CRISPR-Cas9. *Nat Biotechnol*, *34*(2), 184-191. https://doi.org/10.1038/nbt.3437

Doetsch, F., Caille, I., Lim, D. A., Garcia-Verdugo, J. M., & Alvarez-Buylla, A. (1999). Subventricular zone astrocytes are neural stem cells in the adult mammalian brain. *Cell*, *97*(6), 703-716. https://doi.org/10.1016/s0092-8674(00)80783-7

Doetsch, F., Petreanu, L., Caille, I., Garcia-Verdugo, J. M., & Alvarez-Buylla, A. (2002). EGF converts transit-amplifying neurogenic precursors in the adult brain into multipotent stem cells. *Neuron*, *36*(6), 1021-1034. https://doi.org/10.1016/s0896-6273(02)01133-9

Esteller, M., Garcia-Foncillas, J., Andion, E., Goodman, S. N., Hidalgo, O. F., Vanaclocha, V., Baylin, S. B., & Herman, J. G. (2000). Inactivation of the DNA-repair gene MGMT and the clinical response of gliomas to alkylating agents. *N Engl J Med*, *343*(19), 1350-1354. https://doi.org/10.1056/NEJM200011093431901

Fang, L. P., Liu, Q., Meyer, E., Welle, A., Huang, W., Scheller, A., Kirchhoff, F., & Bai, X. (2023). A subset of OPCs do not express Olig2 during development which can be increased in the adult by brain injuries and complex motor learning. *Glia*, *71*(2), 415-430. https://doi.org/10.1002/glia.24284

Galvao, R. P., Kasina, A., McNeill, R. S., Harbin, J. E., Foreman, O., Verhaak, R. G., Nishiyama, A., Miller, C. R., & Zong, H. (2014). Transformation of quiescent adult oligodendrocyte precursor cells into malignant glioma through a multistep reactivation process. *Proc Natl Acad Sci U S A*, *111*(40), E4214-4223. https://doi.org/10.1073/pnas.1414389111

Gonzalez, P. P., Kim, J., Galvao, R. P., Cruickshanks, N., Abounader, R., & Zong, H. (2018). p53 and NF 1 loss plays distinct but complementary roles in glioma initiation and progression. *Glia*, *66*(5), 999-1015. https://doi.org/10.1002/glia.23297

Groszer, M., Erickson, R., Scripture-Adams, D. D., Lesche, R., Trumpp, A., Zack, J. A., Kornblum, H. I., Liu, X., & Wu, H. (2001). Negative regulation of neural stem/progenitor cell proliferation by the Pten tumor suppressor gene in vivo. *Science*, *294*(5549), 2186-2189. https://doi.org/10.1126/science.1065518

Guo, X., Yang, X., Wu, J., Yang, H., Li, Y., Li, J., Liu, Q., Wu, C., Xing, H., Liu, P., Wang, Y., Hu, C., & Ma, W. (2022). Tumor-Treating Fields in Glioblastomas: Past, Present, and Future. *Cancers (Basel)*, *14*(15). https://doi.org/10.3390/cancers14153669

Gwynne, W. D., Suk, Y., Custers, S., Mikolajewicz, N., Chan, J. K., Zador, Z., Chafe, S. C., Zhai, K., Escudero, L., Zhang, C., Zaslaver, O., Chokshi, C., Shaikh, M. V., Bakhshinyan, D., Burns, I., Chaudhry, I., Nachmani, O., Mobilio, D., Maich, W. T., . . . Singh, S. K. (2022). Cancer-selective metabolic vulnerabilities in MYC-amplified medulloblastoma. *Cancer Cell*, *40*(12), 1488-1502 e1487. https://doi.org/10.1016/j.ccell.2022.10.009

Haque, A., Engel, J., Teichmann, S. A., & Lonnberg, T. (2017). A practical guide to single-cell RNA-sequencing for biomedical research and clinical applications. *Genome Med*, *9*(1), 75. https://doi.org/10.1186/s13073-017-0467-4

Hara, T., Chanoch-Myers, R., Mathewson, N. D., Myskiw, C., Atta, L., Bussema, L., Eichhorn, S. W., Greenwald, A. C., Kinker, G. S., Rodman, C., Gonzalez Castro, L. N., Wakimoto, H., Rozenblatt-Rosen, O., Zhuang, X., Fan, J., Hunter, T., Verma, I. M., Wucherpfennig, K. W., Regev, A., . . . Tirosh, I. (2021). Interactions between cancer cells and immune cells drive transitions to mesenchymal-like states in glioblastoma. *Cancer Cell*, *39*(6), 779-792 e711. https://doi.org/10.1016/j.ccell.2021.05.002

Ikawa, T., Barder, T. E., Biscoe, M. R., & Buchwald, S. L. (2007). Pd-catalyzed amidation of aryl chlorides using monodentate biaryl phosphine ligands: a kinetic, computational, and synthetic investigation. *J Am Chem Soc*, *129*(43), 13001-13007. https://doi.org/10.1021/ja0717414

Ishiwata, T., Teduka, K., Yamamoto, T., Kawahara, K., Matsuda, Y., & Naito, Z. (2011). Neuroepithelial stem cell marker nestin regulates the migration, invasion and growth of human gliomas. *Oncol Rep*, *26*(1), 91-99. https://doi.org/10.3892/or.2011.1267

Jacques, T. S., Swales, A., Brzozowski, M. J., Henriquez, N. V., Linehan, J. M., Mirzadeh, Z., C, O. M., Naumann, H., Alvarez-Buylla, A., & Brandner, S. (2010). Combinations of genetic mutations in the adult neural stem cell compartment determine brain tumour phenotypes. *EMBO J*, *29*(1), 222-235. https://doi.org/10.1038/emboj.2009.327

Johansson, C. B., Momma, S., Clarke, D. L., Risling, M., Lendahl, U., & Frisen, J. (1999). Identification of a neural stem cell in the adult mammalian central nervous system. *Cell*, *96*(1), 25-34. https://doi.org/10.1016/s0092-8674(00)80956-3

Kagawa, T., Mekada, E., Shishido, Y., & Ikenaka, K. (1997). Immune system-related CD9 is expressed in mouse central nervous system myelin at a very late stage of myelination. *J Neurosci Res*, *50*(2), 312-320. https://doi.org/10.1002/(SICI)1097-4547(19971015)50:2<312::AID-JNR19>3.0.CO;2-9

Kim, E. J., Leung, C. T., Reed, R. R., & Johnson, J. E. (2007). In vivo analysis of Ascl1 defined progenitors reveals distinct developmental dynamics during adult neurogenesis and gliogenesis. *J Neurosci*, *27*(47), 12764-12774. https://doi.org/10.1523/JNEUROSCI.3178-07.2007

Kiss, A., Raduly, A. P., Regdon, Z., Polgar, Z., Tarapcsak, S., Sturniolo, I., El-Hamoly, T., Virag, L., & Hegedus, C. (2020). Targeting Nuclear NAD(+) Synthesis Inhibits DNA Repair, Impairs Metabolic Adaptation and Increases Chemosensitivity of U-2OS Osteosarcoma Cells. *Cancers (Basel)*, *12*(5). https://doi.org/10.3390/cancers12051180

Kofuji, S., Hirayama, A., Eberhardt, A. O., Kawaguchi, R., Sugiura, Y., Sampetrean, O., Ikeda, Y., Warren, M., Sakamoto, N., Kitahara, S., Yoshino, H., Yamashita, D., Sumita, K., Wolfe, K., Lange, L., Ikeda, S., Shimada, H., Minami, N., Malhotra, A., . . . Sasaki, A. T. (2019). IMP dehydrogenase-2 drives aberrant nucleolar activity and promotes tumorigenesis in glioblastoma. *Nat Cell Biol*, *21*(8), 1003-1014. https://doi.org/10.1038/s41556-019-0363-9

Kwon, C. H., Zhao, D., Chen, J., Alcantara, S., Li, Y., Burns, D. K., Mason, R. P., Lee, E. Y., Wu, H., & Parada, L. F. (2008). Pten haploinsufficiency accelerates formation of high-grade astrocytomas. *Cancer Res*, *68*(9), 3286-3294. https://doi.org/10.1158/0008-5472.CAN-07-6867

Kwon, Y. (2001). Handbook of Essential Pharmacokinetics, Pharmacodynamics and Drug Metabolism for Industrial Scientists. In *Handbook of Essential Pharmacokinetics, Pharmacodynamics and Drug Metabolism for Industrial Scientists* (pp. 231-232). Springer New York, NY. https://doi.org/https://doi.org/10.1007/b112416

Lagace, D. C., Whitman, M. C., Noonan, M. A., Ables, J. L., DeCarolis, N. A., Arguello, A. A., Donovan, M. H., Fischer, S. J., Farnbauch, L. A., Beech, R. D., DiLeone, R. J., Greer, C. A., Mandyam, C. D., & Eisch, A. J. (2007). Dynamic contribution of nestin-expressing stem cells to adult neurogenesis. *J Neurosci*, *27*(46), 12623-12629. https://doi.org/10.1523/JNEUROSCI.3812-07.2007

Lampert, F., Stafa, D., Goga, A., Soste, M. V., Gilberto, S., Olieric, N., Picotti, P., Stoffel, M., & Peter, M. (2018). The multi-subunit GID/CTLH E3 ubiquitin ligase promotes cell proliferation and targets the transcription factor Hbp1 for degradation. *Elife*, *7*. https://doi.org/10.7554/eLife.35528

Lendahl, U., Zimmerman, L. B., & McKay, R. D. (1990). CNS stem cells express a new class of intermediate filament protein. *Cell*, *60*(4), 585-595. https://doi.org/10.1016/0092-8674(90)90662-x

Ligon, K. L., Kesari, S., Kitada, M., Sun, T., Arnett, H. A., Alberta, J. A., Anderson, D. J., Stiles, C. D., & Rowitch, D. H. (2006). Development of NG2 neural progenitor cells

requires Olig gene function. *Proc Natl Acad Sci U S A*, *103*(20), 7853-7858. https://doi.org/10.1073/pnas.0511001103

Lim, M., Weller, M., Idbaih, A., Steinbach, J., Finocchiaro, G., Raval, R. R., Ansstas, G., Baehring, J., Taylor, J. W., Honnorat, J., Petrecca, K., De Vos, F., Wick, A., Sumrall, A., Sahebjam, S., Mellinghoff, I. K., Kinoshita, M., Roberts, M., Slepetis, R., . . . Omuro, A. (2022). Phase III trial of chemoradiotherapy with temozolomide plus nivolumab or placebo for newly diagnosed glioblastoma with methylated MGMT promoter. *Neuro Oncol*, *24*(11), 1935-1949. https://doi.org/10.1093/neuonc/noac116

Lin, S. C., Lee, K. F., Nikitin, A. Y., Hilsenbeck, S. G., Cardiff, R. D., Li, A., Kang, K. W., Frank, S. A., Lee, W. H., & Lee, E. Y. (2004). Somatic mutation of p53 leads to estrogen receptor alpha-positive and -negative mouse mammary tumors with high frequency of metastasis. *Cancer Res*, *64*(10), 3525-3532. https://doi.org/10.1158/0008-5472.CAN-03-3524

Liu, C., Sage, J. C., Miller, M. R., Verhaak, R. G., Hippenmeyer, S., Vogel, H., Foreman, O., Bronson, R. T., Nishiyama, A., Luo, L., & Zong, H. (2011). Mosaic analysis with double markers reveals tumor cell of origin in glioma. *Cell*, *146*(2), 209-221. https://doi.org/10.1016/j.cell.2011.06.014

Louis, D. N., Perry, A., Reifenberger, G., von Deimling, A., Figarella-Branger, D., Cavenee, W. K., Ohgaki, H., Wiestler, O. D., Kleihues, P., & Ellison, D. W. (2016). The 2016 World Health Organization Classification of Tumors of the Central Nervous System: a summary. *Acta Neuropathol*, *131*(6), 803-820. https://doi.org/10.1007/s00401-016-1545-1

Louis, D. N., Perry, A., Wesseling, P., Brat, D. J., Cree, I. A., Figarella-Branger, D., Hawkins, C., Ng, H. K., Pfister, S. M., Reifenberger, G., Soffietti, R., von Deimling, A., & Ellison, D. W. (2021). The 2021 WHO Classification of Tumors of the Central Nervous System: a summary. *Neuro Oncol*, *23*(8), 1231-1251. https://doi.org/10.1093/neuonc/noab106

Marques, S., van Bruggen, D., Vanichkina, D. P., Floriddia, E. M., Munguba, H., Varemo, L., Giacomello, S., Falcao, A. M., Meijer, M., Bjorklund, A. K., Hjerling-Leffler, J., Taft, R. J., & Castelo-Branco, G. (2018). Transcriptional Convergence of Oligodendrocyte Lineage Progenitors during Development. *Dev Cell*, *46*(4), 504-517 e507. https://doi.org/10.1016/j.devcel.2018.07.005

Marques, S., Zeisel, A., Codeluppi, S., van Bruggen, D., Mendanha Falcao, A., Xiao, L., Li, H., Haring, M., Hochgerner, H., Romanov, R. A., Gyllborg, D., Munoz Manchado, A., La Manno, G., Lonnerberg, P., Floriddia, E. M., Rezayee, F., Ernfors, P., Arenas, E., Hjerling-Leffler, J., . . . Castelo-Branco, G. (2016). Oligodendrocyte heterogeneity in the mouse juvenile and adult central nervous system. *Science*, *352*(6291), 1326-1329. https://doi.org/10.1126/science.aaf6463

Menn, B., Garcia-Verdugo, J. M., Yaschine, C., Gonzalez-Perez, O., Rowitch, D., & Alvarez-Buylla, A. (2006). Origin of oligodendrocytes in the subventricular zone of the adult brain. *J Neurosci*, *26*(30), 7907-7918. https://doi.org/10.1523/JNEUROSCI.1299-06.2006

Mignone, J. L., Kukekov, V., Chiang, A. S., Steindler, D., & Enikolopov, G. (2004). Neural stem and progenitor cells in nestin-GFP transgenic mice. *J Comp Neurol*, *469*(3), 311-324. https://doi.org/10.1002/cne.10964

Mohseni, P., Sung, H. K., Murphy, A. J., Laliberte, C. L., Pallari, H. M., Henkelman, M., Georgiou, J., Xie, G., Quaggin, S. E., Thorner, P. S., Eriksson, J. E., & Nagy, A. (2011). Nestin is not essential for development of the CNS but required for dispersion of acetylcholine receptor clusters at the area of neuromuscular junctions. *J Neurosci*, *31*(32), 11547-11552. https://doi.org/10.1523/JNEUROSCI.4396-10.2011

Morshead, C. M., Reynolds, B. A., Craig, C. G., McBurney, M. W., Staines, W. A., Morassutti, D., Weiss, S., & van der Kooy, D. (1994). Neural stem cells in the adult mammalian forebrain: a relatively quiescent subpopulation of subependymal cells. *Neuron*, *13*(5), 1071-1082. https://doi.org/10.1016/0896-6273(94)90046-9

Naffouje, R., Grover, P., Yu, H., Sendilnathan, A., Wolfe, K., Majd, N., Smith, E. P., Takeuchi, K., Senda, T., Kofuji, S., & Sasaki, A. T. (2019). Anti-Tumor Potential of IMP Dehydrogenase Inhibitors: A Century-Long Story. *Cancers (Basel)*, *11*(9). https://doi.org/10.3390/cancers11091346

Nait-Oumesmar, B., Decker, L., Lachapelle, F., Avellana-Adalid, V., Bachelin, C., & Baron-Van Evercooren, A. (1999). Progenitor cells of the adult mouse subventricular zone proliferate, migrate and differentiate into oligodendrocytes after demyelination. *Eur J Neurosci*, *11*(12), 4357-4366. https://doi.org/10.1046/j.1460-9568.1999.00873.x

Navarrete-Perea, J., Yu, Q., Gygi, S. P., & Paulo, J. A. (2018). Streamlined Tandem Mass Tag (SL-TMT) Protocol: An Efficient Strategy for Quantitative (Phospho)proteome Profiling Using Tandem Mass Tag-Synchronous Precursor Selection-MS3. *J Proteome Res*, *17*(6), 2226-2236. https://doi.org/10.1021/acs.jproteome.8b00217

Neftel, C., Laffy, J., Filbin, M. G., Hara, T., Shore, M. E., Rahme, G. J., Richman, A. R., Silverbush, D., Shaw, M. L., Hebert, C. M., Dewitt, J., Gritsch, S., Perez, E. M., Gonzalez Castro, L. N., Lan, X., Druck, N., Rodman, C., Dionne, D., Kaplan, A., . . . Suva, M. L. (2019). An Integrative Model of Cellular States, Plasticity, and Genetics for Glioblastoma. *Cell*, *178*(4), 835-849 e821. https://doi.org/10.1016/j.cell.2019.06.024

Omuro, A., Brandes, A. A., Carpentier, A. F., Idbaih, A., Reardon, D. A., Cloughesy, T., Sumrall, A., Baehring, J., van den Bent, M., Bahr, O., Lombardi, G., Mulholland, P., Tabatabai, G., Lassen, U., Sepulveda, J. M., Khasraw, M., Vauleon, E., Muragaki, Y., Di Giacomo, A. M., . . . Weller, M. (2023). Radiotherapy combined with nivolumab or temozolomide for newly diagnosed glioblastoma with unmethylated MGMT promoter: An international randomized phase III trial. *Neuro Oncol*, *25*(1), 123-134. https://doi.org/10.1093/neuonc/noac099

Pal, S., Kaplan, J. P., Nguyen, H., Stopka, S. A., Savani, M. R., Regan, M. S., Nguyen, Q. D., Jones, K. L., Moreau, L. A., Peng, J., Dipiazza, M. G., Perciaccante, A. J., Zhu, X., Hunsel, B. R., Liu, K. X., Alexandrescu, S., Drissi, R., Filbin, M. G., McBrayer, S.

K., . . . Haas-Kogan, D. A. (2022). A druggable addiction to de novo pyrimidine biosynthesis in diffuse midline glioma. *Cancer Cell*, *40*(9), 957-972 e910. https://doi.org/10.1016/j.ccell.2022.07.012

Palmer, T. D., Takahashi, J., & Gage, F. H. (1997). The adult rat hippocampus contains primordial neural stem cells. *Mol Cell Neurosci*, *8*(6), 389-404. https://doi.org/10.1006/mcne.1996.0595

Patel, A. P., Tirosh, I., Trombetta, J. J., Shalek, A. K., Gillespie, S. M., Wakimoto, H., Cahill, D. P., Nahed, B. V., Curry, W. T., Martuza, R. L., Louis, D. N., Rozenblatt-Rosen, O., Suva, M. L., Regev, A., & Bernstein, B. E. (2014). Single-cell RNA-seq highlights intratumoral heterogeneity in primary glioblastoma. *Science*, *344*(6190), 1396-1401. https://doi.org/10.1126/science.1254257

Persson, A. I., Petritsch, C., Swartling, F. J., Itsara, M., Sim, F. J., Auvergne, R., Goldenberg, D. D., Vandenberg, S. R., Nguyen, K. N., Yakovenko, S., Ayers-Ringler, J., Nishiyama, A., Stallcup, W. B., Berger, M. S., Bergers, G., McKnight, T. R., Goldman, S. A., & Weiss, W. A. (2010). Non-stem cell origin for oligodendroglioma. *Cancer Cell*, *18*(6), 669-682. https://doi.org/10.1016/j.ccr.2010.10.033

Picard-Riera, N., Decker, L., Delarasse, C., Goude, K., Nait-Oumesmar, B., Liblau, R., Pham-Dinh, D., & Baron-Van Evercooren, A. (2002). Experimental autoimmune encephalomyelitis mobilizes neural progenitors from the subventricular zone to undergo oligodendrogenesis in adult mice. *Proc Natl Acad Sci U S A*, *99*(20), 13211-13216. https://doi.org/10.1073/pnas.192314199

Pluskal, T., Castillo, S., Villar-Briones, A., & Oresic, M. (2010). MZmine 2: modular framework for processing, visualizing, and analyzing mass spectrometry-based molecular profile data. *BMC Bioinformatics*, *11*, 395. https://doi.org/10.1186/1471-2105-11-395

Ponti, G., Obernier, K., & Alvarez-Buylla, A. (2013). Lineage progression from stem cells to new neurons in the adult brain ventricular-subventricular zone. *Cell Cycle*, *12*(11), 1649-1650. https://doi.org/10.4161/cc.24984

Rappsilber, J., Mann, M., & Ishihama, Y. (2007). Protocol for micro-purification, enrichment, pre-fractionation and storage of peptides for proteomics using StageTips. *Nat Protoc*, *2*(8), 1896-1906. https://doi.org/10.1038/nprot.2007.261

Reardon, D. A., Brandes, A. A., Omuro, A., Mulholland, P., Lim, M., Wick, A., Baehring, J., Ahluwalia, M. S., Roth, P., Bahr, O., Phuphanich, S., Sepulveda, J. M., De Souza, P., Sahebjam, S., Carleton, M., Tatsuoka, K., Taitt, C., Zwirtes, R., Sampson, J., & Weller, M. (2020). Effect of Nivolumab vs Bevacizumab in Patients With Recurrent Glioblastoma: The CheckMate 143 Phase 3 Randomized Clinical Trial. *JAMA Oncol*, *6*(7), 1003-1010. https://doi.org/10.1001/jamaoncol.2020.1024

Regelmann, J., Schule, T., Josupeit, F. S., Horak, J., Rose, M., Entian, K. D., Thumm, M., & Wolf, D. H. (2003). Catabolite degradation of fructose-1,6-bisphosphatase in the yeast Saccharomyces cerevisiae: a genome-wide screen identifies eight novel GID genes and indicates the existence of two degradation pathways. *Mol Biol Cell*, *14*(4), 1652-1663. https://doi.org/10.1091/mbc.e02-08-0456

Reilly, K. M., Loisel, D. A., Bronson, R. T., McLaughlin, M. E., & Jacks, T. (2000). Nf1;Trp53 mutant mice develop glioblastoma with evidence of strain-specific effects. *Nat Genet*, *26*(1), 109-113. https://doi.org/10.1038/79075

Reya, T., Morrison, S. J., Clarke, M. F., & Weissman, I. L. (2001). Stem cells, cancer, and cancer stem cells. *Nature*, *414*(6859), 105-111. https://doi.org/10.1038/35102167

Reynolds, B. A., & Weiss, S. (1992). Generation of neurons and astrocytes from isolated cells of the adult mammalian central nervous system. *Science*, *255*(5052), 1707-1710. https://doi.org/10.1126/science.1553558

Santt, O., Pfirrmann, T., Braun, B., Juretschke, J., Kimmig, P., Scheel, H., Hofmann, K., Thumm, M., & Wolf, D. H. (2008). The yeast GID complex, a novel ubiquitin ligase (E3) involved in the regulation of carbohydrate metabolism. *Mol Biol Cell*, *19*(8), 3323-3333. https://doi.org/10.1091/mbc.e08-03-0328

Saxton, R. A., & Sabatini, D. M. (2017). mTOR Signaling in Growth, Metabolism, and Disease. *Cell*, *168*(6), 960-976. https://doi.org/10.1016/j.cell.2017.02.004

Schule, T., Rose, M., Entian, K. D., Thumm, M., & Wolf, D. H. (2000). Ubc8p functions in catabolite degradation of fructose-1, 6-bisphosphatase in yeast. *EMBO J*, *19*(10), 2161-2167. https://doi.org/10.1093/emboj/19.10.2161

Sherpa, D., Chrustowicz, J., Qiao, S., Langlois, C. R., Hehl, L. A., Gottemukkala, K. V., Hansen, F. M., Karayel, O., von Gronau, S., Prabu, J. R., Mann, M., Alpi, A. F., & Schulman, B. A. (2021). GID E3 ligase supramolecular chelate assembly configures multipronged ubiquitin targeting of an oligomeric metabolic enzyme. *Mol Cell*, *81*(11), 2445-2459 e2413. https://doi.org/10.1016/j.molcel.2021.03.025

Shi, D. D., Savani, M. R., Levitt, M. M., Wang, A. C., Endress, J. E., Bird, C. E., Buehler, J., Stopka, S. A., Regan, M. S., Lin, Y. F., Puliyappadamba, V. T., Gao, W., Khanal, J., Evans, L., Lee, J. H., Guo, L., Xiao, Y., Xu, M., Huang, B., . . . McBrayer, S. K. (2022). De novo pyrimidine synthesis is a targetable vulnerability in IDH mutant glioma. *Cancer Cell*, *40*(9), 939-956 e916. https://doi.org/10.1016/j.ccell.2022.07.011

Shi, Y., Lim, S. K., Liang, Q., Iyer, S. V., Wang, H. Y., Wang, Z., Xie, X., Sun, D., Chen, Y. J., Tabar, V., Gutin, P., Williams, N., De Brabander, J. K., & Parada, L. F. (2019). Gboxin is an oxidative phosphorylation inhibitor that targets glioblastoma. *Nature*, *567*(7748), 341-346. https://doi.org/10.1038/s41586-019-0993-x

Shireman, J. M., Atashi, F., Lee, G., Ali, E. S., Saathoff, M. R., Park, C. H., Savchuk, S., Baisiwala, S., Miska, J., Lesniak, M. S., James, C. D., Stupp, R., Kumthekar, P., Horbinski, C. M., Ben-Sahra, I., & Ahmed, A. U. (2021). De novo purine biosynthesis is a major driver of chemoresistance in glioblastoma. *Brain*, *144*(4), 1230-1246. https://doi.org/10.1093/brain/awab020

Singh, S. K., Clarke, I. D., Terasaki, M., Bonn, V. E., Hawkins, C., Squire, J., & Dirks, P. B. (2003). Identification of a cancer stem cell in human brain tumors. *Cancer Res*, *63*(18), 5821-5828. https://www.ncbi.nlm.nih.gov/pubmed/14522905

Song, H., Stevens, C. F., & Gage, F. H. (2002). Astroglia induce neurogenesis from adult neural stem cells. *Nature*, *417*(6884), 39-44. https://doi.org/10.1038/417039a

Stupp, R., Mason, W. P., van den Bent, M. J., Weller, M., Fisher, B., Taphoorn, M. J., Belanger, K., Brandes, A. A., Marosi, C., Bogdahn, U., Curschmann, J., Janzer, R. C., Ludwin, S. K., Gorlia, T., Allgeier, A., Lacombe, D., Cairncross, J. G., Eisenhauer, E., Mirimanoff, R. O., . . . National Cancer Institute of Canada Clinical Trials, G. (2005). Radiotherapy plus concomitant and adjuvant temozolomide for glioblastoma. *N Engl J Med*, *352*(10), 987-996. https://doi.org/10.1056/NEJMoa043330

Stupp, R., Taillibert, S., Kanner, A. A., Kesari, S., Steinberg, D. M., Toms, S. A., Taylor, L. P., Lieberman, F., Silvani, A., Fink, K. L., Barnett, G. H., Zhu, J. J., Henson, J. W., Engelhard, H. H., Chen, T. C., Tran, D. D., Sroubek, J., Tran, N. D., Hottinger, A. F., . . . Ram, Z. (2015). Maintenance Therapy With Tumor-Treating Fields Plus Temozolomide vs Temozolomide Alone for Glioblastoma: A Randomized Clinical Trial. *JAMA*, *314*(23), 2535-2543. https://doi.org/10.1001/jama.2015.16669

Terada, N., Baracskay, K., Kinter, M., Melrose, S., Brophy, P. J., Boucheix, C., Bjartmar, C., Kidd, G., & Trapp, B. D. (2002). The tetraspanin protein, CD9, is expressed by progenitor cells committed to oligodendrogenesis and is linked to beta1 integrin, CD81, and Tspan-2. *Glia*, *40*(3), 350-359. https://doi.org/10.1002/glia.10134

Touat, M., Idbaih, A., Sanson, M., & Ligon, K. L. (2017). Glioblastoma targeted therapy: updated approaches from recent biological insights. *Ann Oncol*, *28*(7), 1457-1472. https://doi.org/10.1093/annonc/mdx106

Umemura, Y., Al-Holou, W., Marini, B., Leung, D., Kim, M., Ferris, S., Junck, L., Sagher, O., Heth, J., Sun, Y., Schipper, M., Lyssiotis, C., Lawrence, T., & Wahl, D. (2022). CTNI-35. PHASE 0/1 TRIAL OF MYCOPHENOLATE MOFETIL COMBINED WITH CHEMORADIATION TO OVERCOME TREATMENT RESISTANCE IN NEWLY DIAGNOSED AND RECURRENT GLIOBLASTOMA BY TARGETING PURINE METABOLISM. *Neuro-Oncology*, *24*(Supplement_7), vii79-vii79. https://doi.org/10.1093/neuonc/noac209.300

Valvezan, A. J., McNamara, M. C., Miller, S. K., Torrence, M. E., Asara, J. M., Henske, E. P., & Manning, B. D. (2020). IMPDH inhibitors for antitumor therapy in tuberous sclerosis complex. *JCI Insight*, *5*(7). https://doi.org/10.1172/jci.insight.135071

Varn, F. S., Johnson, K. C., Martinek, J., Huse, J. T., Nasrallah, M. P., Wesseling, P., Cooper, L. A. D., Malta, T. M., Wade, T. E., Sabedot, T. S., Brat, D., Gould, P. V., Woehrer, A., Aldape, K., Ismail, A., Sivajothi, S. K., Barthel, F. P., Kim, H., Kocakavuk, E., . . . Consortium, G. (2022). Glioma progression is shaped by genetic evolution and microenvironment interactions. *Cell*, *185*(12), 2184-2199 e2116. https://doi.org/10.1016/j.cell.2022.04.038

Verhaak, R. G., Hoadley, K. A., Purdom, E., Wang, V., Qi, Y., Wilkerson, M. D., Miller, C. R., Ding, L., Golub, T., Mesirov, J. P., Alexe, G., Lawrence, M., O'Kelly, M., Tamayo, P., Weir, B. A., Gabriel, S., Winckler, W., Gupta, S., Jakkula, L., . . . Cancer Genome Atlas Research, N. (2010). Integrated genomic analysis identifies clinically relevant subtypes of glioblastoma characterized by abnormalities in PDGFRA, IDH1, EGFR, and NF1. *Cancer Cell*, *17*(1), 98-110. https://doi.org/10.1016/j.ccr.2009.12.020

Verma, R., Chen, X., Xin, D., Luo, Z., Ogurek, S., Xin, M., Rao, R., Berry, K., & Lu, Q. R. (2023). Olig1/2-Expressing Intermediate Lineage Progenitors Are Predisposed to PTEN/p53-Loss-Induced Gliomagenesis and Harbor Specific Therapeutic Vulnerabilities. *Cancer Res*, *83*(6), 890-905. https://doi.org/10.1158/0008-5472.CAN-22-1577

Wainberg, M., Kamber, R. A., Balsubramani, A., Meyers, R. M., Sinnott-Armstrong, N., Hornburg, D., Jiang, L., Chan, J., Jian, R., Gu, M., Shcherbina, A., Dubreuil, M. M., Spees, K., Meuleman, W., Snyder, M. P., Bassik, M. C., & Kundaje, A. (2021). A genome-wide atlas of co-essential modules assigns function to uncharacterized genes. *Nat Genet*, *53*(5), 638-649. https://doi.org/10.1038/s41588-021-00840-z

Wang, Q., Hu, B., Hu, X., Kim, H., Squatrito, M., Scarpace, L., deCarvalho, A. C., Lyu, S., Li, P., Li, Y., Barthel, F., Cho, H. J., Lin, Y. H., Satani, N., Martinez-Ledesma, E., Zheng, S., Chang, E., Sauve, C. G., Olar, A., . . . Verhaak, R. G. W. (2017). Tumor Evolution of Glioma-Intrinsic Gene Expression Subtypes Associates with Immunological Changes in the Microenvironment. *Cancer Cell*, *32*(1), 42-56 e46. https://doi.org/10.1016/j.ccell.2017.06.003

Wang, X., Yang, K., Wu, Q., Kim, L. J. Y., Morton, A. R., Gimple, R. C., Prager, B. C., Shi, Y., Zhou, W., Bhargava, S., Zhu, Z., Jiang, L., Tao, W., Qiu, Z., Zhao, L., Zhang, G., Li, X., Agnihotri, S., Mischel, P. S., . . . Rich, J. N. (2019). Targeting pyrimidine synthesis accentuates molecular therapy response in glioblastoma stem cells. *Sci Transl Med*, *11*(504). https://doi.org/10.1126/scitranslmed.aau4972

Wang, X., Yang, K., Xie, Q., Wu, Q., Mack, S. C., Shi, Y., Kim, L. J. Y., Prager, B. C., Flavahan, W. A., Liu, X., Singer, M., Hubert, C. G., Miller, T. E., Zhou, W., Huang, Z., Fang, X., Regev, A., Suva, M. L., Hwang, T. H., . . . Rich, J. N. (2017). Purine synthesis promotes maintenance of brain tumor initiating cells in glioma. *Nat Neurosci*, *20*(5), 661-673. https://doi.org/10.1038/nn.4537

Xie, X. P., Laks, D. R., Sun, D., Ganbold, M., Wang, Z., Pedraza, A. M., Bale, T., Tabar, V., Brennan, C., Zhou, X., & Parada, L. F. (2022). Quiescent human glioblastoma cancer stem cells drive tumor initiation, expansion, and recurrence following chemotherapy. *Dev Cell*, *57*(1), 32-46 e38. https://doi.org/10.1016/j.devcel.2021.12.007

Xie, X. P., Laks, D. R., Sun, D., Poran, A., Laughney, A. M., Wang, Z., Sam, J., Belenguer, G., Farinas, I., Elemento, O., Zhou, X., & Parada, L. F. (2020). High-resolution mouse subventricular zone stem-cell niche transcriptome reveals features of lineage, anatomy, and aging. *Proc Natl Acad Sci U S A*, *117*(49), 31448-31458. https://doi.org/10.1073/pnas.2014389117

Zeisel, A., Hochgerner, H., Lonnerberg, P., Johnsson, A., Memic, F., van der Zwan, J., Haring, M., Braun, E., Borm, L. E., La Manno, G., Codeluppi, S., Furlan, A., Lee, K., Skene, N., Harris, K. D., Hjerling-Leffler, J., Arenas, E., Ernfors, P., Marklund, U., & Linnarsson, S. (2018). Molecular Architecture of the Mouse Nervous System. *Cell*, *174*(4), 999-1014 e1022. https://doi.org/10.1016/j.cell.2018.06.021

Zhang, J., Pettersson, H. I., Huitema, C., Niu, C., Yin, J., James, M. N., Eltis, L. D., & Vederas, J. C. (2007). Design, synthesis, and evaluation of inhibitors for severe acute respiratory syndrome 3C-like protease based on phthalhydrazide ketones

or heteroaromatic esters. *J Med Chem*, *50*(8), 1850-1864. https://doi.org/10.1021/jm061425k

Zheng, H., Ying, H., Yan, H., Kimmelman, A. C., Hiller, D. J., Chen, A. J., Perry, S. R., Tonon, G., Chu, G. C., Ding, Z., Stommel, J. M., Dunn, K. L., Wiedemeyer, R., You, M. J., Brennan, C., Wang, Y. A., Ligon, K. L., Wong, W. H., Chin, L., & DePinho, R. A. (2008). p53 and Pten control neural and glioma stem/progenitor cell renewal and differentiation. *Nature*, *455*(7216), 1129-1133. https://doi.org/10.1038/nature07443

Zhou, W., Yao, Y., Scott, A. J., Wilder-Romans, K., Dresser, J. J., Werner, C. K., Sun, H., Pratt, D., Sajjakulnukit, P., Zhao, S. G., Davis, M., Nelson, B. S., Halbrook, C. J., Zhang, L., Gatto, F., Umemura, Y., Walker, A. K., Kachman, M., Sarkaria, J. N., . . . Wahl, D. R. (2020). Purine metabolism regulates DNA repair and therapy resistance in glioblastoma. *Nat Commun*, *11*(1), 3811. https://doi.org/10.1038/s41467-020-17512-x

Zhu, Y., Guignard, F., Zhao, D., Liu, L., Burns, D. K., Mason, R. P., Messing, A., & Parada, L. F. (2005). Early inactivation of p53 tumor suppressor gene cooperating with NF1 loss induces malignant astrocytoma. *Cancer Cell*, *8*(2), 119-130. https://doi.org/10.1016/j.ccr.2005.07.004

Zhu, Y., Romero, M. I., Ghosh, P., Ye, Z., Charnay, P., Rushing, E. J., Marth, J. D., & Parada, L. F. (2001). Ablation of NF1 function in neurons induces abnormal development of cerebral cortex and reactive gliosis in the brain. *Genes Dev*, *15*(7), 859-876. https://doi.org/10.1101/gad.862101

Zimmerman, L., Parr, B., Lendahl, U., Cunningham, M., McKay, R., Gavin, B., Mann, J., Vassileva, G., & McMahon, A. (1994). Independent regulatory elements in the nestin gene direct transgene expression to neural stem cells or muscle precursors. *Neuron*, *12*(1), 11-24. https://doi.org/10.1016/0896-6273(94)90148-1